2011

An evaluation of fall speed characteristics in bin and bulk microphysical schemes and use of bin fall speeds to improve forecasts of warm-season rainfall

Eric Anthony Aligo
Iowa State University

An evaluation of fall speed characteristics in bin and bulk microphysical schemes and use of bin fall speeds to improve forecasts of warm-season rainfall

by

Eric A. Aligo

A dissertation submitted to the graduate faculty

in partial fulfillment of the requirements for the degree of

DOCTOR OF PHILOSPHY

Major: Meteorology

Program of Study Committee:
William A. Gallus, Jr., Major Professor
Raymond W. Arritt
William J. Gutowski
Gene S. Takle
Xiaoqing Wu
Brad S. Ferrier
Gregory Thompson

Iowa State University

Ames, Iowa

2011

TABLE OF CONTENTS

ABSTRACT

As computer power increases and model grid spacing decreases, more emphasis will be put on model microphysics to produce accurate forecasts of rainfall including that from warm-season mesoscale convective systems (MCSs). Some believe bin microphysical schemes are far superior to the commonly used bulk microphysical schemes because of their ability to more accurately depict certain processes like sedimentation. However, bin schemes are computationally inefficient and there are no plans in the near future to implement such schemes operationally. Instead, this study proposes to use a technique in Weather Research and Forecast (WRF) Advanced Research WRF (ARW) simulations that attempts to improve bulk microphysical forecasts of warm-season MCSs by harnessing the intrinsic characteristics of bin fall speed distributions that are important for the sedimentation process provided the fall speed characteristics in bin schemes differ from those in commonly used bulk schemes.

Fall speed distributions of rain, snow, graupel and cloud ice were compared between a bin scheme and three bulk schemes, and were found to be different between the different schemes. The microphysical processes that contributed the largest to the microphysical budget in the bin scheme often occurred with the slower fall speeds, but the opposite was true for the bulk schemes. There was evidence of size-sorting in the bin and Thompson bulk schemes, a naturally occurring phenomenon. This feature was not simulated in the WSM6 and Lin schemes and can be attributed to those schemes being single moment and the Thompson scheme being double moment in ice and rain.

Since the characteristics of the bin fall speeds were different from those in the bulk schemes, bin fall speeds were used to modify bulk scheme fall speeds using a probability

matching technique that was developed to improve the prediction of warm-season MCSs. The sensitivity of different convective morphologies to the fall speed modifications was also evaluated. First, various tests were performed with various microphysical schemes and cases in order to find the vertical grid configuration that provides the best rainfall forecast. Rainfall forecasts worsened when the number of vertical levels was doubled from a control configuration of 31 levels and an over prediction of rainfall occurred. The largest improvement in skill occurred when the levels above the melting level were doubled and this was attributed to better resolved cold-cloud microphysical processes. As such, simulations using the probability matching technique employed the vertical configuration with refined vertical grid resolution above the melting layer.

The different convective morphologies responded similarly when the fall speed modifications were made with all systems simulating a narrower stratiform region, less stratiform rainfall and a larger anvil. Rainfall forecasts generally improved with the use of the probability matching technique with improvements in the lightest and heaviest rainfall. The reduced stratiform rainfall occurred as a result of slower falling snow and a reduction in downward fluxes of snow, while forecasts of convective rainfall intensity improved as a result of faster falling graupel. Sensitivity tests were performed by computing bulk-like fall speeds in the bin scheme, which resulted in a modification of the particle size distribution of snow, which led to faster falling snow, larger downward fluxes of snow and a larger stratiform rain region.

CHAPTER 1. GENERAL INTRODUCTION

Introduction

Some ten to twenty years ago, NWP models typically used a horizontal grid spacing of ten to twenty kilometers, which required the use of cumulus parameterizations in order to resolve the effects of sub-grid scale cumulus convection (Kain and Fritsch 1993; Betts 1986; Betts and Miller 1986; Janjic 1994). Today, grid spacing in some high-resolution NWP runs is approaching that of the convective-scale and as such microphysical schemes are becoming even more important (Milbrandt 2005a) as cumulus parameterizations are no longer used.

To save on computational costs, research and operational centers have relied heavily on bulk microphysical schemes rather than bin schemes. Bulk microphysical schemes assume a size distribution function for each hydrometeor type, and predict one or more moments of that distribution. Schemes that predict one moment of the size distribution often predict the mass content and are referred to as single moment schemes (Rutledge and Hobbs, 1983; Lin et al., 1983). Microphysical schemes that predict two moments of the size distribution often predict the number concentration in addition to the mass content (Thompson et al. 2008b; Ferrier, 1994; Morrison et al., 2005). Some microphysical schemes are triple moment and predict radar reflectivity in addition to number concentration and mass content (Milbrandt and Yau 2005a). Although higher moment schemes have been shown to better represent the sedimentation process, errors in sedimentation still exist (Milbrandt and McTaggart-Cowan 2010).

Bin microphysical schemes, on the other hand, predict the mass content and number concentration for an entire spectrum of sizes for different hydrometeor categories and are believed to best represent the evolution of the rain drop size distribution (Straka 2009) as well as the sedimentation process. Bin schemes, unlike bulk schemes, also have the advantage of allowing different-sized hydrometeors to exist per model grid point.

Operational centers have no intentions of implementing bin microphysical schemes because of computational costs, and that is why so much work has been done with bulk microphysical schemes in order to improve rainfall forecasts of all types of systems including warm-season mesoscale convective systems (MCSs). It is well known that warm-season rainfall is one of the most poorly forecasted meteorological parameters (Carbone 2004). Jankov et al. (2005) showed that rainfall forecasts are sensitive not only to the choice of convective parameterization but also to the microphysical scheme used. Studies have the shown the importance of the ice phase in creating the stratiform region associated with warm-season MCSs (McCumber et al (1991), while another study noted that parameterizations in microphysical schemes can produce errors in the structure of systems (Gallus and Pfeifer 2008). Various sensitivity tests have been performed including changing the particle densities, particle size definition and fall speeds, all of which affected the spatial patterns of rainfall. Even different convective morphologies have been shown to have different sensitivies to microphysics with the stratiform region of trailing stratiform (TS) systems, whose stratiform region occurs to the rear of the convective line, sustained by mesoscale updrafts induced by condensation and deposition (Gallus and Johnson 1995). On the other hand, leading stratiform (LS) systems have the stratiform region out ahead of the convective line and are believed to be sustained by evaporation and sublimation of the particles in the stratiform region (Storm et al. 2007).

In this study, we compare fall speed distributions of rain, snow, graupel and cloud ice between a bin scheme and some popular bulk microphysical schemes and evaluate the importance of fall speed distribution characteristics to microphysical processes using the Weather Research and Forecasting (WRF) Advanced Research WRF (ARW) model. The goal is to determine if bin fall speed characteristics differ from those in bulk schemes and if they do to use that information in a bulk scheme in an attempt to improve forecasts of warm-season TS and LS systems. A probability matching technique would then be implemented in a bulk scheme essentially using the bin scheme fall speed information to drive a bulk scheme simulation. The best model vertical grid configuration to use for the experiment was determined after extensive testing with different vertical grid resolutions (VGRs). An increased VGR in hurricane simulations in a recent study yielded an improvement in hurricane intensity and structure. It is expected that with a higher VGR, cloud microphysical processes will be better resolved and will improve rainfall forecasts.

Thesis Organization

This thesis follows the journal paper format. Chapter 1 contains the general introduction to the thesis, Chapter 2 is a paper which will be submitted to the *Journal of Atmospheric Sciences*, and compares bin and bulk microphysical fall speeds and associated microphysical processes. Chapter 3 is an exploratory study that evaluates the impact of using different vertical grid resolutions and has been published in *Weather and Forecasting*. Chapter 4 discusses the results of simulations using the probability matching technique in 2D and 3D simulations, and is a paper that will be submitted to *Monthly Weather Review*. Chapter 5 is the general conclusions

which review the major findings of the three papers. The final part of the thesis is the reference section.

CHAPTER 2: COMPARISON OF HYDROMETEOR FALL SPEED DISTRIBUTIONS IN BIN AND BULK MICROPHYSICAL SCHEMES

Eric A. Aligo and William A. Gallus, Jr.

Dept. of Geological and Atmospheric Sciences, Iowa State University, Ames, IA

Gregory Thompson

Research Applications Program, National Center for Atmospheric Research, Boulder, CO

Brad S. Ferrier

Mesoscale Support Task, IMSG, NOAA/NWS/NED/EMC W/NP2, Camp Springs, MD

(A paper to be submitted to the Journal of Atmospheric Sciences)

Corresponding author address: Eric A. Aligo, Iowa State University, 3010 Agronomy Hall, Ames, IA , 50011 email: eric.aligo@noaa.gov.

Abstract

Using the Weather Research and Forecast (WRF) model, idealized two dimensional simulations of squall lines were performed to compare fall speed distributions from a spectral (bin) microphysical scheme to three widely-used bulk schemes. The bin model exhibited wider spectra of fall speed distributions compared to any of the bulk schemes. More specifically, the bin model had more frequent low fall speeds for all hydrometeors. The bin model also exhibited the slowest falling rain due to a relatively crude method for treating the melting of ice. A microphysical budget analysis indicated that the melting of graupel contributed to the smaller fall speeds in the bin model, whereas both snow melting and graupel melting was mostly responsible for the larger fall speeds in the bulk schemes. Despite having slower fall speeds, the Geresdi bin scheme had a narrower stratiform region compared to the bulk schemes, contrary to expectations, possibly because the system in the bin scheme was weaker. The method for dealing with the melting of ice as well as a different solution for condensation in the bin scheme might have contributed to a weaker system in the bin scheme compared to the bulk schemes. The weaker flow in the bin scheme might have acted to limit the amount of advection experienced by the hydrometeors resulting in the narrower stratiform region. Comparison of hydrometeor fall speeds also reveals potential flaws in specific physical aspects found in one or more of the bulk schemes.

1. **Introduction**

Since mesoscale convective systems (MCSs) represent the major source of warm-season rainfall for the central and northern Plains (Fritsch et al. 1986), it is important to have high quality rainfall forecasts of such systems. Numerical model rainfall forecasts have been shown to be most sensitive to the choice of convective parameterization, but also sensitive to the choice of microphysical scheme (Jankov et al. 2005) used. McCumber et al (1991), among others, have shown that the ice phase is needed to give realistic simulations of convective systems that may develop stratiform regions, a common occurrence in the systems affecting the Midwest in summer. Gallus and Pfeifer (2008) compared synthesized polarimetric radar scans from runs using five microphysical schemes to observed polarimetric data and found spatial errors in reflectivity throughout their trailing stratiform system. The errors were thought to be related to the microphysical parameterizations as well as errors in dynamics, vertical motions and lateral boundary effects. Gallus and Johnson (1995), while noting that stratiform precipitation associated with trailing stratiform (TS) systems can be due to the rearward transport of slightly positively buoyant high θ_e air detrained from active and dissipating convective towers, also pointed out that increases in effective buoyancy can be due to the fallout of precipitation. Condensation, freezing and deposition are processes that contribute to latent heating and an increase in buoyancy in the stratiform region.

Modifications to microphysical parameters have been shown to substantially impact cloud processes and resultant rainfall. Gilmore et al. (2004b) illustrated the importance of modifications to hydrometeor densities and slope intercepts on the areal coverage of rainfall in their idealized simulations of supercells. They found that slower falling graupel particles,

compared to faster falling hail particles, remained suspended in the cloud for a longer period of time allowing them to be advected outside of the updraft region, resulting in less total ground-accumulated rainfall. Initial near-surface downdrafts for the simulation with graupel particles were weaker and outflow was warmer (compared to simulations using hail) as the slower falling graupel particles took longer to reach the melting level and turn to rain thus delaying the evaporation.

Potter (1991) noted a sensitivity of the fall speeds of snow and graupel/hail to the definition of particle size. Particle size was defined to be the diameter of the melted particle, as well as the maximum ice-particle dimension. The difference in the fall speed values of snow between the two different fall speed definitions was ~ 0.25 m s^{-1} for a range of mixing ratio values. They noted that differences in the fall speeds can affect accretion rates. The smaller the fall speed, the less the accretion and hence snow and graupel mixing ratios, which leads to less evaporative cooling at low-levels, a weaker cold pool and fewer vigorous storms.

Colle and Mass (2000) showed how changes in the fall speed of snow can affect the distance over which the snow is advected and hence the location of the surface precipitation. They compared two snow fall speed relations, with one providing fall speeds lower by 20% for different particle sizes. Minor improvements in bias and root mean square scores (rms) were noted while using the slower fall speeds in their simple ice schemes (only snow and ice below 0C) due to the slower falling snow particles being advected farther away from the main updraft region.

Lynn and Khain (2007) performed 3D runs of a squall line associated with a sea-breeze event and showed a reduction in surface convective rain rates and a better defined stratiform

cloud structure that were both closer to observations in their runs using a spectral (bin) microphysical scheme as compared to runs using several bulk microphysical schemes. Bin schemes, unlike bulk schemes, allow different-sized hydrometeors to exist per model grid point, thus allowing the smaller, slower falling particles to advect away from the updraft region resulting in a reduction in rain rate in the convective region and a better defined stratiform region. Lynn et al. (2005) note that mean fall speeds in bulk schemes can lead to both unrealistic vertical and horizontal distributions of hydrometeors and errors in the simulation of convection.

An objective of this paper is to extend the work of Lynn and Khain (2007) by determining if the shapes of hydrometeor fall speed distributions differ between bulk and bin schemes, and more specifically, determine if the bin scheme has slower falling hydrometeors, and if this results in a system that differs for bulk schemes as described in their work. This paper will also provide initial insight into the relationship between fall speeds and microphysical processes. The model and experimental design are described in section 2, followed by the results in section 3 and conclusions in section 4.

2. Data and Methodology

a) Model setup and data

Two dimensional (2D) idealized Weather Research and Forecast (WRF) Advanced Research WRF (ARW) model (Skamarock et al. 2005) simulations were performed using a bin microphysical scheme (Geresdi 1998; Rasmussen et al. 2002; hereafter denoted as Geresdi) in addition to the Lin (Lin et al. 1983), WSM-6 class (Hong and Lim 2006; WSM6) and Thompson

(Thompson et al. 2008) bulk microphysical schemes. The Geresdi scheme is double moment in liquid, pristince ice, rimed ice (snow) and graupel meaning it predicts both the mass mixing ratios and number concentrations of these species of water. The Thompson scheme is double moment in rain and ice, but it is single moment in snow, graupel and cloud water, meaning it predicts only the mass mixing ratios of those last three species of water. The WSM6 and Lin schemes are single moment schemes and predict the mass mixing ratios of cloud water, cloud ice, snow, graupel and rain.

The three idealized runs in this study simulate a squall line in the x direction (east-west) and were initialized each with a sounding from Weisman et al. (1988; default sounding provided with the WRF package), a modified sounding from 12 June 2002 from the International H_2O Project (IHOP; Parsons 2002), and a sounding representative of a leading stratiform (LS) system (Parker and Johnson 2004). Convection is initiated in the center of the domain by a 4-km radius and 3 K warm thermal perturbation except for a 1.5 K perturbation in the 12 June 2002 case. A perturbation of 3 K was not used in the 12 June 2002 case because it resulted in gravity-wave generated convection, which led to additional updrafts that interfered with main system. The simulations were run for six hours using a horizontal grid spacing of 1 km with 80 vertical levels and 600 horizontal grid points yielding a horizontal domain size of 600 km. The idealized runs use a flat terrain, do not consider radiation, surface fluxes or frictional effects. The boundary conditions are open in the x-direction and periodic in the y-direction.

b) Experimental design

One of the important differences between bin and bulk schemes is in the prescription of fall speeds. In the Geresdi bin scheme, there are 36 mass doubling bins of liquid, pristine ice, rimed ice (snow) and graupel. A unique fall speed relation is used for each hydrometeor and is used to determine the fall speeds for each of the 36 bins. All falling particles follow the power law relation from Ferrier (1994):

$$V(D) = \left(\frac{\rho_0}{\rho}\right)^{1/2} \alpha D^{\beta} e^{-fD}, \qquad (1)$$

where ρ_0 is a reference air density usually chosen to be close to the surface, ρ is the air density at a particular altitude, D is the diameter of the particle and α, β and f are constants that are defined in Table 2. The hydrometeor fall speed formulation deviates from (1) for liquid and graupel in Geresdi with fall speeds for these species of water based on the Best and Bon number approach as described in Pruppacher and Klett (1997), and Rasmussen and Heymsfield (1987), respectively.

For the bulk schemes used in this paper, mean mass-weighted fall speeds are determined for cloud ice, rain, snow and graupel using the relation:

$$\hat{V} \equiv \frac{\int_0^{\infty} V(D) m(D) N(D) dD}{\int_0^{\infty} m(D) N(D) dD}, \qquad (2)$$

where $V(D)$ also follows (1), except in Lin for graupel and cloud ice (Lin et al. 1983), $m(D)$ is described using the following power law relation:

$$m(D) = aD^{b}, \qquad (3)$$

and *N(D)* is the particle number concentration, which is diagnosed often assuming the exponential or Marshall-Palmer size distribution (Marshall and Palmer 1948). Thompson et al. (2008) and others (Walko et al. 1995; Verlinde et al. 1990) have used the gamma distribution to diagnose *N*(D), finding it to be a better fit for certain hydrometeors. The coefficients, *a* , and, *b* , in (3) are microphysical-scheme dependent, and will not be shown here for the sake of brevity.

The addition of 288 new prognostic variables in the bin scheme increases computational costs by a factor of 40, restricting the simulations presented in this paper to 2D.

1) MICROPHYSICAL BUDGET

A microphysical budget was computed using the following from Colle et al. (2005):

$$\overline{Pqqqq} = \frac{\sum_{i,k} p^*(i) \times Pqqqq(i,k) \times \Delta\sigma(k)}{\sum_{i,k} p^*(i) \times WVL(i,k) \times \Delta\sigma(k)}, \qquad (4)$$

where $Pqqqq(i,k)$ is a source/sink term from any of the microphysical schemes averaged for the layer between two sigma levels. Source/sink terms in the tendency equations of Thompson are provided in the appendix with the definitions of each term in Table 1. Tendency equations similar to those in Thompson exist for the other schemes, but will not be shown here. Also in (4), $WVL(i,k)$ is the water vapor loss rate (*pri_inu*+ *pri_ide*+ *prs_ide*+*prs_sde*+ *prg_gde*+ *prw_vcd* in the Thompson scheme), Δσ is the distance between any two sigma levels, and *p**(i) is the pressure difference between the top of the model and the surface. The budget can be used to identify the most important microphysical processes contributing to the creation of hydrometeors

and their associated fall speeds. Colle et al. (2005) performed their budget over a volume fixed in space and time. In this study, however, the budget was evaluated for all times beginning one hour into the simulation and for portions of the system over predetermined fall speed ranges. Note that while all of the source/sink terms were accumulated over every model time step (2 seconds), only ten minute accumulations were used for the budget computations with 31 ten minute intervals used in the construction of the microphysical budet. For a grid point to be considered in the budget analysis, it had to have a fall speed value within a pre-determined range for the time being evaluated and the previous time (ten minutes earlier). This condition limits the particles being evaluated to those that likely had values within the pre-determined range throughout the ten minute time interval over which the microphysical processes were accumulated. It is important to note that $WVL(i,k)$ will be different for each scheme, and it represents the total water vapor loss over the entire spectrum of fall speeds for a given species of water, thus making comparisons of different portions of the spectrum possible and isolating the fall speeds most important to the budget.

3. Results

a) Weisman case

1) RAIN WATER

Graupel melting was responsible for the entire spectrum of rain fall speeds in Geresdi (Fig. 1a) with the more moderately falling rain contributing most to graupel (only 3% of graupel melting produced the slowest and fastest falling rain). In Thompson, rain collecting cloud water

(RCW) became less important (Fig. 1b) as rain fall speeds increased, but the reverse was the situation in WSM6 (Fig. 1c). This was likely due to larger cloud water mixing ratios simulated in Thompson (WSM6) in the vicinity of the slower (fastest) falling rain. In WSM6 and Lin, graupel melting was the dominant microphysical process (Fig. 1d), similar to what was found in Geresdi. Snow melting played almost no role in Lin in the production of rain in contrast to what was seen in Thomspon. Thompson and Lin have been known to produce too much snow and graupel, respectively (Lin et al. 2006); therefore, it is not surprising that melting snow and melting graupel are the largest contributors to rain in the respective schemes.

Although the relative importance of each microphysical process can be evaluated from the budget plots in Fig. 1, it is difficult to compare processes across schemes because each scheme has a different WVL rate, a key component in the construction of the budget. Since processes below the melting level ($\geq$ 0°C) are primarily responsible for creating a healthy stratiform and convective rain region, the relative contribution of each scheme to rain water mixing ratios was evaluated. This was achieved by recomputing (4) using the scheme-averaged WVL, and the results are shown in Fig. 2. In Lin, 114% of the WVL went toward the production of rain, more than any other scheme with WSM6 following closely behind (108%). The percentage of rain production in Thompson and Geresdi was about half the Lin amounts with contributions of 69% and 50%, respectively. Mostly consistent with the trends in the budget plots, the domain-integrated six- hour accumulated surface rainfall was highest for Lin and WSM6 (5428 and 5012 mm, respectively) and lowest for Geresdi and Thompson (4455 and 4170 mm, respectively). With more mass moving into the rain category in Lin and WSM6 compared to the other two schemes, less mass was available to produce a large anvil as was the case in

Geresdi and Thompson (see vertical cross sections of total condensate valid 4 hours into the simulation with the 0.1 g kg^{-1} value contoured).

Fig. 3 illustrates fall speed distributions of rain for the bulk schemes and liquid (cloud water and rain water) for Geresdi. In Geresdi, fall speeds above 0.0933 m s^{-1} represent rain water, while those below that value represent cloud water with the dividing point representing a drop diameter of 50 μm. For the same drop size, the rain in Lin and WSM6 will have fall speeds of 0.3 m s^{-1}, but they will have fall speeds of 0.24 m s^{-1} in Thompson. It is of interest to know if differences in the simulated fall speed distributions between Geresdi and any bulk scheme are due simply to different fall speed relations or other physical processes. To test this, a theoretical mass-weighted fall speed was computed using both the Geresdi and Thompson fall speed relations for a range of mass mixing ratios. Since only the velocity-diameter relationship was allowed to vary, any differences in the computed mass-weighted fall speeds would be directly related to fall speed relations. For rain and snow, mass-weighted fall speed differences between Geresdi and Thompson were less than 1% and 10%, respectively. Thus, the presence of slower falling rain and snow in the bin scheme likely was the result of physical processes and not because of its fall speed relation. For graupel and cloud ice, however, differences in mass-weighted fall speeds were substantial and were as high as 55% and 80%, respectively. The slower falling cloud ice in the bin scheme could be a byproduct of its fall speed relation. Interestingly, Thompson had slower falling graupel in this theoretical experiment, but had narrower fall speed distribution (fewer slower and faster falling graupel particles) in all three model simulations suggesting that physical processes in the bin scheme made its fall speed distributions wider.

A substantial amount of the slowest falling rain in Geresdi, associated with graupel melting, was simulated at 700 hPa (shown as blue in Fig. 4a), and could be the result of a very crude method for treating melting ice in Geresdi. In Geresdi, when the air temperature is slightly above freezing and the ice particle begins to melt, tiny drops are shed from the particle instead of remaining with the particle and becoming a larger drop. The impact this approach might have on the system is evaluated in more detail in a later section. In Fig. 4, the total condensate (indicated by the 0.1 g kg^{-1} mixing ratio contour) is shown 4 hours into the simulation along with the spatial distribution of the fall speeds, separated into three categories: blue for the slowest falling rain, red for more moderately falling rain and green for the fastest falling rain. This time was chosen as it depicted the mature stage of the system in each scheme. It should also be pointed out that the white spaces between colors in Fig. 4 indicate the points that experienced fall speeds of two different colors during the ten minute time period over which the processes were accumulated. The largest fall speeds in WSM6 near the convective region (Fig. 4c) were also more spatially extensive and had lower values than those in Thompson (Fig. 4b) possibly due to the use of different fall speed relations and smaller particle sizes in WSM6.

There is some indication of size sorting in Thompson and Geresdi, but not in WSM6 or Lin. Milbrandt and Yau (2005a) note that gravitation alone results in the larger, faster falling particles being distributed near the ground, and the smaller, slower falling particles being distributed aloft. Single-moment schemes cannot replicate this pattern because they use one mean mass-weighted fall speed for an entire spectrum of particle sizes for each hydrometeor type and they predict only the mass mixing ratios. Double moment schemes predict both the mass mixing ratios and number concentrations requiring a mass-weighted fall speed and an additional number-weighted fall speed. The differential sedimentation that results from the two different

fall speeds allows size-sorting patterns to emerge. The WSM6 and Lin schemes are single moment, while the Thompson scheme is single moment only in snow and graupel. The Thompson scheme is double moment in rain and cloud ice, while the Geresdi is double moment in each hydrometeor category.

2) SNOW

It is clear that a large portion of the snow field in Geresdi is of the slower falling kind, while in the bulk schemes it is of the faster falling kind (Fig. 5). All schemes, except for Thompson, share snow collecting cloud ice (SCI) as either the most important or the second most important microphysical process in producing snow particles. SCI is almost non-existent in Thompson as cloud ice mixing ratios are very small (at least one order in magnitude smaller than those in the other schemes) because this scheme is very efficient in converting cloud ice to snow.

Snow fall speeds in Geresdi, Thompson and WSM6 peaked at around 0.5 m s^{-1} (Fig. 6), while a second, smaller, peak in WSM6 occurred around fall speeds of 1.3 m s^{-1}. Fall speeds in Lin were much larger with peak values nearing 2.0 m s^{-1}, because this scheme uses graupel-like snow from Locatelli and Hobbs (1974).

The slowest falling snow extended through a deep layer between 150 hPa and 700 hPa in Geresdi and WSM6 (Fig. 7a,c), although it occupied many fewer grid points in WSM6. In Thompson, the slowest falling snow was restricted to a 100 hPa depth above 300 hPa (Fig. 7b). An interesting feature in Fig. 7 is the increase in snow fall speeds with increasing height in Lin, a feature not at all seen in the other schemes. Observational studies using vertically pointing radar data have shown that snow fall speeds decrease with increasing height (Orr and Kropfli, 1998**;**

Lin and Colle, 2008) making the Lin an outlier in this regard. The exponent in the fall speed relation for snow in Lin is set to 0.25, while larger exponents are used in the other schemes (1 in Thompson, 0.41 in WSM6 and 0.55 in Geresdi for approximately the first 15 bins and then 0.25 for the remaining bins). It is believed the smaller exponent in Lin makes the fall speeds relatively insensitive to the diameter of the particle and more sensitive to the air resistance factor. The air resistance factor allows for the fall speeds to increase with increasing height (Lin et al. 1983). There is strong evidence of size-sorting in Geresdi and Thompson (Fig. 7a,b), but little evidence of this in WSM6 and Lin (Fig. 7c,d).

Fig. 7 illustrates nicely how the bin scheme has the potential to produce a wider anvil and stratifrom region than its bulk counterparts as a large portion of the TS system has fall speeds much lower, and in some areas half as large as those in the bulk schemes. However, in this study, the extent of the anvil and stratiform region in Geresdi is similar to or smaller than that simulated in the bulk schemes. This feature is further illustrated in hovmöller diagrams of surface rain rate (in. h^{-1} ; 1 in. = 25.4 mm) from all four schemes (Fig. 8) with the stratiform rain rates depicted by cool colors (those with rain rates less than 0.40 in. h^{-1}) and convective rain rates depicted by warm colors (those with rain rates exceeding 0.39 in. h^{-1}). All three bulk schemes (Fig. 8b,c,d) have a wider stratiform rain region than what was simulated in the bin scheme. A time series of domain-averaged upward vertical velocities shows the bulk schemes have a stronger system for the first three hours of the simulation with the Lin scheme upward motions double those of the bin scheme on two separate occasions (Fig. 9). The system matures sooner in the bulk schemes compared to the bin scheme as upward motions in the bulk schemes begin to weaken after 3 hours at which time the bin scheme upward motion begins to strengthen. The only exception was with WSM6 as isolated convection developed ahead of the main system complicating the

results during the last hour. The weaker system in Geresdi in the first half of the simulation might explain the comparable anvil and stratifrom region to that of the bulk schemes, as hydrometeors were not ejected as high into the atmosphere and were subjected to a weaker circulation. The weaker upward motions in the bin scheme can be explained by less latent heat of condensation produced (not shown) due to the condensation formulation in the Geresdi bin scheme.

An additional factor that might explain the meager stratiform region in the bin scheme is the crude method used for melting ice. As mentioned earlier, a large number of very small drops are created as ice begins to melt. This can be seen also through an analysis of number concentration (not shown) as a large number of small drops were clustered around the melting level. Time-averaged cross-sections of liquid evaporation (cloud water and rain water) show ten minute evaporation rates three times larger (up to 3.5 g kg^{-1}) in the bin scheme compared to the bulk schemes (Fig. 10). The peak evaporation rate in Geresdi is centered at and just below the melting level, while in the bulk schemes, the peak evaporation rate extended closer to the surface indicating that in the bin scheme, tiny rain particles evaporate very quickly near the melting level leaving the remainder of the boundary layer with low rain water mixing ratios.

3) GRAUPEL

Rain collecting graupel was very important in Geresdi (Fig. 11a) and WSM6 (Fig. 11c). In Geresdi, this could be a reflection of the ice melting issue with an abundance of tiny drops being collected by graupel, which might not necessarily be physically correct. Rain collecting

graupel was not at all important in Thompson (Fig. 11b) and Lin (Fig. 11d), and in Thompson, this could be because both rain and graupel have nearly the same fall speeds limiting the interactions between the two species. Rain collecting snow (RCS) was important in Thompson, and not at all in Lin, a result not surprising due to the aforementioned biases in snow and graupel in Thompson and Lin. Additionally, graupel deposition was relatively important in Lin, but miniscule in Geresdi and WSM6. Graupel deposition is formulated in such a way that it rarely occurs in Thompson.

As with the fall speed distributions for snow and rain, the graupel fall speeds in Geresdi were distributed over a wider range of values mostly for the smaller fall speeds (Fig.12). The Thompson and the Geresdi schemes had similar frequency distributions, while the Lin scheme had all fast falling graupel. A peak occurred near 0.5 m s^{-1} in Geresdi as well as in WSM6 and Thompson; however, these slow falling graupel particles were important only in WSM6. Most of the graupel obtained fall speeds greater than 1.5 m s^{-1} in Lin and had peak values near 5 m s^{-1}

The spatial pattern of the fall speeds in Geresdi and Thompson was very similar with most of the graupel located behind the convective line (Fig. 13a,b). The slowest falling graupel, however, was more abundant in Geresdi and the faster falling graupel extended all the way to the surface in Geresdi. For the most part, the fastest falling graupel (fall speeds larger than 3.5 m s^{-1}) contributed most to the microphysical budget except in WSM6, for which the more moderate fall speeds were important, and the fall speeds encompassed a large area from 700 hPa to 300 hPa.

There is again some indication of fall speeds increasing with increasing height in Lin, although this is not as noticeable for graupel. Lin does have the smallest exponent in the fall speed relation for graupel compared with other schemes, thus possibly explaining the spatial

distributions seen in Fig. 13. A total lack of size-sorting is evident in the Lin and WSM6 schemes, whereas the Geresdi and Thompson schemes clearly show this very physical behavior.

3) ICE

For the fastest falling ice (fall speeds exceeding 0.1 m s^{-1}), the freezing of cloud water into cloud ice (CWF) was the dominant microphysical process for Thompson and Lin (Fig. 14b,d) with ice deposition (IDEP) most important in Geresdi and WSM6 (Fig. 14a,c). Ice fall speeds slower than 0.1 m s^{-1} were simulated (Fig. 15), but these ice particles did not contribute much to the microphysical budget. The slowest falling ice (speeds less than 0.1 m s^{-1}) most frequently occurred in Geresdi and WSM6 with a more substantial proportion of slow falling ice occurring in Geresdi. Thompson and Geresdi ice fall speeds peaked around 0.2 m s^{-1}, with WSM6 and Lin peaking around 0.5 m s^{-1}. Similar to what was seen in Fig. 15, Fig. 16 also shows that Geresdi had the widest spectrum of cloud ice fall speeds. Common among all schemes, and most notably in Geresdi, the slowest falling ice was simulated close to cloud top and cloud bottom, a feature that is realistic based on vertically pointing radar data (Matrosov et al. 2002).

b) IHOP (June 12 2002) and LS case

Fall speed distributions were constructed from the 2D idealized simulations that used the IHOP 12 June 2002 sounding and the LS sounding, and were found to be very similar to those described throughout this paper for the simulations using the Weisman sounding. Figure 17

illustrates the fall speed distributions for all species and schemes for the LS case, and shows how the shape of the distributions are almost unchanged compared to those shown for Weisman. Since the distributions were similar among all three cases, detailed results from the 12 June 2002 and LS cases will not be discussed here.

4. Conclusions

Exploratory two dimensional WRF ARW idealized simulations of warm season MCSs were performed to compare fall speed distributions between the Geresdi bin scheme and the Thompson, WSM6 and Lin bulk schemes. Results were shown from the simulations using a sounding from Weisman et al. (1988), and revealed that Geresdi had a wider spectra of fall speed distributions for all hydrometeors, and more notably, more slower falling hydrometeors compared to the bulk schemes. Although the largest peaks in the snow and graupel distributions occurred with the smallest fall speeds, the microphysical processes associated with these particles did not contribute much to the total microphysical budget in the bulk schemes, but they played a more substantial role in the Geresdi bin scheme. While this study showed that there is the potential for a larger anvil and stratiform region in the Geresdi bin scheme compared with the bulk schemes due to the advection of slower falling particles farther away from the main updraft region, this might have been limited by a weaker system caused by a crude method for dealing with melting ice and a better solution for condensation, which results in less latent heating in the bin scheme.

Increasing snow and graupel fall speeds with increasing height simulated only in the Lin scheme might have been due to the use of a smaller exponent in the fall speed relation, making

the fall speeds relatively insensitive to the diameter and more sensitive to the air resistance factor. The air resitance factor allows the fall speeds to increase with height. Size sorting was well simulated in the Geresdi bin scheme and the Thompson bulk scheme, but not simulated well or at all in the WSM6 and Lin schemes likely due to the WSM6 and Lin schemes being single moment in each hydrometeor.

Bin schemes are often thought to better represent fall speed distributions due to their more appropriate use of fall speeds (Lynn et al. 2007). Additionally, since all three cases yielded similar fall speed distributions with the bin scheme simulating slower falling hydrometeors compared to the bulk schemes, future work will involve using the fall speed distributions from the bin model to drive bulk scheme simulations in 2D as well as in 3D. The impacts of the fall speed modifications on the convective and stratiform rainfall of different types of convective systems (trailing stratiform and leading stratiform) could then be evaluated and compared against observations. Additional work could try to improve the melting ice formulation in the bin scheme in order to make it more realistic, and to evaluate the sensitivity of the system's cold pool, circulations and stratiform/anvil regions to such modifications.

Acknowledgements

The authors would like to thank Lulin Xue, Kyoko Ideka, Moti Segal and Chris Karstens for their input. This research was funded by NSF Grants ATM-0848200 and ATM-0537043.

Appendix

Thompson Microphysical Tendency Equations

Note that q_v,q_c,q_r,q_s and q_g below are the mixing ratios of water vapor, cloud water, rain water, snow and graupel, respectively. See Table 1 for a definition of all of the source/sink terms indicated below.

$$dq_v/dt = (-pri\_inu - pri\_ide - prs\_ide - prs\_sde - prg\_gde - prw\_vcd + prv\_rev),$$

$$dq_c/dt = (-prr\_wau - pri\_wfz - prr\_rcw - prs\_scw - prg\_scw - prg\_gcw + prw\_vcd),$$

$$dq_i/dt = (+pri\_inu + pri\_ihm + pri\_wfz + pri\_rfz + pri\_ide - prs\_iau - prs\_sci - pri\_rci + sed\_i),$$

$$dq_r/dt = (+prr\_wau + prr\_rcw + prr\_sml + prr\_gml + prr\_rcs + prr\_rcg - prg\_rfz - pri\_rfz - prr\_rci - prv\_rev + sed\_r),$$

$$dq_s/dt = (+prs\_iau + prs\_sde + prs\_sci + prs\_scw + prs\_rcs + prs\_ide - prs\_ihm - prr\_sml - sed\_s),$$

$$dq_g/dt = (+prg\_scw + prg\_rfz + prg\_gde + prg\_rcg + prg\_gcw + prg\_rci + prg\_rcs - prg\_ihm - prr\_gml + sed\_g),$$

References

Colle, B. A., and C. F. Mass, 2000: The 5-9 February 1996 flooding event over the Pacific Northwest: Sensitivity studies and evaluation of the MM5 precipitation forecasts. *Mon. Wea. Rev*., **128,** 593-617.

_____, M. F. Garvert, J. B. Wolfe, C. F. Mass and C. P. Woods, 2005: The 13-14 December 2001 IMPROVE-2 event. Part III: Simulated microphysical budgets and sensitivity studies. *J. Atmos. Sci.*, **62,** 3535-3558.

Ferrier, B. S., 1994: A double-moment multiple-phase four-class bulk ice scheme. Part I: Description. *J. Atmos. Sci.*, **51,** 249-280.

Fritsch, J. M., R. J. Kane, and C. R. Chelius, 1986: The contribution of mesoscale convective weather systems to the warm-season precipitation in the United States. *J. Climate Appl. Meteor.*, **25**, 1333-1345.

Gallus, W. A. Jr. and R. H. Johnson, 1995: The dynamics of circulations within the trailing stratiform regions of squall lines. Part I: The 10-11 June PRE-STORM system. *J. Atmos. Sci.*, **52,** 2161-2187.

_____, and M. Pfeifer, 2008: Intercomparision of simulations using 5 WRF microphysical schemes with dual-Polarization data for a German squall line. *Advances in Geosciences.*, **16**, 109-116.

Geresdi, I, 1998: Idealized simulation of the Colorado hailstorm case: comparison of bulk and detailed microphysics. *Atmospheric Research,* **45**, 237-252.

Gilmore, M. S., J. M. Straka and E. N. Rasmussen, 2004b: Precipitation uncertainty due to variations in precipitation particle parameters within a simple microphysics scheme. *Mon. Wea. Rev.,* **132,** 2610-2627.

Hong, S. –H., J. Dudhia and S. –H. Chen, 2004: A revised approach to ice microphysical processes for the bulk parameterization of clouds and precipitation. *Mon. Wea.Rev.,* **132,** 103-120.

_____ and J. O. Lim, 2006: The WRF single-moment 6-class microphysics scheme (WSM6). *Journal of the Korean Meteorological Society*, **42,** 129-151.

Jankov, I., W.A. Gallus Jr., M. Segal, B. Shaw and S. E. Koch, 2005: The impact of different WRF model physical parameterizations and their interactions on warm season MCS rainfall. *Wea. Forecasting.,* **20**, 1048-1060.

Lin, Y. –L., R. D. Farley and H. D. Orville, 1983: Bulk parameterization of the snow field in a cloud model. *J. Appl. Meteor.,* **22,** 1065-1092.

Lin, Y., B. A. Colle, C. Woods and B. F. Smull, 2006: Verification of WRF for the 4-5 December 2001 IMPROVE-2 event over the central Oregon Cascades. Preprints, *7th WRF Users' Workshop,* Boulder, CO, National Center for Atmospheric Research, P2-2.

_____and _____, 2008: The 4-5 December 2001 IMPROVE-2 Event: Observed Microphysics and Comparisons with the Weather Research and Forecasting Model. *Mon.Wea.Rev.,* **137,** 1372-1392.

Locatelli, J. D. and P. V. Hobbs, 1974: Fall speeds and masses of solid precipitation particles. *J. Geophys. Res.,* **79,** 2185-2197.

Lynn, B. H., A. P. Khain, J. Dudhia, D. Rosenfeld, A. Pokrovsky and A. Seifert, 2005: Spectral (Bin) microphysics coupled with a mesoscale model (MM5). Part II: Simulation of a CaPE rain event with a squall line. *Mon.Wea.Rev.*, **133,** 59-71.

_____ and _____, 2007: Utilization of spectral bin microphysics and bulk parameterization schemes to simulate the cloud structure and precipitation in a mesoscale rain event. *J. Geophys. Res.*, **112,** 22205, doi:10.1029/2007JD008475.

Marshall, J.S. and W. Mc K. Palmer, 1948: The distribution of raindrops with size. *Journal of Meteorology*., **5,** 165-166.

Matrosov, S. Y., A. V. Korolev and A. J. Heymsfield, 2002: Profiling cloud ice mass and particle characteristic size from Doppler radar measurements. *J. Atmos. Oceanic Technol.*, **19,** 1003-1018.

McCumber, M., W-K. Tao, J. Simpson, R. Penc ands-T Soong, 1991: Comparison of ice-phase microphysical parameterization schemes using numerical simulations of tropical convection. *J. Appl. Meteor.*, **30,** 985-1004.

Orr, B. W. and R. A. Kropfli, 1998: A method for estimating particle fall velocities from vertically pointing Doppler radar. *J. Atmos. Oceanic Technol.*, **16,** 29-37.

Parker, M.D. and R. H. Johnson, 2004: Structures and dynamics of quasi-2D mesoscale convective systems, *J. Atmos. Sci.*, **61,** 545-567.

Parsons, D., cited 2002: IHOP_2002 Water Vapor Intercomparisoins Workshop Presentations. [Available online at [http://www.atd.ucar.edu/dir_off/projects/2002/IHOPwsOct03

/presentations.html].

Potter, B. E., 1991: Improvements to a commonly used cloud microphysical bulk parameterization. *J. Appl. Meteor.,* **30,** 1040-1042.

Pruppacher, H. R., and J. D. Klett, 1978: *Microphysics of Clouds and Precipitation.* D. Reidel, 714 pp..

Rasmussen, R. M. and A. J. Heymsfield, 1987: Melting and shedding of graupel and hail. Part I: Model physics. *J. Atmos. Sci.*, **44,** 2754-2763.

_____, I. Geresdi, G. Thompson, K, Manning and E. Karplus, 2002: Freezing drizzle formation in stably stratified layer clouds: The role of radiative cooling of cloud droplets, cloud condensation nuclei, and ice initiation. *J. Atmos. Sci.*, **59,** 837-860.

Skamarock, W.C., J.B. Klemp, J. Dudhia, D.O. Gill, D.M. Barker, W. Wang, and J.G. Powers, 2005: A description of the advanced research WRF version 2. NCAR Tech. Note NCAR/TN-468+STR, 88 pp. [Available online at http://www.wrf-model.org/wrfadmin/docs/arw_v2.pdf]

Thompson, G., P. R. Field, R. M. Rasmussen, and W. D. Hall 2008: Explicit forecasts of winter precipitation using an improved bulk microphysics scheme. Part II: Implementation of a new snow parameterization. *Mon.Wea.Rev.*, **136,** 5095-5115.

Walko, R. L., W. R. Cotton, M. P. Meyers, and J. Y. Harrington, 1995: New RAMS cloud microphysics parameterization. Part I: The single-moment scheme. *Atmos. Res.*, **38**, 29–62.

Verlinde, J., P. J. Flatau, and W. R. Cotton, 1990: Analytical solutions to the collection growth equation: Comparison with approximate methods and application to the cloud microphysics parameterization schemes. *J. Atmos. Sci.*, **47**:2871–2880.

Weisman, M. L., J. B. Klemp, and R. Ruttunno, 1988: Structure and evolution of numerically simulated squall lines. *J. Atmos. Sci.*, **45**, 1990-2013.

List of Figures

Figure. 1. Percentage contribution of the indicated microphysical processes to the total microphysical budget for particles with different rain fall speeds for (a) Geresdi, (b) Thompson, (c) WSM6 and (d) Lin. Processes indicated for each scheme are those that contribute positively to the rain water mixing ratios. The blue, red and green bars correspond to the fall speed ranges indicated in the inset in (a). Some of the processes are defined as follows: RCW: Rain collecting cloud water, DIFF: water vapor diffuision onto cloud condensation nuclei (CCN) , RAUT: autoconversion of cloud water to rain water, RCG: rain collecting graupel, CND: rain condenstion, SCW: snow collecting cloud water, GCW: graupel collecting cloud wate, RCS: rain collecting snow and SGCW: accretion of cloud water by averaged snow/graupel.

Figure 2. Same as in Fig. 1 but with the average microphysical scheme value used for WVL in (4).

Figure 3. Rain (in addition to cloud water in Geresdi) fall speed distributions for all schemes as indicated in the inset. Note that rain particles in Geresdi are those with fall speeds above 0.0933 m s^{-1}. The blue, red and green horizontal lines along the abscissa highlight the three fall speed segments used for the budget analysis and in the vertical cross sections in Fig 1. and Fig. 3, respectively.

Figure 4. Vertical cross sections of total condensate (only the 0.1 g kg^{-1} contour is shown) and rain fall speeds (shaded) four hours into the simulations for (a) Geresdi, (b) Thompson, (c) WSM6 and (d) Lin. In each cross-section, the system is moving from left to right, and the horizontal grid points are located along the abscissa.

Figure 5. Same as in Fig. 1 but for snow. Some of the processes are defined as follows: SDEP: snow deposition, SCI: snow collecting ice, SCW: snow collecting water, SAUT: autoconversion of cloud ice to snow, RCS: rain collecting snow, RCI: rain collecting cloud ice, ICR: cloud ice collecting rain, Berg1: the reduction of cloud ice by Bergeron process, Berg2: Bergeron process (deposition and riming)-transfer of cloud water to form snow.

Figure 6. Snow fall speed distributions for all schemes as indicated in the inset. The blue, red and green horizontal lines along the abscissa highlight the three fall speed segments used for the budget analysis and in the vertical cross sections used in Fig 4. and Fig. 6, respectively.

Figure 7. Same as in Fig. 3, but for snow.

Figure 8. Hovmöller diagram of rainfall rate (in. h^{-1}; 1 in. = 25.4 mm) for (a) Geresdi, (b) Thompson, (c) WSM6 and (d) Lin. The horizontal grid points are located along the abscissa.

Figure 9. Time series of domain-averaged upward vertical velocities in m s^{-1} for the microphysical schemes indicated in the inset.

Figure 10. Vertical cross section of time-domain-averaged liquid (cloud water and rain water) evaporation rate (g kg^{-1} 10 min^{-1}) for (a) Geresdi, (b) Thompson, (c) WSM6 and (d) Lin. The horizontal grid points are located along the abscissa.

Figure 11. Same as in Fig. 1 but for graupel. Some of the processes are defined as follows: RFRZ: rain freezing, RCS: rain collecting snow, RCG: rain collecting graupel, RCI: rain collecting ice, GDEP: graupel deposition, RCG: rain collecting graupel, GCW: graupel collecting cloud water, GAUT: autoconversion of snow to graupel, GCI: graupel collecting ice, SCR: snow collecting rain, GCS: graupel collecting snow, ICR: ice collecting rain.

Figure 12. Graupel fall speed distributions for all schemes as indicated in the inset. The blue, red and green horizontal lines along the abscissa highlight the three segments of fall speeds used in Fig 10. and Fig. 12.

Figure 13. Same as in Fig. 3, but for graupel.

Figure 14. Same as in Fig. 2, but for cloud ice. Some of the processes are defined as follows: CWF: cloud water freezing, IDEP: cloud ice deposition, CNDF: condensation freezing, IMRS: ice multiplication from rime-splinters.

Figure 15. Cloud ice fall speed distributions for all schemes as indicated in the inset. The blue and green horizontal lines along the abscissa highlight the three segments of fall speeds used in Fig 13. and Fig. 15.

Figure 16. Same as in Fig. 3, but for cloud ice.

Figure. 17. Fall speed distributions for all schemes as indicated in the inset, and for the LS simulation for (a) rain, (b) snow, (c) graupel and (d) cloud ice. Note that rain particles in Geresdi are those with fall speeds above 0.0933 m s^{-1}.

List of Tables

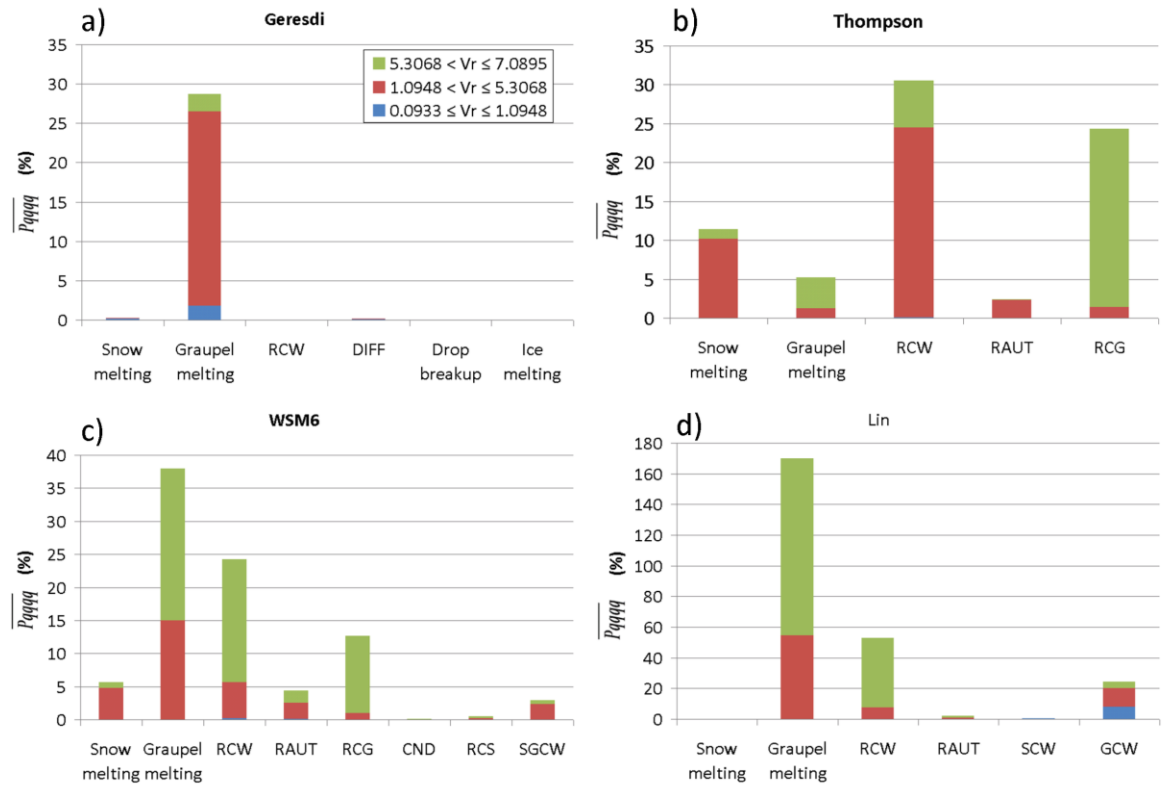

Fig. 1. Percentage contribution of the indicated microphysical processes to the total microphysical budget for particles with different rain fall speeds for (a) Geresdi, (b) Thompson, (c) WSM6 and (d) Lin. Processes indicated for each scheme are those that contribute positively to the rain water mixing ratios. The blue, red and green bars correspond to the fall speed ranges indicated in the inset in (a). Some of the processes are defined as follows: RCW: Rain collecting cloud water, DIFF: water vapor diffuision onto cloud condensation nuclei (CCN) , RAUT: autoconversion of cloud water to rain water, RCG: rain collecting graupel, CND: rain condenstion, SCW: snow collecting cloud water, GCW: graupel collecting cloud wate, RCS: rain collecting snow and SGCW: accretion of cloud water by averaged snow/graupel.

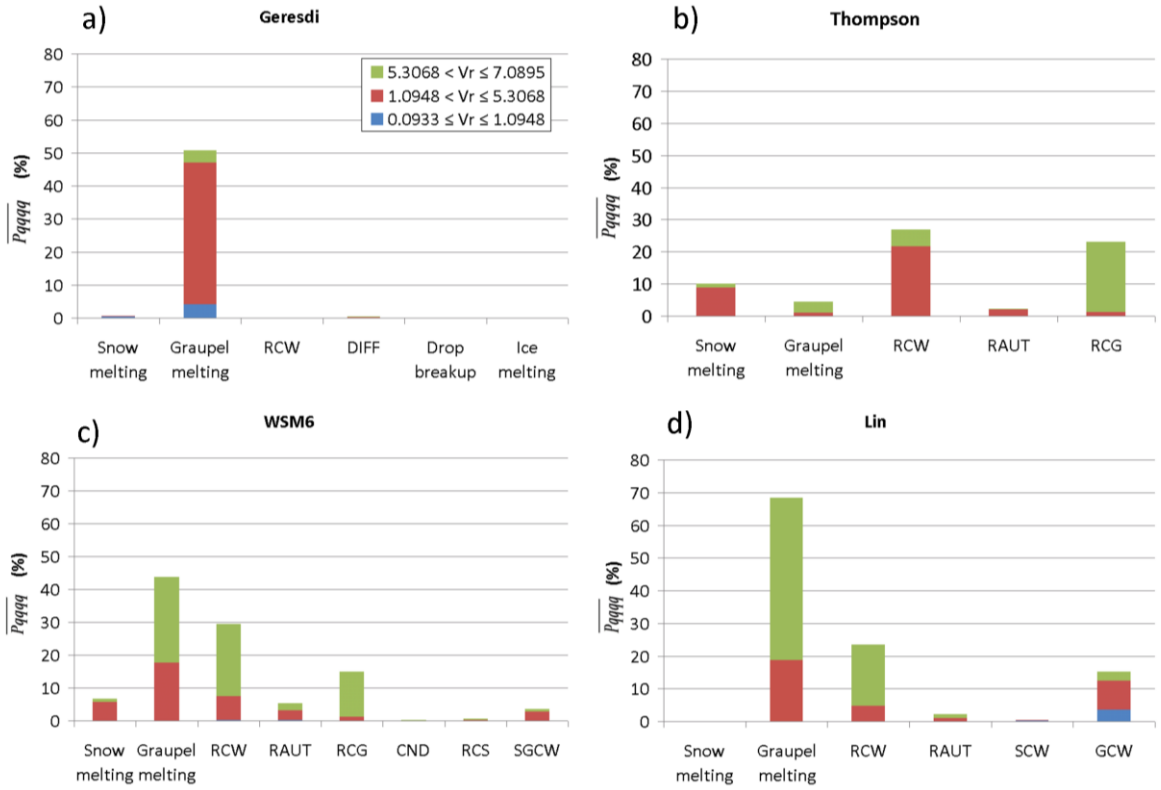

Fig. 2. Same as in Fig. 1 but with the average microphysical scheme value used for WVL in (4).

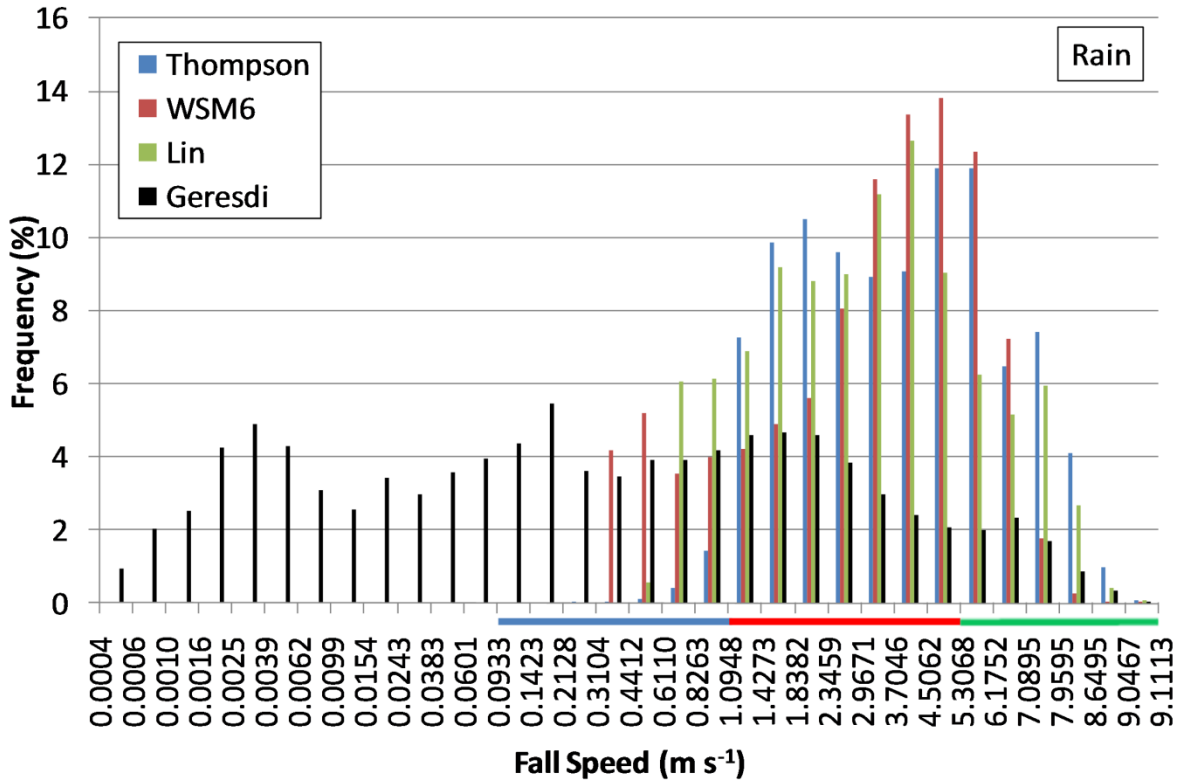

Fig. 3. Rain (in addition to cloud water in Geresdi) fall speed distributions for all schemes as indicated in the inset. Note that rain particles in Geresdi are those with fall speeds above 0.0933 m s^{-1}. The blue, red and green horizontal lines along the abscissa highlight the three fall speed segments used for the budget analysis and in the vertical cross sections in Fig 1. and Fig. 4, respectively.

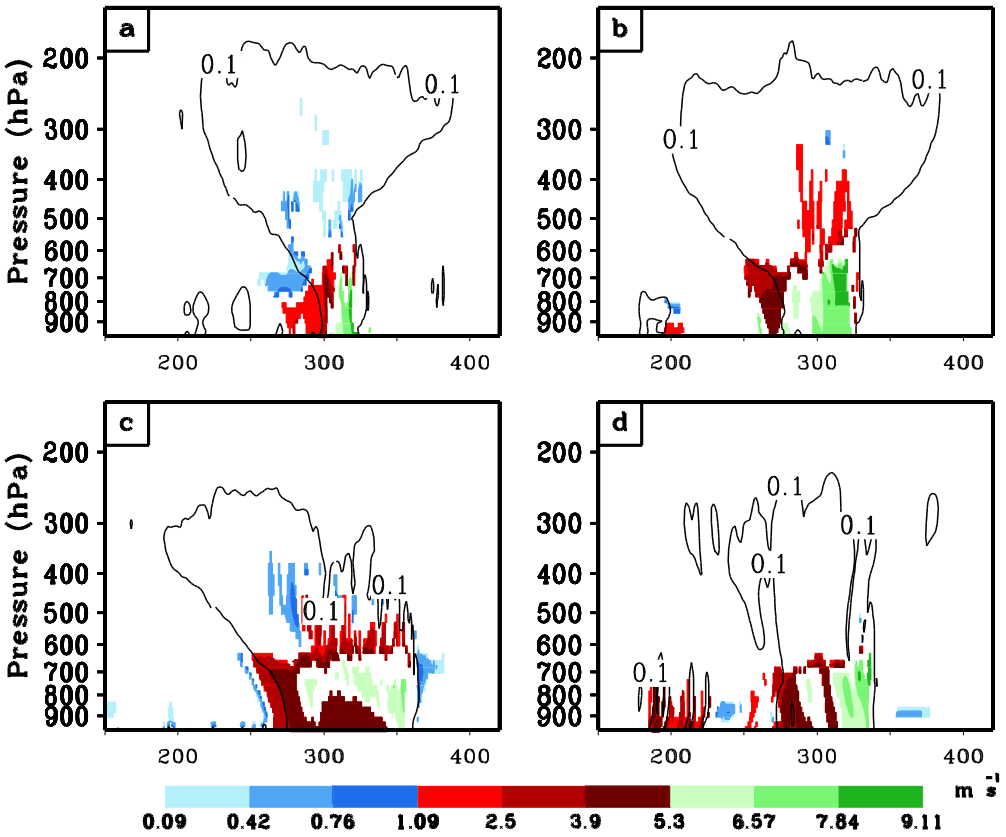

Fig. 4. Vertical cross sections of total condensate (only the 0.1 g kg^{-1} contour is shown) and rain fall speeds (shaded) four hours into the simulations for (a) Geresdi, (b) Thompson, (c) WSM6 and (d) Lin. In each cross-section, the system is moving from left to right, and the horizontal grid points are located along the abscissa.

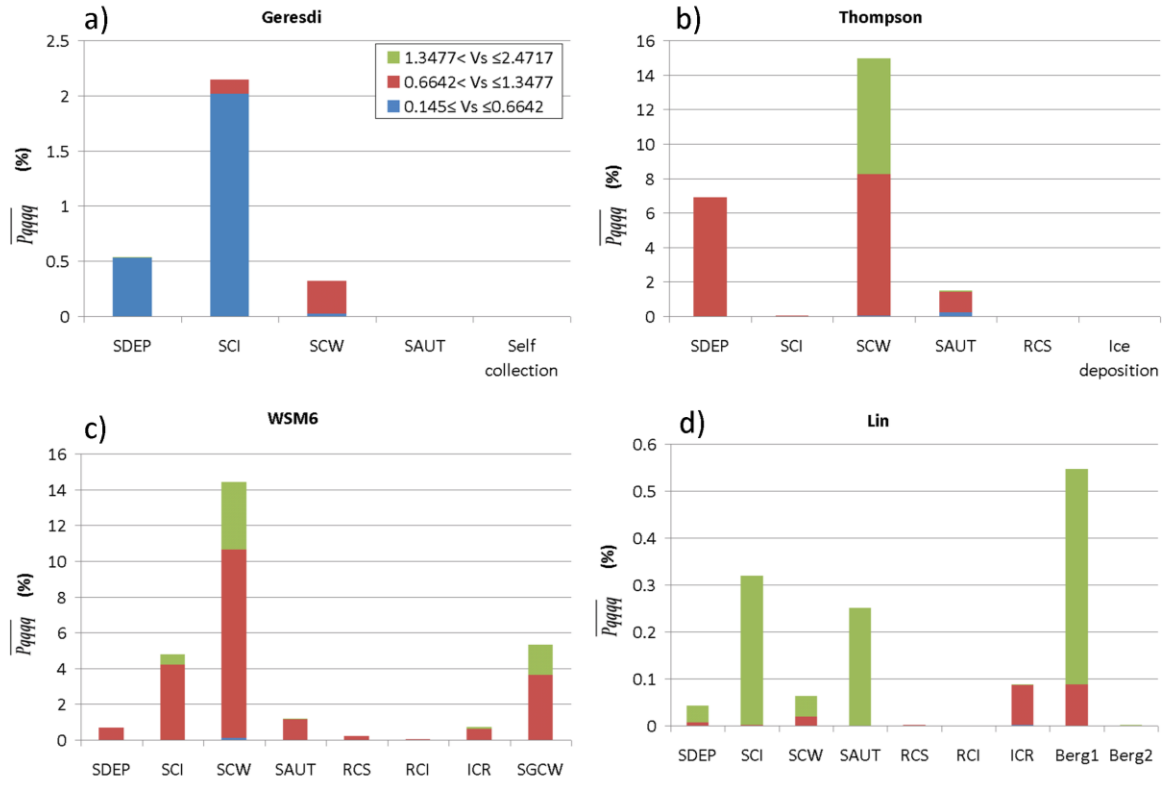

Fig. 5. Same as in Fig. 1 but for snow. Some of the processes are defined as follows: SDEP: snow deposition, SCI: snow collecting ice, SCW: snow collecting water, SAUT: autoconversion of cloud ice to snow, RCS: rain collecting snow, RCI: rain collecting cloud ice, ICR: cloud ice collecting rain, SGCW: accretion of cloud water by averaged snow/graupel, Berg1: the reduction of cloud ice by Bergeron process, Berg2: Bergeron process (deposition and riming)-transfer of cloud water to form snow.

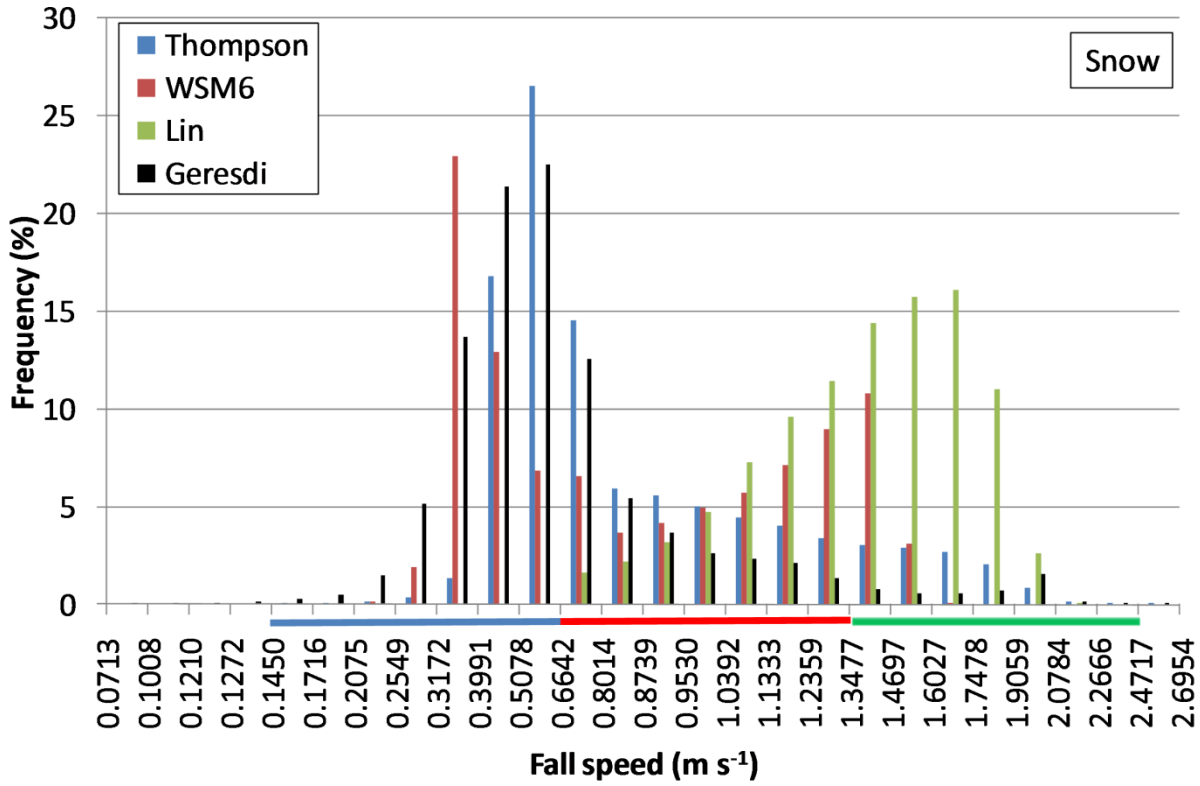

Fig. 6. Snow fall speed distributions for all schemes as indicated in the inset. The blue, red and green horizontal lines along the abscissa highlight the three fall speed segments used for the budget analysis and in the vertical cross sections used in Fig 5. and Fig. 7, respectively.

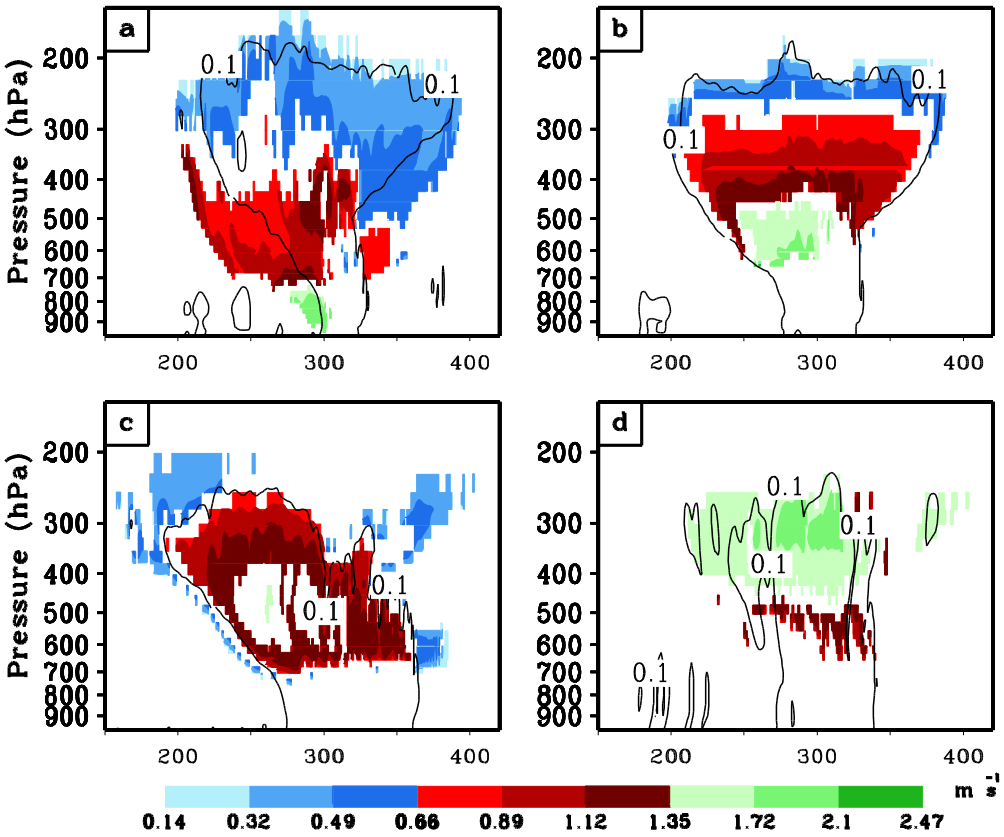

Fig.7. Same as in Fig. 4, but for snow.

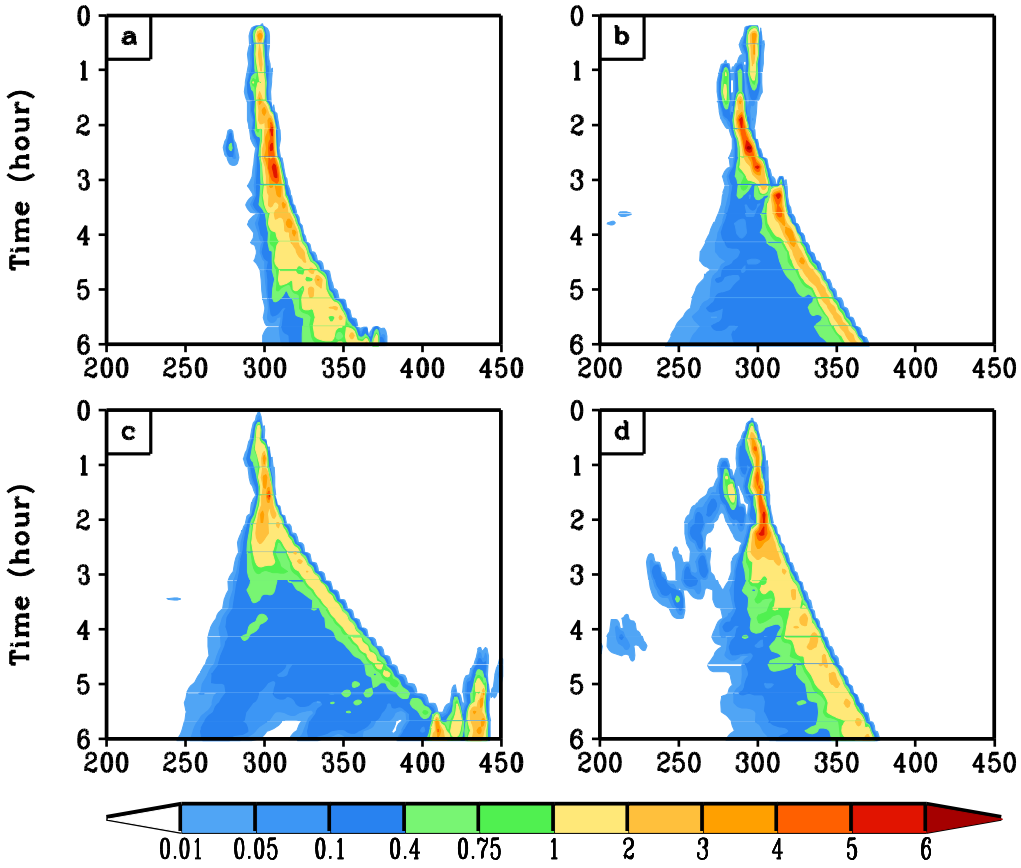

Fig. 8. Hovmöller diagram of rainfall rate (in. h^{-1}; 1 in. = 25.4 mm) for (a) Geresdi, (b) Thompson, (c) WSM6 and (d) Lin. The horizontal grid points are located along the abscissa.

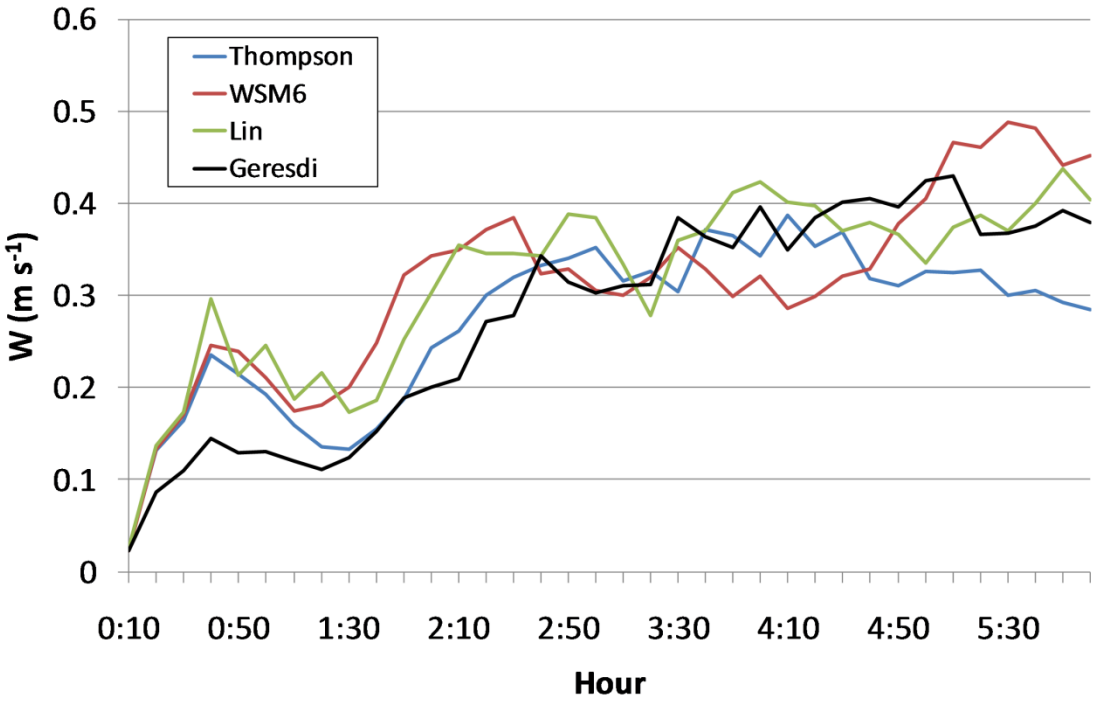

Fig. 9. Time series of domain-averaged upward vertical velocities in m s^{-1} for the microphysical schemes indicated in the inset.

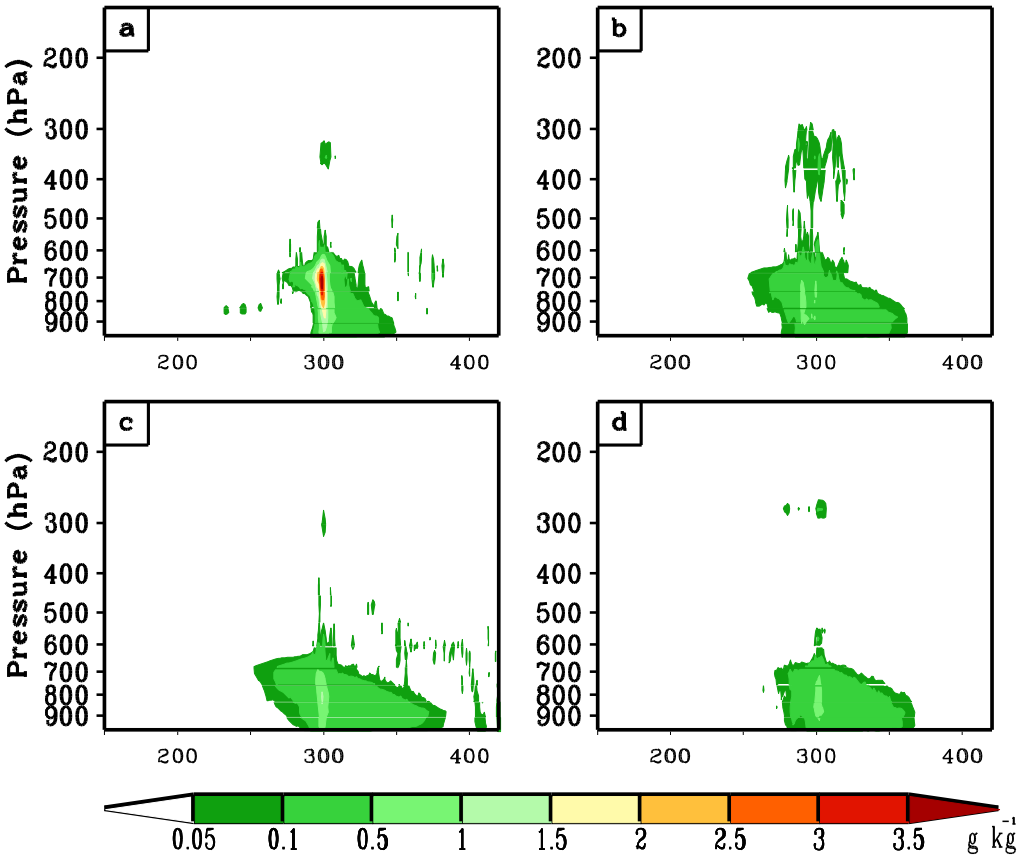

Fig. 10. Vertical cross section of time-domain-averaged liquid (cloud water and rain water) evaporation rate (g kg^{-1} 10 min^{-1}) for (a) Geresdi, (b) Thompson, (c) WSM6 and (d) Lin. The horizontal grid points are located along the abscissa.

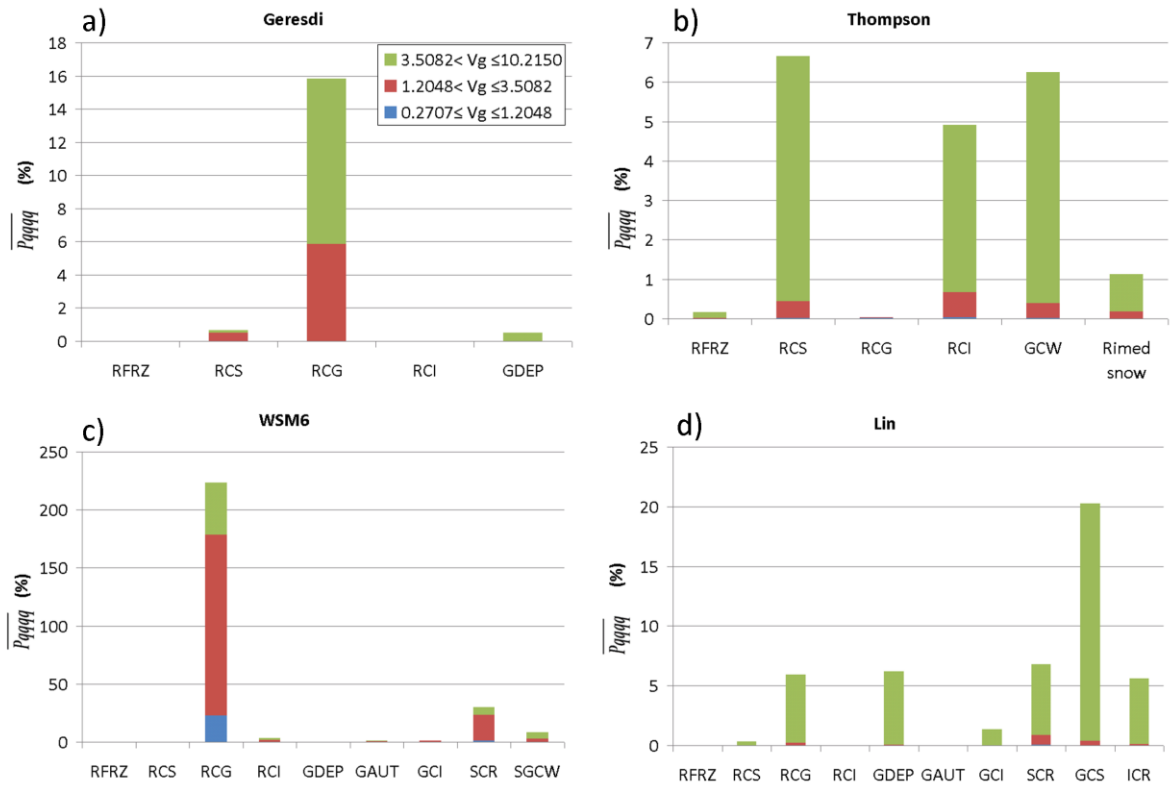

Fig. 11. Same as in Fig. 1 but for graupel. Some of the processes are defined as follows: RFRZ: rain freezing, RCS: rain collecting snow, RCG: rain collecting graupel, RCI: rain collecting ice, GDEP: graupel deposition, RCG: rain collecting graupel, GCW: graupel collecting cloud water, GAUT: autoconversion of snow to graupel, GCI: graupel collecting ice, SCR: snow collecting rain, GCS: graupel collecting snow, ICR: ice collecting rain, SGCW: accretion of cloud water by averaged snow/graupel.

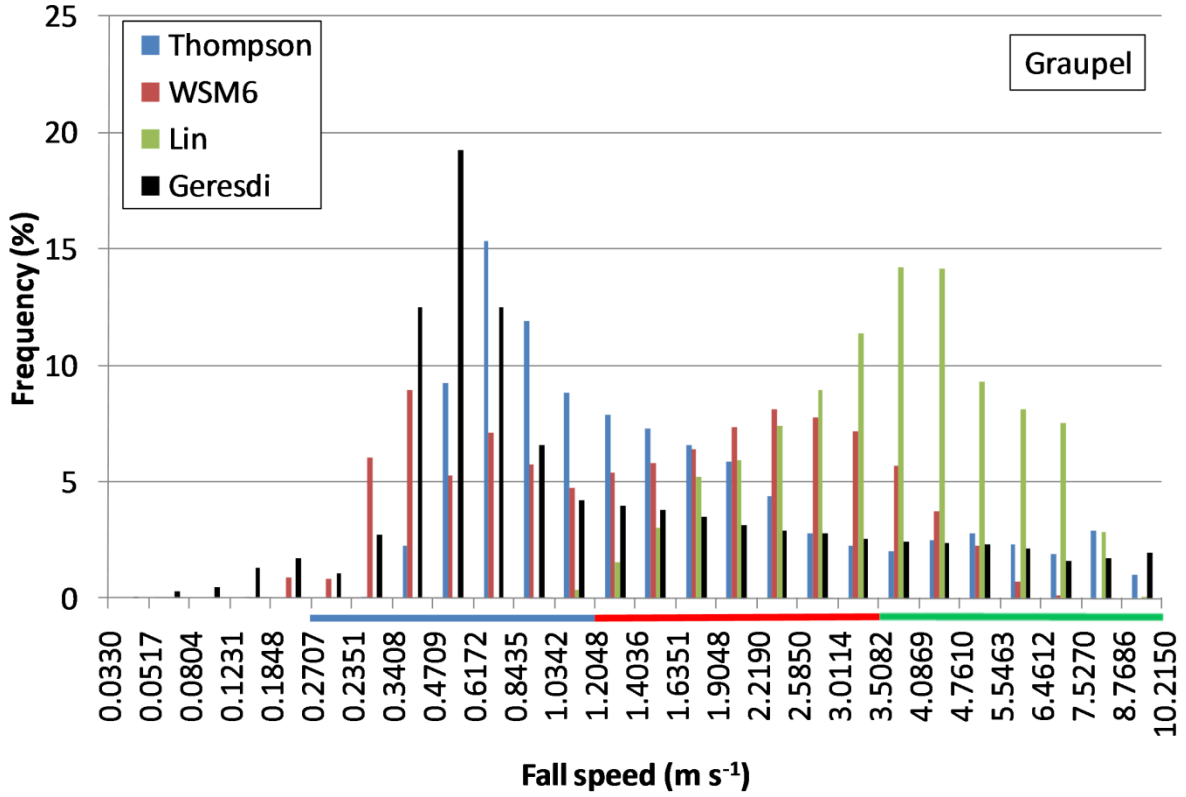

Fig. 12. Graupel fall speed distributions for all schemes as indicated in the inset. The blue, red and green horizontal lines along the abscissa highlight the three segments of fall speeds used in Fig 11. and Fig. 13.

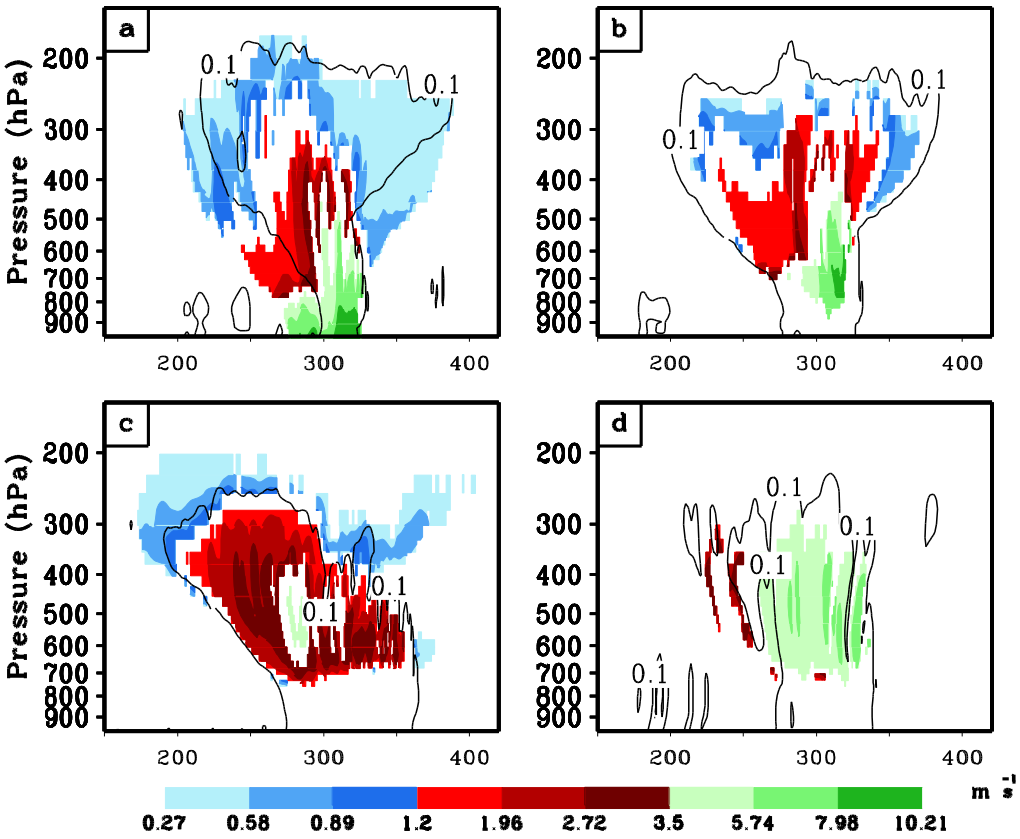

Fig. 13. Same as in Fig. 4, but for graupel.

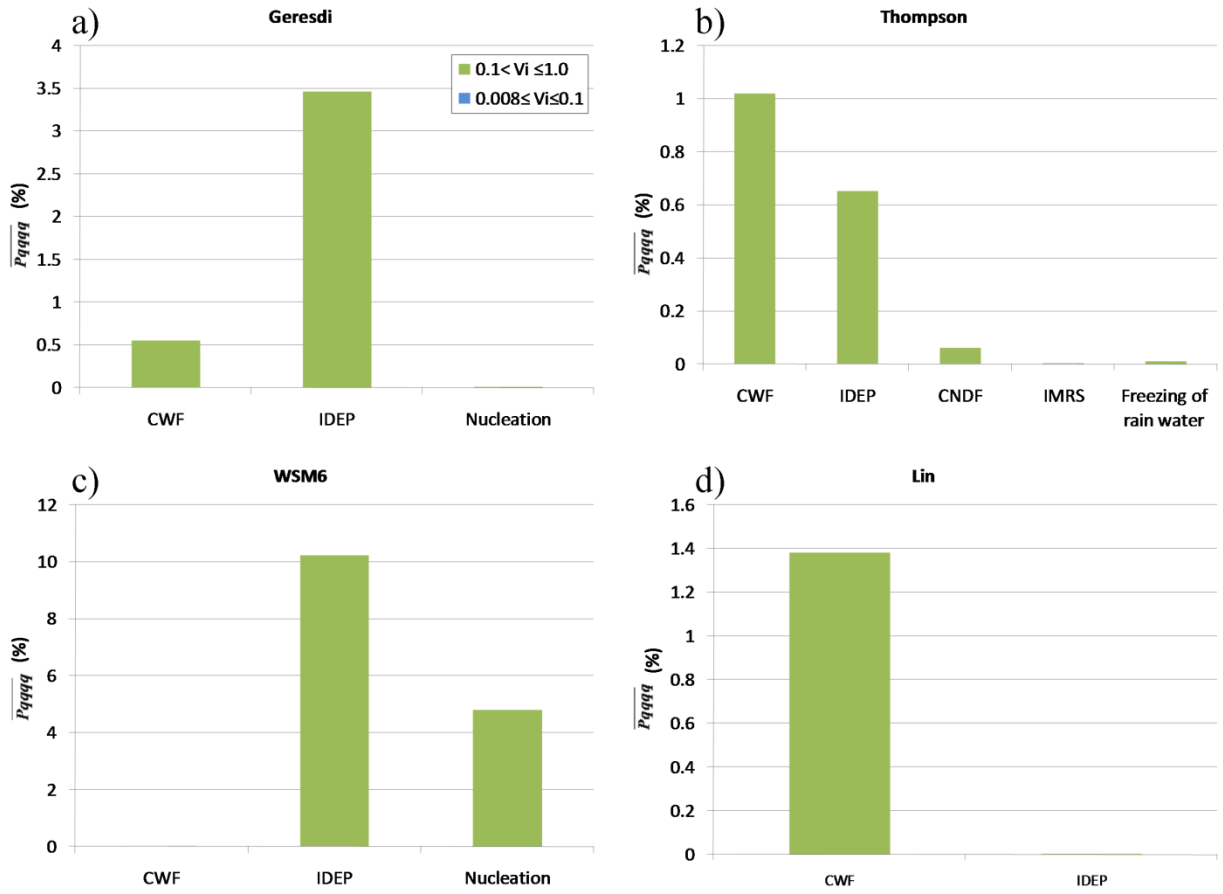

Fig. 14. Same as in Fig. 1, but for cloud ice. Some of the processes are defined as follows: CWF: cloud water freezing, IDEP: cloud ice deposition, CNDF: condensation freezing, IMRS: ice multiplication from rime-splinters.

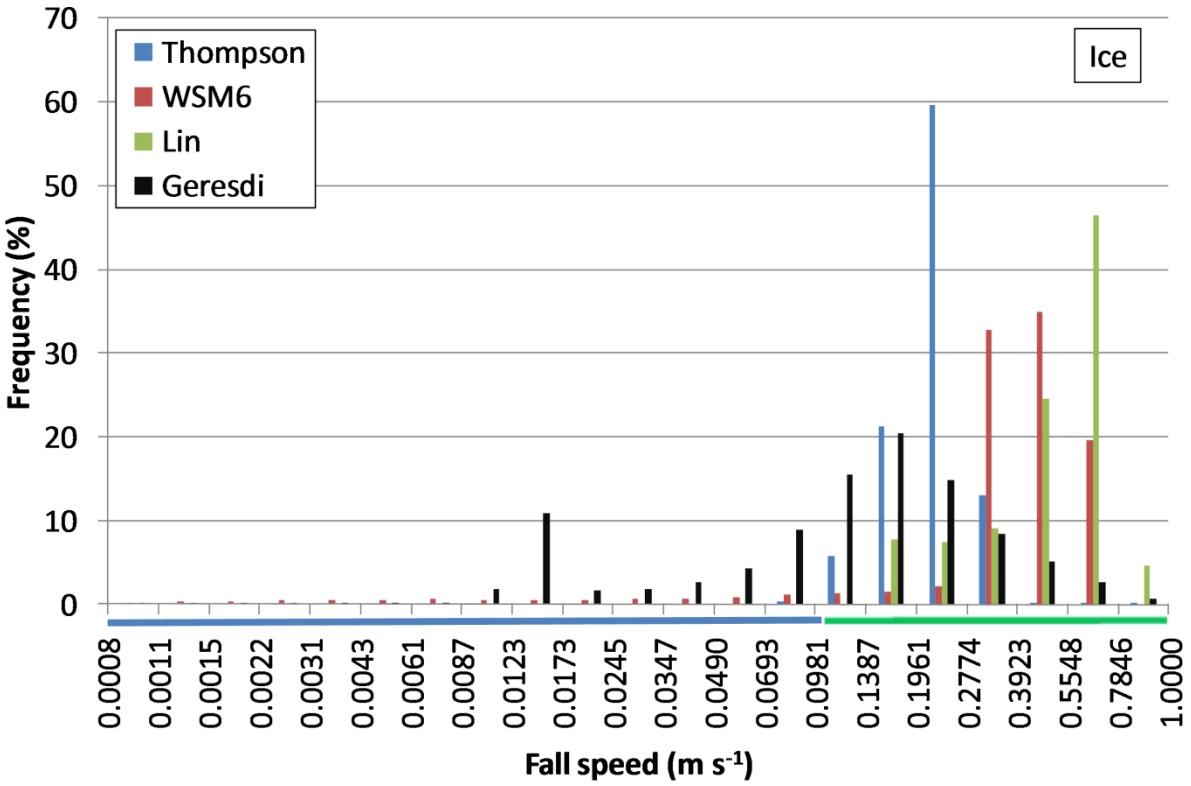

Fig. 15. Cloud ice fall speed distributions for all schemes as indicated in the inset. The blue and green horizontal lines along the abscissa highlight the three segments of fall speeds used in Fig 14. and Fig. 16.

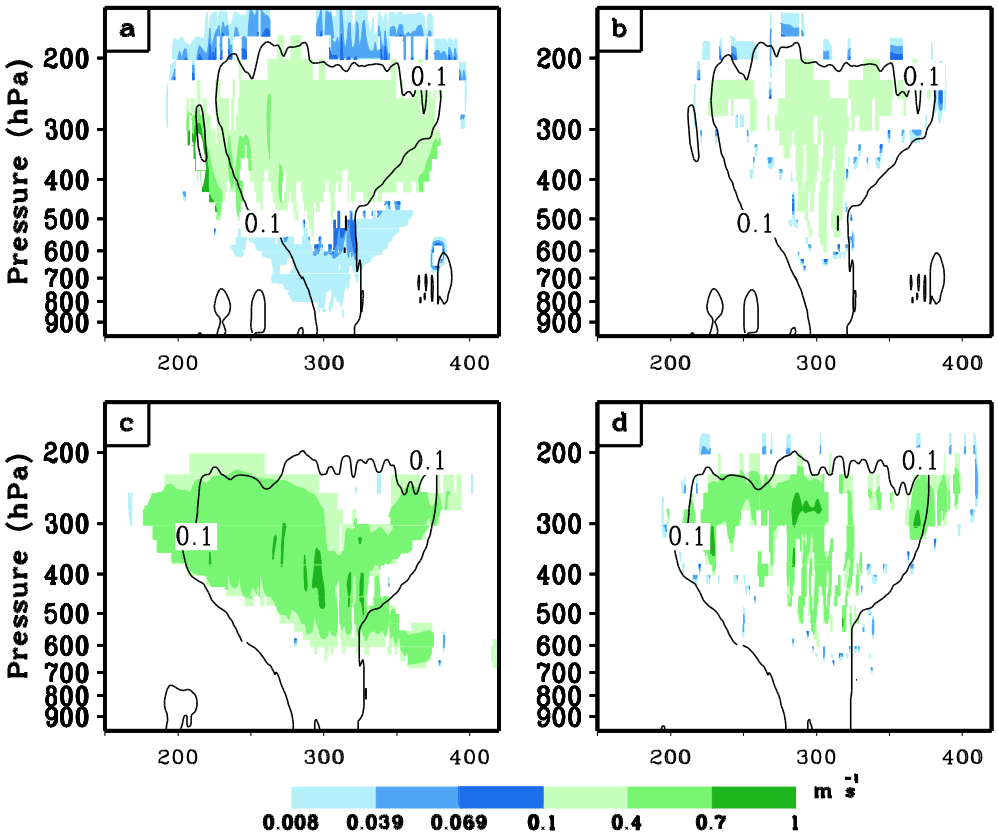

Fig. 16. Same as in Fig. 4, but for cloud ice.

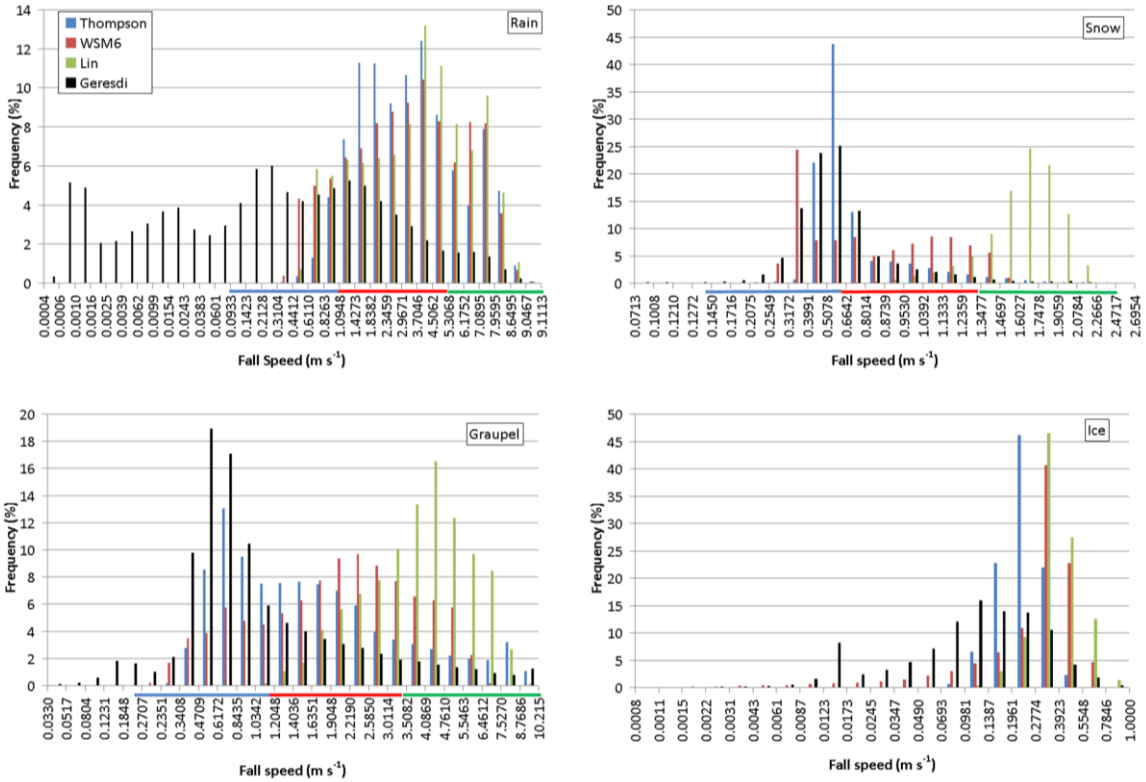

Fig. 17. Fall speed distributions for all schemes as indicated in the inset, and for the LS simulation for (a) rain, (b) snow, (c) graupel and (d) cloud ice. Note that rain particles in Geresdi are those with fall speeds above 0.0933 m s^{-1}.

Table 1. Alphabetical listing and definitions of the Thompson source/sink terms indicated in the appendix. Units of these processes are in kg kg^{-1}.

Prg_gcw	graupel collecting cloud water
Prg_gde	graupel deposition/sublimation
Prg_ihm	ice multiplication from rime-splinters
Prg_rcg	rain collecting graupel
Prg_rci	rain collecting cloud ice
Prg_rcs	rain collecting snow
Prg_rfz	freezing of rain water into graupel
Prg_scw	rimed snow becoming graupel
Pri_rci	rain collecting ice
Pri_ide	deposition/sublimation of cloud ice
Pri_ihm	ice multiplication from rime-splinters
Pri_inu	condensation freezing
Pri_rfz	freezing rain water into cloud ice
Pri_wfz	freezing of cloud water into cloud ice
Prr_gml	graupel melting
Prr_rcg	rain collecting graupel
Prr_rci	rain collecting cloud ice
Prr_rcs	rain collecting snow
Prr_rcw	rain collecting cloud water
Prr_sml	snow melting
Prr_wau	autoconversion of cloud water to rain
Prs_iau	autoconversion of cloud ice to snow
Prs_ide	ice deposition/sublimation
Prs_ihm	ice multiplication from rime-splinters
Prs_rcs	rain collecting snow
Prs_sci	snow collecting cloud ice
Prs_scw	snow collecting cloud water
Prs_sde	snow deposition/sublimation
Prv_rev	rain evaporation
Prw_vcd	cloud water condensation/evaporation
Sed_g	sedimentation of graupel
Sed_i	sedimentation of ice
Sed_r	sedimentation of rain
Sed_s	sedimentation of snow

Table 2. Coeficients used in Eq.(1) for the indicated hydrometeors of the four microphysical schemes as well as the prescribed reference density, ρ_o, used in the fall speed relations. Units of mass, m , are in kg.

Scheme Hydrometeor	α	β	f	ρ_o
Geresdi				1.20
Liquid	(Pruppacher and Klett 1997)			
Cloud ice	304	1	0	
Snow	$\alpha = \begin{cases} 1250, & \mathrm{m} < 5.654 \cdot 10^{-9} \\ 4.84, & \mathrm{m} \geq 5.654 \cdot 10^{-9} \end{cases}$ $\beta = \begin{cases} 1, & m < 5.654 \cdot 10^{-9} \\ 0.25, & m \geq 5.654 \cdot 10^{-9} \end{cases}$ $f = 0$			
Graupel	(Rasmussen and Hyemsfield 1987)			
Thompson				1.18
Rain	4854	1	195	
Cloud ice	1847.5	1	0	
Snow	40	0.55	125	
Graupel	442	0.89	0	
WSM6				1.28
Rain	841.9	0.8	0	
Cloud ice	1490	1.31	0	
Snow	11.72	0.41	0	
Graupel				
Lin				1.29
Rain	841.9	0.8	0	
Cloud ice		(see text)		
Snow	4.836	0.25	0	
Graupel		(see text)		

CHAPTER 3: ON THE IMPACT OF WRF MODEL VERTICAL GRID RESOLUTION ON MIDWEST SUMMER RAINFALL FORECASTS

Eric A. Aligo*

William A. Gallus, Jr.*

and

Moti Segal[+]

* Dept. of Geological and Atmospheric Sciences

Iowa State University

Ames, IA

[+]Dept. of Agronomy

Iowa State University

Ames, IA

(submitted to Weather and Forecasting December 07, 2007; revised May 26, 2008; revised August 29, 2008)

Corresponding author address: Eric A. Aligo, Iowa State University, 3010 Agronomy Hall,

Ames, IA , 50011 email: ealigo@iastate.edu

Abstract

Weather Research and Forecast (WRF) model exploratory sensitivity simulations were performed to determine the impact of vertical grid resolution (VGR) on the forecast skill of Midwest summer rainfall. Varying the VGR indicated that a refined VGR, while adopting the widely used North America Regional Reanalysis (NARR) for initial and lateral boundary conditions, does not necessarily result in a consistent improvement in quantitative precipitation forecasts (QPF). When averaged over a variety of microphysical schemes in an illustrative case, Equitable Threat Score (ETS) and Bias values actually worsened with a greater overpredicted rainfall for half of the rainfall thresholds when the VGR was refined. Averaged over strongly forced cases, ETS values worsened for all rainfall thresholds while Biases mostly increased, indicating a further overprediction of rainfall when the number of levels was increased. Skill improved, however, for all rainfall thresholds when the resolution above the melting level was increased. Skill also improved for most rainfall thresholds when the resolution in the surface layer was increased, attributed to better resolved surface turbulent momentum and thermal fluxes. Likewise, a refined VGR resulted in improvements in weakly forced cases, which are governed mostly by thermodynamic forcing and are sensitive to vertical profiles of temperature and moisture. Application of the factor separation method suggested that the refined VGR more frequently had a negative impact on skill through the interaction between lower atmospheric processes and microphysical processes above the melting level.

1. Introduction

The continuous increase in computer power has led gradually to an increase in horizontal and vertical grid resolution (VGR) in models used to forecast summer convection. One of the aims of improving horizontal grid resolution is to reach a grid spacing believed to be sufficient to explicitly resolve convection. However, an increase in horizontal grid resolution has not always led to a clear improvement in quantitative precipitation forecasts (QPF) as evaluated by various skill measures (Mass et al. 2002 ; Roebber et al 2004). Much less attention has been given to evaluating the related refinements of VGR on QPF skill.

Recently Zhang and Wang (2003) and Kimball and Dougherty (2006) demonstrated in illustrative case studies a significant improvement of simulated hurricane intensity and structure while testing several variants of refined VGR. A similar type of evaluation of the impact of VGR on summer continental convection has not been reported, hence it will be beneficial to provide initial insight into this issue. Considering this objective, the present study provides an illustrative evaluation of QPF sensitivity to refinements in VGR in a cloud-permitting mesoscale model while applied to summer convection in the Midwest. The study is exploratory and oriented toward the resources available in the operational environment.

Addressing the above objective, the following pertinent issues are worth pointing out. Conceptually, for rainfall forecasts, the model should acquire a vertical resolution that is more refined than that of the atmospheric initial conditions (IC) and lateral boundary conditions (LBC) for two reasons: i) the vertical profiles of the IC and LBC (which are embedding observations) are not adversely affected, as would be the case when the model VGR is coarser than that of the IC and LBC, and ii) an increased VGR should improve the simulated vertical structure of the

predicted fields. Considering (i)-(ii) above, examples of several relevant features affecting convection and their sensitivity to VGR are outlined:

- The higher the VGR of the IC and LBC, the more likely that refined observed features, such as the convective boundary layer (CBL) capping inversion, sharp wind shear, and low-level jets can be captured more accurately, thus improving the introduction of thermodynamic and some dynamical forcing.
- In mesoscale models, the cloud microphysical processes are resolved typically with a coarser VGR with increasing height, and conceptually they are likely to be improved with an increased VGR.
- Physically, an adequate computation of the surface turbulent momentum and thermal fluxes requires that at least the first model level be in the surface layer.

We pursued the study objective using a near-cloud-permitting configuration of the Weather Research and Forecasting (WRF) Advanced Research WRF (ARW) model, hereafter termed WRF, and North American Regional Reanalysis (NARR) data focusing on illustrative simulations of Midwest summer rainfall. Since the WRF model and NARR are both widely used, this study acquires additional merit. Control simulations with the WRF default VGR were used as a reference to simulations carried out using various increased and reduced VGRs. The results presented here are based on a total of 68 simulations. The study methodology is described in section 2, followed by quantitative results in section 3 and qualitative evaluations in section 4.

2. Methodology

a. Model Setup and Data

The WRF model (Skamarock et al. 2005) was run with a 4 km domain nested within a 12 km domain using a two-way nested interface (Fig. 1) with the simulated cases located in the central United States. The model physical configuration is that described in Aligo et al. (2007) with the exception of the planetary boundary layer (PBL) scheme and the land surface model (LSM), which in the present study are, respectively, the Mellor-Yamada-Janjic (MYJ; Janjic 2002) scheme and the Noah LSM (Ek et al. 2003). In addition to the above configuration, the 12 km outer nest used the Betts-Miller-Janjic convective scheme (Betts 1986; Betts and Miller 1986; Janjic 1994), which currently is used operationally at NCEP. Bryan et al. (2003) point out that a more realistic depiction of moist convection is likely with a horizontal grid spacing O(100 m), but because such grid spacing is not likely to be used operationally in the near future, the horizontal grid spacing of 4 km used in this study is a compromised choice considering the operational orientation of the paper.

The NARR, which is used in the present study, contains data on 29 pressure levels with a vertical grid spacing of 25 hPa below 700 hPa and above 300 hPa and a vertical grid spacing of 50 hPa between these two levels.

There are three approaches that could be adopted in the present study. The first involves very few simulations while focusing on comprehensive analyses. The second involves the computation of seasonal statistics, which will provide more accurate statistical results, however, it is typically not associated with case analyses. The third approach, which was adopted in the

study, is an exploratory one. It provides some statistics (based on 68 simulations in the present study) showing variability from case to case and provides initial insight into identifiable causes of some of the patterns. Since the model formulations and initial conditions are incomplete, and atmospheric processes are nonlinear, it is difficult to establish a direct relation between specific processes and VGR impacts on model QPF.

The evaluations focus on seven illustrative cases, five of which (18-19 June 2002, 20-21 June 2003, 22-23 June 2003, 23-24 June 2003 and 28-29 June 2003) were initialized at 18 UTC and integrated over an 18 hour period using the NARR for the IC and LBC. These five cases represent various strongly forced warm season convective systems (linear systems including bowing, parallel, leading and trailing stratiform as well as nonlinear systems; Grams et al. 2006) mostly from the Bow Echo and Mesoscale Convective Vortex Experiment (BAMEX; Davis et al. 2004). For added insight, the remaining two cases are weakly forced, i.e. mainly thermodynamically forced, and are 20-21 June 2005 and 24-25 July 2005. The weakly forced events were defined to be those associated with weak mid-upper level winds (500 hPa winds less than 15 m s^{-1}) and either weak frontal systems (near-surface cross-frontal horizontal temperature gradients less than 5° C over 100 km), no frontal systems at all, or only outflow boundaries in the region near the convection. Strongly forced events had 500 hPa winds of at least 20 m s^{-1} and/or near-surface cross-frontal horizontal temperature gradients of at least 7°C over 100 km (used in Aligo et al. 2007). The cases in this study were chosen carefully such that most of the simulated rainfall occurred after 6 hours into the model integration, enough time to avoid model spin-up errors found to exist in the first 3-5 hours of 4 km WRF simulations performed by Weisman et al. (2004).

b. Experimental design

The default number of levels likely used by WRF users is 31, and thus a run using these levels was considered the control run (note that for this run the VGR above 1 km becomes relatively coarse) and is denoted as 31L. To evaluate the sensitivity of QPF to VGR, runs with various grid configurations were carried out, in addition to that of 31L. These runs include 21, 33 and 62 levels (hereafter these runs are denoted, respectively, as: 21L, 33L and 62L). In addition, runs were performed with 57 levels with doubled resolution from 31L above 3.5 km (approximately the height where the temperature is 0°C; henceforth termed melting level), and 37 levels with doubled resolution from 31L below 3.5 km (hereafter these runs are denoted, respectively, as UPL and DNL). Figure 2 illustrates the heights of the model levels above the surface for each of these runs and the heights above sea level for the NARR. The 21L runs were done for comparative purposes only as degradation in QPF skill would be anticipated, particularly considering this VGR is coarser than that of the IC and LBC data from the NARR. The first level in 31L (54 m above surface) might be too high to resolve adequately the surface turbulent momentum and thermal fluxes, particularly under thermal stable conditions (Wei et al. 2001). Therefore, the 33L run used the levels in the 31L run and additional levels at 10 m and 25 m to improve the resolution of surface layer processes. In run 62L, the number of levels was doubled from 31L, hence providing an improved VGR. Run DNL should resolve better boundary layer and warm cloud processes, whereas run UPL should resolve better cloud microphysical processes above the melting level.

It should be noted that Lindzen and Fox-Rabinovitz (1989) and Pecnick and Keyser (1989) indicated needed constraints on the ratio between the vertical and the horizontal grid

resolutions to avoid the formation of spurious gravity waves. However, because of the horizontal eddy diffusion/filter damping effects in models, it is assumed that the suggested constraints are practically nonessential (Lindzen and Fox-Rabinovitz 1989). While varying the VGR in the present study, it was important to ensure that such spurious gravity waves were not present, and an examination of the model simulations revealed no such waves, consistent with findings in other mesoscale model convection studies (e.g. Roebber and Eise 2001; Jewett and Wilhelmson 2006).

Two types of evaluations have been carried out. First, because some studies (e.g., Gilmore et al. 2004 and Jankov et al. 2005) have shown that the choice of microphysical scheme can have a large impact on the simulated rainfall, the VGR impact associated with the changes in model microphysics was examined for the 23-24 June 2003 case, chosen because of its relatively high QPF skill. The following microphysical schemes were used for this evaluation: WRF single moment 3-class (WSM3; Hong et al. 2004), WRF single moment 5-class (WSM5; Hong et al. 2004), WRF single moment 6-class (WSM6; Hong and Lim 2006), Thompson (Thompson et al. 2006), Lin (Lin et al. 1983) and Ferrier (Rogers et al. 2001). Second, the VGR impact for the larger sample of all seven cases was studied with all runs using only the Ferrier microphysical scheme. Considering the stated orientation of the study, the Ferrier microphysics was adopted because it is currently being used operationally in the National Center for Environmental Prediction (NCEP) North American Model (NAM). The Ferrier microphysics has been used in explicit warm-season convective forecasts at 4-5 km grid spacing for the Storm Prediction Center since 2004-2005 (Ferrier 2008, personal communication). In addition, such runs have been part of NCEP's 4-5 km High Resolution Window (HRW) runs for approximately two years. In the Ferrier scheme, the total condensate is advected and not the individual species of water

(e.g., rain and cloud water as well as snow, cloud ice and graupel). There are storage arrays that retain the fraction of liquid/ice that is present and the fraction of liquid water that is in the form of rain, and from these storage arrays updated mixing ratios are calculated/diagnosed. The key assumption is that these fractions are not changed significantly due to advection, and in some situations this is probably violated. It has not been shown one way or the other that this assumption degrades forecast skill.

A quantitative and a qualitative evaluation of QPF skill was performed. The quantitative evaluations were done using the Equitable Threat Score (ETS; Schaefer 1990) and Bias, where

$$\mathrm{ETS} = \frac{\mathrm{CFA} - \mathrm{CHA}}{F + O - \mathrm{CFA} - \mathrm{CHA}}, \tag{1}$$

$$\mathrm{CHA} = O\frac{F}{V}, \tag{2}$$

and

$$\mathrm{Bias} = \frac{F}{O}. \tag{3}$$

In (1), (2) and (3), each variable indicates the number of grid points at which: (i) rainfall was correctly forecasted to exceed the specified threshold (CFA), (ii) rainfall was forecasted to exceed the threshold (F), (iii) rainfall was observed to exceed the threshold (O), and (iv) a correct forecast would occur by chance (CHA), where V is the total number of evaluated grid points. The NCEP 4 km gridded Stage IV multi-sensor data (Baldwin and Mitchell, 1997) were used for verification. It should be noted that given the study goals it is advantageous to use the ETS and Bias as they provide a simple method to score the overall QPF for a given case while

being compared to other cases. These skill indices, however, are known to penalize forecasts relatively more as the horizontal grid interval decreases due to possible small spatial or temporal shifts in rainfall forecasts (Mass et al. 2002). However, since these shifts are assumed to be random these indices are assumed adequate for the comparative needs of this study as all simulations use the same horizontal grid spacing.

3. Quantitative skill evaluations

a) Sensitivity of microphysical schemes to a refined VGR

The following provides an analysis of ETS and Bias for individual microphysical schemes and for all schemes averaged together for the 23-24 June 2003 case. Results are presented for low to moderate rainfall thresholds where the rainfall forecast is relatively skillful.

ETS values in 31L and 62L in all microphysical schemes were mostly above 0.25 for the lowest rainfall threshold and generally decreased with increasing thresholds (Fig. 3a), a result common for warm season events (e.g. Gallus and Segal 2001; Jankov and Gallus 2004). The ETS values were noticeably worse in 62L than in 31L for the lowest rainfall threshold for five microphysical schemes, possibly because of the more frequent grid cell saturation that was found (as evaluated later in this section), which lead to higher Biases (more grid points with rainfall) and higher Bias errors (Fig. 3b). In the Thompson scheme, the more frequent grid cell saturation in 62L eliminated the under-Bias, which might have improved the skill for this scheme for the 0.01" threshold (1.00" = 25.4 mm). Biases were higher in 62L than in 31L for all schemes and thresholds, and doubling the number of levels to 62 mostly improved the Bias error for the 0.10",

0.25" and 0.50" rainfall thresholds (Fig. 3b). Both the 31L and 62L runs had a low Bias for lighter rainfall thresholds and a high Bias for heavier thresholds, similar to what was found in Jankov et al. (2006) and Shaw (2004) for runs with explicit rainfall, a feature uncommon for model runs using convective parameterizations (e.g., Gallus et al. 2005).

ETS and Bias values were then averaged over all microphysical schemes and for all thresholds. Table 1 contains the average ETS and Bias values based on individual microphysical scheme ETS and Bias values (denoted as 31L_det and 62L_det in the table), as well as those values based on an averaged rainfall field from all of the different microphysical runs (akin to the ensemble mean and denoted as 31L_ens and 62L_ens in the table). These two types of averaging were done because the first one reflects the impacts on deterministic forecasts, and the second one would give an idea of the impact on an ensemble forecast. Mass et al. (2002) indicate that ensemble forecasting is becoming increasingly common, and may provide more useful forecasting information. Compared to 31L_det, ETS values in 62L_det improved for half of the rainfall thresholds, and compared to 31L_ens, 62L_ens was better in four rainfall thresholds. The higher Bias values in 31_ens versus 31_det and 62_ens versus 62_det is due to the increase in the number of grid points with forecasted rainfall as a result of averaging together the rainfall predictions from each microphysical scheme. In addition, averaging smoothes out the peak rainfall amounts, and distributes them to lower rainfall thresholds increasing the Biases for those thresholds. Ebert (2000) discusses this behavior for simple ensemble means of rainfall. The ETS and Bias values were also computed by aggregation of all microphysical schemes, but these skill values were the same compared to the average values presented in Table 1.

Contrary to expectations, individual and averaged microphysical scheme ETS values in 62L were no better than, or even worse, than those in 31L. Although microphysical and PBL

processes are parameterized, conceptually, refining the number of levels should better resolve the simulated microphysical and PBL processes in the vertical. On the other hand, doubling the number of model levels did not provide any additional refinements to the IC and LBC as these are available on only 29 levels.

For all simulations of this case, the Biases showed a systematic increase with the number of levels (Fig. 3b). Average Biases were always higher in 62L compared to 31L (Table 1) suggesting that the increase in Bias with resolution is microphysical scheme independent. There was a tendency for grid cell saturation to occur more frequently in the 62L runs compared to the 31L runs in all microphysical schemes in this case. Increasing the VGR decreases the thickness of a grid cell, potentially improving the chance that it can become saturated compared to a thicker grid cell associated with a coarser VGR (Zhang and Wang 2003), but as will be discussed later, enhanced ascent in the finer VGR runs could also lead to increased grid cell saturation.

b) Sensitivity of strongly forced convective systems to VGR

The following presents the ETS and Bias for the five strongly forced cases along with additional relevant evaluations.

1) FINE VERSUS COARSE VGR

In half of the situations (considering all cases and thresholds; Figs. 4a-e), ETS scores were higher in 21L compared to both 31L and 62L. When not considering 22-23 June 2003, however, there was an overall advantage in both 31L and 62L over 21L. When the number of levels was doubled from 31 to 62, slightly more than half of the increases in Biases (Figs 5a-e)

represented an improvement in rainfall Bias errors. When the number of levels was coarsened from 31 to 21, more than half of the increases in Biases represented an improvement in Bias errors; however, the magnitude of the increases in Biases was small compared to that of the decreases in Bias.

Contrary to expectations, the ETS values averaged over all 5 cases (Table 2), were higher in 21L than in 31L run for half of the rainfall thresholds. Also, ETS values were lower for all rainfall thresholds in 62L compared to 31L. Again, although vertical processes are better resolved with more levels, the increase in number of levels does not add any refinements to the 29 data levels available in the NARR IC and LBC. Doubling the levels to 62 also increased the Bias and overprediction of rainfall for all thresholds. Coarsening the levels from 31 to 21 decreased the Bias for all thresholds bringing values closer to 1 for three thresholds and indicating a further underprediction for the remaining three thresholds. The above results were slightly different when aggregated over all cases in the computation; however, the general conclusions were unchanged. When ETS values were computed by aggregation of all cases, the maximum difference between their computed values and the corresponding ones in Table 2 was 0.04, while the average difference over all thresholds and all runs was 0.010. The maximum difference in Bias was 1.045, while the average difference was only 0.179.

It is worth pointing out that similar to what was found previously for the different microphysical schemes, the average Biases in the present set of cases were usually higher with increased VGR (Table 2).

To explore the relationship between VGR and Biases, the sensitivity of upward vertical velocities to increasing VGR was examined. Averaging the 3D domain-peak simulated upward

vertical velocities over all hours and cases (65 evaluation periods) yielded the highest values of 36.4 m s^{-1} in the 62L run, 25.4 m s^{-1} in the 21L run and 23.8 m s^{-1} in the 31L run. The strongest average peak upward vertical velocities (Fig. 6) occurred in 65%, 20% and 15% of the 65 evaluation periods in 62L, 21L and 31L, respectively. The 3D domain-averaged upward vertical velocities averaged over all hours and cases, indicated that the 62L, 31L and 21L runs had the strongest average vertical velocities, in that order. Based on all hours and cases, in 78% and 22% of the evaluation periods (Fig. 6), 62L and 31L, respectively, had the strongest average upward motions. In none of the evaluation periods did 21L have the strongest average upward motions. Vertical cross sections of relative humidity revealed a tendency for grid cell saturation to occur more frequently as the number of levels increased. For example, Figs. 7a-c illustrate higher relative humidity in the higher VGR runs at 00 UTC 19 June 2002 just prior to convective initiation. Additionally, the number of grid boxes over the entire domain with relative humidity exceeding 70% and 90% increased with increased VGR. Profiles of area-averaged upward vertical velocities (not shown) for this and other cases just prior to convective initiation indicated stronger upward motions in the finer VGR runs occurring in concert with higher relative humidity suggesting that grid cell saturation might be occurring as a result of the stronger upward motions. With grid-cell saturation occurring more frequently, condensation and thus latent heating would be occurring more frequently potentially resulting in an increase in the buoyancy and the vertical velocities. It is also possible that as processes are better resolved in the vertical, individual systems might be stronger in some areas and acquire stronger upward vertical velocities. Although this impact would clearly be smaller than that associated with finer horizontal grid spacing, known to produce stronger upward vertical velocities (Weisman et al. 1997), the peaks in ascent should be better resolved with finer vertical grid spacing. Finally, it

should also be noted, Warner and Hsu (2000) showed in their nested runs that when using a cumulus parameterization (CP) in the outer nest and none in the inner nest, there is a relatively large sensitivity of rainfall in the inner nest to the outer nest CP. To determine if the degree of sensitivity of our runs to VGR is dependent on the choice of CP in the outer nest, tests were performed on the five strongly forced cases for 31L and 62L using the Kain-Fritsch CP (Kain and Fritsch, 1993; KF) in the outer nest instead of the BMJ CP. Although the runs using the KF CP, namely, 31L_KF and 62L_KF, performed better than both the 31L and 62L runs using the BMJ CP for all rainfall thresholds, the use of the KF CP did not result in a different degree of sensitivity to VGR (Table 2). Bias scores were lower for all thresholds in the KF CP runs compared to the BMJ CP runs, a result also found in Gallus and Segal (2001).

2) SURFACE LAYER REFINED VGR

Adding two levels to 31L near the surface (33L), mostly improved ETS values (Figs. 4a-e). Biases increased for most thresholds and cases, which generally improved the Bias errors, but only modestly (Figs. 5a-e). However, when averaged over all cases, the increases in Biases for all rainfall thresholds compared to 31L mostly indicated a further overprediction of rain (Table 2) due in large part to the influence of the 18-19 June 2002 case. Averaged over all cases, ETS values in 33L increased for most rainfall thresholds as compared to 31L.

The differences in ETS and Bias between 33L and 31L were caused by alterations in convective initiation due to changes in near surface VGR. Since the VGR changes in 31L were in the model surface layer, any convective initiation differences between the two simulations should be reflected initially by differences in surface turbulent momentum and sensible heat

fluxes (both fluxes denoted henceforth as τ and H_s, respectively, define the constant flux surface layer). Hence, relative differences in these fluxes above a given threshold (as specified in Appendix A), are used as an indicator for divergence of the simulations in the following evaluation. Simulated differences in surface fluxes were caused by the rapid collapse of the CBL due to thermal stabilization induced by evaporative cooling and the cloud shading impact on surface net thermal fluxes. Under these conditions τ and H_s become sensitive to the height of the first model level (see Appendix A for elaborations). Consequently, differences in the flow and in turn in horizontal wind convergence resulted in differences in convective initiation.

As an illustration, we present the response of the friction velocity, u_*, ($u_* = (\tau/\rho)^{0.5}$, where ρ is the near surface air density) and H_s to local convection at 21 UTC (forecast hour 3) for 22-23 June 2003 in southeastern Kansas (Fig. 8). The convection initiated an hour earlier toward the end of the spin-up time when the 31L and 33L meteorological fields were locally perturbed only somewhat by the convection. The general location of the convection is depicted by the relatively low H_s values in Fig. 8c, where the friction velocity, u_*, in 31L was less than 0.5 m s^{-1}, but increased somewhat above 1 m s^{-1} along the northern edge of the convective outflow (Fig. 8a). In the thermally unstable surface layer under clear sky conditions, u_* was around 0.8 m s^{-1}. Noticeable increases in $|\Delta u_*|$ (Δ indicates a difference between 33L and 31L) occurred in the convection area (in some locations as large as u_* itself; Fig. 8b). Following the constraints in Appendix A, it is assumed that $|\Delta u_*/u_{*31L}| \leq 0.05$ or $|\Delta H_s/H_{s31L}| \leq 0.1$ are required to avoid noticeable surface flow differences between the two runs. The shaded area in Fig. 8b indicates that $|\Delta u_*/u_{*31L}| > 0.05$ was widespread in the convection zone, whereas outside the convection zone the related values were < 0.05. The altered u_* in 33L, compared to 31L, modified surface

wind convergence and local convection forcing, a feature which is consistent with the findings in Colle and Yuter (2007). Consequently, areas of convection further differed between the two simulations due to the convection processes, and could be affected by model generated thermal circulations due to sensible heat flux gradients induced by cloud shading and soil wetness contrasts (e.g. Ookouchi et al. 1984; Segal et al. 1986).

The H_s values in 31L were about 200 W m^2 in the clear air and relatively wet surface environment to the south (Fig. 8c). The H_s values dropped to zero and even negative in the convective region indicating a stable surface layer. In the convective area $|\Delta H_s|$ was as high as 200 W m^2 (Fig. 8d), while the $|\Delta H_s|$ values in the surrounding clear sky environment were close to zero. Likewise, $|\Delta H_s / H_{s31L}| > 0.5$ was typical in the convection zone, whereas in the surrounding clear sky environment, the corresponding values were < 0.1. Similar spatial patterns in latent heat fluxes were simulated at this time (not shown). Overall, the features described above support the conclusion that in daytime clear sky conditions, the surface thermal fluxes and thus PBL thermodynamics are insensitive to the near surface changes in VGR, and likewise surface wind convergence. However, these conclusions are invalid once surface layer thermal stabilization occurs after convection initiates.

It is worth noting that during the daytime the 33L simulated 10 m height winds among the cases presented in this study were slightly weaker than those in 31L, while occasionally being slightly too weak in some areas as compared to observations.

During the nocturnal period, with a typical stable surface layer outside of convection, $|\Delta u_* / u_{*31L}| > 0.05$ and $|\Delta H_s / H_{s31L}| > 0.1$, were common, resulting in some differences in the near surface thermal stratification, which in turn enhanced the low-level jet in 33L compared to

31L (not shown). This in turn resulted in local areas of enhanced low-level horizontal wind convergence and upward vertical velocities. These differences were amplified with the initiation of convection as in the daytime.

In summary, the addition of the two levels near the surface to 31L altered the low-level wind and air temperature in a way that generally improved QPF skill in most cases presented in this study.

3) REFINED VGR ABOVE 3.5 KM (UPL) AND BELOW 3.5 KM (DNL)

(i) Skill evaluation

Values of ETS were worse in UPL and DNL compared to 31L in 30% and 47% of the presented situations, respectively (considering all cases and thresholds; Figs. 4a-e), further indicating that a refined VGR may not always result in an improved QPF forecast. Among all cases and thresholds, Biases generally increased in UPL compared to 31L (Figs. 5a-e) with an improvement in Bias errors in 73% of the presented situations. Similar trends were found in DNL with an improvement in Bias errors in 63% of the situations.

Averaged over all cases (Table 2), ETS values in UPL were better for all thresholds compared to 31L, but better only in the highest two thresholds in DNL. The ETS values in UPL and DNL were better than those in 62L for all thresholds, a rather intriguing result that is evaluated rigorously in sub-section (ii) below. As was also found previously for VGR refinements, Biases were mostly higher for the UPL and DNL VGR refinements as compared to 31L. Bias errors were worsened in DNL but improved in UPL.

(ii) Factor separation analysis

Additional insight into the results in sub-section *(i)* can be provided by applying the factor separation methodology formulated by Stein and Alpert (1993). Based on this methodology:

$$\underbrace{S_{62L} - S_{31L}}_{d} = \underbrace{(S_{UPL} - S_{31L})}_{du} + \underbrace{(S_{DNL} - S_{31L})}_{dd} + \underbrace{S^{Y}}_{sy} \qquad (4)$$

where S_{31L} and S_{62L} denote, respectively, the 31L (control run) and 62L run QPF skill (note that following the definitions in section 2b the 62L VGR consists of the composite of UPL and DNL), while S_{UPL} and S_{DNL} denote, respectively, the QPF skill in the UPL and DNL runs. The VGRs associated with S_{UPL} and S_{DNL} are the factors. S^{Y} denotes the synergistic term [$S^{Y} = S_{62L} - (S_{UPL} + S_{DNL}) + S_{31L}$]. Note that for the sake of brevity, the various terms in Eq. 4 are denoted as *d*, *du*, *dd* and *sy*. Equation (4) expresses the difference in skill between 62L and the control run (31L) as the sum of the differences in skill between UPL and 31L, DNL and 31L and the synergistic term. The synergistic term reflects the skill associated with the non-linear interaction due to a simultaneous change in the upper and lower VGR. This term may be thought of as the difference between the actual skill occurring in the run in which both the upper and the lower VGR resolutions have been changed simultaneously and the skill expected by adding the impacts of each individual change. Appendix B provides mathematical-physical insight into the derivation and meaning of the various terms in Eq. 4.

Figs. 9a-e present the various terms of the factor separation analysis for ETS using (4) as computed for the situations depicted in Figs. 4a-e. Most of the presented situations (70%) had negative synergy (*sy* < 0) suggesting that PBL and warm cloud processes interacted with microphysical processes above the melting level (~ 3.5 km) to degrade the ETS of 62L, while 27% of the situations had positive synergy (*sy* > 0) suggesting that these interactions improved the ETS of 62L. The remaining 3% of the situations had no synergy (*sy* = 0) implying that non-linear interactions between the PBL/warm cloud processes and microphysical processes above the melting level had no effect on ETS.

Averaging the various terms in Eq. 4 over all cases with positive synergy (*sy* > 0; Table 3) the positive contribution of the non-linear interactions (the synergy) between warm cloud processes and microphysical processes above the melting level on the QPF skill of 62L was particularly noticeable for the 0.5" and 0.75" rainfall thresholds. For these thresholds, refining the VGR from 31L to 62L, which consists of compositing the VGRs of UPL and DNL, provided better skill than refining the VGRs to either UPL or DNL. For example, for the 0.75" rainfall threshold, *d*(= 0.02) is greater than the sum of *du*(= -0.003) and *dd*(= 0.015) due to the positive contribution of *sy*(=0.015). The negative contribution of synergy (*sy* < 0) on 62L was largest for the 0.01" threshold as the synergy was the most negative. For this threshold, *d*(= -0.000) is lower than the sum of *du*(=0.026) and *dd*(=0.019) due to the negative synergy (*sy* = -0.045). Note from the table that the terms on the RHS of Eq. 4 (*du, dd and sy*) very rarely acquire the same sign, thus resulting in a moderation of the magnitude of *d.*

c) Sensitivity of weakly forced cases to a refined VGR

Averaged over the two weakly forced cases (Table 2), ETS values for 62L_WK (WK: weakly forced) worsened compared with 31L_WK for the lowest thresholds, and Bias errors worsened (rain was further overpredicted) for those same thresholds. This can be attributed to the increase in Biases and Bias errors and the decrease in ETS found only in 20-21 June 2005. ETS values improved and Bias values improved (decreased) for all the thresholds in 24-25 July 2005. In both of these cases, the 3D domain-hourly-averaged upward vertical velocities were higher in the finer VGR run suggesting the higher vertical velocities may have played a role in more frequent grid cell saturation in 20-21 June 2005 and the higher Biases, but other processes might have been more important in 24-25 July 2005 because in this case the Biases were lower in the refined VGR.

An improved QPF skill over 31L and even 62L occurred in some instances when two levels near the surface were added (33L_WK). Table 2 shows an improvement in ETS in three thresholds in 33L_WK compared to 31L_WK and three thresholds compared to 62L_WK. Bias errors increased and were worse for all thresholds in 33L_WK compared to 31L_WK.

As indicated by the results, the simulated rainfall in the weakly forced cases was improved somewhat with refinements in the VGR. The results also suggest that better resolved surface turbulent thermal flux processes were at least as important as better resolved microphysical processes.

4. Qualitative evaluations

Modifying the VGR as described in the previous section generally resulted in local shifts in rainfall patterns. Overall, rainfall amounts between runs with various VGR differed by 25

mm in some cases to as much as 180 mm on 18-19 June 2002. On 22-23 June 2003 there was a sharp improvement in the rainfall forecast associated with the coarsening of VGR, a result which is counterintuitive. The rainfall features from those two specific cases are evaluated next.

a) 18-19 June 2002 case

One of the cases more sensitive to vertical resolution was 18-19 June 2002. Observed rainfall (Fig. 10a) occurred mainly from eastern Iowa northward into eastern Minnesota and western Wisconsin with 18 hour accumulated rainfall amounts between 0.3 and 25 mm. The 21L run (Fig. 10b) sharply underpredicted the band of rain in Minnesota and Iowa and overpredicted rain in eastern South Dakota and Nebraska. The 31L run (Fig. 10c) forecast was better than the 21L run in eastern Iowa and Minnesota, but the rainfall in the western part of the domain (as high as 180 mm) was greatly overpredicted. Perhaps the convective forcing in eastern Iowa was not captured well in the coarse 21L run, but was in the 31L run because of the additional information from the IC and LBC.

To test the sensitivity of WRF simulations to the resolution of the IC and LBC, two additional runs were performed using 21 and 31 model levels, but using 20 NARR levels instead of 29 levels for the IC and LBC. The 20 NARR levels correspond to data in increments of 50 hPa from 1000 hPa to 100 hPa. The sensitivity to IC and LBC resolution was examined by comparing the changes in ETS among the two 31L runs (31L using 29 NARR levels and 31L using 20 NARR levels) to those in the 21L runs (21L using 29 NARR levels and 21L using 20 NARR levels). Averaged over the five strongly forced cases, the sensitivity (change in ETS) was greatest among the 31L runs suggesting the resolution of IC and LBC data can have a substantial impact on rainfall forecasts; however, for the case being discussed in this section, the

largest changes in ETS were among the 21L runs implying that for this specific case, the resolution of the IC and LBC data itself was not as important as other factors including: placement of model levels and thus the degree of interpolation from the NARR levels to the model levels, and also the extent to which vertical processes are more poorly resolved in the coarser VGR.

As the VGR was refined even further (from 31 to 62 levels) the rainfall forecast worsened in most areas (indicated by lower ETS values for each threshold in Fig. 4a) except in northeastern Iowa (Fig. 10d) where the coverage and intensity was closer to what was observed.

The following is suggested concerning the skill of 62L : (i) the increase in the number of levels beyond 31 resulted in an increase in Biases (Fig. 5a) for the lightest thresholds due to more frequent grid cell saturation in these finer VGR runs, and (ii) the non-linear interaction between the atmospheric processes below and above the melting level further worsened the rainfall forecasts for 62L (note from Fig. 4a, the ETS values in UPL and DNL were higher than those of 62L, whereas the synergy for this case was negative).

b) 22-23 June 2003 case

The coarser VGR run (21L) proved to be better than the 31L run on 22-23 June 2003. Observed 18 hour accumulated rainfall approached 50 mm (Fig. 11a) in northeastern Kansas, similar to what was simulated in 21L (Fig. 11b), and at least twice the amount simulated in 31L (Fig. 11c). The system in southern Kansas that produced as much as 127 mm of rainfall in the 31L run was not observed or simulated in 21L.

To understand the processes associated with the rainfall differences between the 21L and 31L runs, a relevant analysis of the kinematic and thermodynamic environment is presented. The intense rainfall that was simulated in 31L in southern Kansas could have been due to a stronger near-surface thermal gradient and stronger low-level wind convergence in 31L near the rainfall area (Fig. 12a-d). Figures 12a and 12c illustrate the 2 m temperature from the 21L and 31L runs, respectively, and show a stronger thermal gradient in the 31L run at 22 UTC (4-h) 23 June 2003 (Fig. 12c) shortly before convection initiated in this area. Near-surface horizontal wind convergence was more expansive and also stronger in the 31L run near the thermal gradient (see Figs. 12b and 12d). The system in southern Kansas in the 31L run persisted throughout most of the model integration and could have blocked the transport of moisture into northern Kansas. This was suggested by lower area-averaged (~ 100 km x 300 km area) precipitable water in the 31L run (30 mm) compared to that in the 21L run (39 mm) north of the system in southern Kansas (not shown). Consequently, in the area where the heaviest rainfall actually occurred in northeastern and northern Kansas, the pre-storm environment was much more unstable in 21L as the most unstable convective available potential energy (MUCAPE), averaged over the same area as above, and was higher by nearly 2000 J kg^{-1}.

5. Summary and conclusions

A refined vertical grid resolution should conceptually improve the prediction of convection-related, microphysical and boundary layer processes, which in turn should improve rainfall forecasts. This paper provides an exploratory evaluation of summertime convection sensitivity in the Midwest to various refinements in the vertical grid resolution, based on 68

simulations, using the NARR for initial and lateral boundary conditions in convection-permitting runs with the WRF ARW model.

Doubling the number of levels from 31 in the control run (31L) to 62 did not result in a consistent improvement in QPF forecasts, as ETS values averaged over various microphysical schemes in an illustrative case worsened for half of the rainfall thresholds with an increased overprediction of rainfall. Averaged over five representative cases of summer convection associated with strong forcing, ETS values declined for all rainfall thresholds while the overprediction of rainfall increased. Similarly, ETS values were mostly lower in DNL compared to 31L, and Biases were higher indicating a further overprediction of rainfall. There was, however, an improvement in rainfall forecasts in UPL as ETS values, when averaged over the five cases, increased for all thresholds and Biases generally were improved suggesting that although microphysical processes are still parameterized, increasing the VGR above the melting level may result in better resolved processes. Application of the factor separation method suggested, however, that 62L, which is the composite of the DNL and UPL VGRs, had mostly a negative impact on the ETS through boundary layer and warm cloud processes interacting with microphysical processes above the melting level.

A general improvement in rainfall forecasts occurred when two levels were added to the surface layer as ETS values increased for most rainfall thresholds in 33L, although the overprediction of rainfall was further increased for most thresholds. In general, there was a systematic increase in Bias with an increase in the VGR, which is suggested to be related to grid cell saturation occurring more frequently in the finer VGR runs. Enhanced upward motions occurring in concert with higher relative humidity prior to convective initiation in the finer VGR

runs suggest that these enhanced upward motions might have led to more frequent grid cell saturation.

Qualitatively, varying the vertical grid resolution resulted in noticeable 18 hour accumulated rainfall differences (> 25 mm) over widespread areas among different microphysical schemes and different cases. While most of the rainfall differences were due to local shifts in rainfall centers, in some areas rainfall was completely removed or new rainfall areas were created.

In conclusion, QPF skill can be sensitive to the vertical resolution, and at least on a case by case basis, the skill might not be improved much by refining the number of levels, especially if the IC and LBC are on a relatively coarse vertical grid. In the present study, the IC and LBC were from the NARR, which provides data on 29 levels, and although increasing the number of model levels from 31 to 62 should conceptually better resolve the simulated processes in the vertical, it did not provide any additional refinement to the IC and LBC. Also, as in the case of horizontal grid resolution, the effect of a refined VGR on forecasted rainfall would be modulated significantly by errors in the IC and LBC and the incompleteness of model physical formulations (Tribbia and Baumhefner 1988). Future work could focus on a detailed evaluation of specific cloud microphysical or boundary layer processes affected by modifications of vertical grid resolution. Carrying out sensitivity simulations over an entire season using a refined vertical grid resolution would provide further insight into the QPF evaluations presented in this illustrative study.

Acknowledgments

The authors would like to thank Jimmy Correia and three anonymous reviewers for their comments on the paper. This research was funded by NSF Grants ATM-0226059 and ATM-0537043. One of the authors (M.S) was also partially supported by the Iowa Agriculture and Home Economics Experiment Station Project 4503.

Appendix A

The Cause of Surface Turbulent Momentum and Sensible Heat Flux Differences Between 31L and 33L During Convective Initiation

Analogous to the thermal stabilization near the surface following sunset, during daytime convective initiation heavy cloud shading and wet surfaces due to rainfall may reduce the surface sensible heat fluxes considerably, or reversing its direction while resulting in the onset of a stable surface layer (e.g. Rosenberg et al. 1983, Markowski et al. 1998). Additionally, stabilization of the lower atmosphere and the rapid collapse of the CBL associated with evaporative cooling are typical in convective situations (see e.g. Kallos and Segal 1991 for illustrative observed temperature profiles). The PBL then might become stable from the surface upward, or transformed into a relatively shallow, near neutral stratification layer capped by a temperature inversion. The above features were simulated in the present study in various areas where convection was initiated. Differences in τ and H_s between 31L and 33L, following the elaboration below, were related to different height specifications of the lowest model level in both runs (54 m in 31L and 10 m in 33L).

Since the surface fluxes are computed using surface layer similarity theory formulation, the first model level should be within the surface layer. The surface layer depth, in which τ and H_s may decrease with height at most by ~ 0.1 (or by ~ 0.05 for u_*), is roughly estimated to be ~ 0.1 of the PBL depth (e.g. Panofsky and Dutton 1982). Denoting the differences between 33L and 31L in u_* and H_s as Δu_* and ΔH_s, respectively, whereas their corresponding relative differences compared with 31L are denoted as $\Delta u_*/u_{*31L}$ and $\Delta H_s/H_{s31L}$, then following the

constraints stated above, once $|\Delta u_* / u_{*31L}| > 0.05$ or $|\Delta H_s / H_{s31L}| > 0.1$, at least some differences in surface flow between 31L and 33L should emerge.

During the daytime in an unstable and clear-sky environment the PBL depth is typically 1000-2000 m; thus, the surface layer depth, as defined previously, is likely to be deeper than the lowest model level prescribed in 31L and 33L. In contrast, the stable PBL depth is at most a few hundreds of meters. Hence, for stable surface layer locations, or where the CBL had collapsed due to convective initiation, the 54 m level in 31L is likely located above the surface layer, whereas in 33L, the 10 m level is likely within the surface layer. In a second aspect, the rapid local changes near the surface in wind or temperature during convective initiation events result in an inadequate model representation of the surface layer processes, since the surface layer parameterization used in the model was derived for reasonably horizontally uniform and steady flows. However, the adjustment of the surface layer in such events is faster in the 33L case since it progresses from the surface upward, and thus reaches the 10 m level first. Hence, considering the two aspects above, u_* and H_s computed using the similarity theory formulation under convective initiation in 33L are likely to differ from these in 31L, while being more accurate.

We carried out sensitivity simulations, including various prescribed VGRs in the lowest 100 m, shutting off cloud-solar radiation interaction (i.e. clouds are transparent to solar radiation), and shutting off solar radiation. These simulations generally further supported the conclusion that the height of the first model level is important for resolving surface flow under a convective initiation environment.

Appendix B

Derivation of the Factor Separation Equation: The DNL and UPL Case

In order to provide further insight into Eq. (4), it is derived in the following using a somewhat different approach to that formulated in Stein and Alpert (1993). A model QPF skill index, *S*, is assumed with values within the segment [0,1] (in the present study *S* is the ETS). Also a continuum of VGR variations from that of the control simulation (31L) is introduced by using a generalized VGR configuration (GVC) of DNL and UPL. The GVC of DNL and UPL is defined by placing the additional levels compared to those in 31L at $Z_{kd}+(Z_{kd+1} - Z_{kd})\cdot v_d$ in the DNL analog VGR, where $0 \le v_d \le 1$ and at $Z_{ku}+(Z_{ku+1} - Z_{ku})\cdot v_u$ in the UPL analog VGR, where $0 \le v_u \le 1$, and Z_{kd} (or Z_{ku}) and Z_{kd+1} (or Z_{ku+1}) are two adjacent levels in the control simulation 31L. The two GVCs defined above are the factors represented mathematically by v_d and v_u. The composite of the GVCs of DNL and UPL, yields the GVC of 62L with the corresponding QPF skill index $S(v_d,v_u)$. The control simulation VGR is obtained by setting $v_d = 0$ or $v_u = 0$ in the corresponding GVCs. The specific VGR configurations of DNL, UPL and 62L used in the present study simulations are obtained by setting, respectively, $v_d = 0.5$, $v_u = 0.5$, and $v_u = v_d = 0.5$ in their corresponding GVCs.

The Taylor series expansion of $S(v_d,v_u)$ around $v_d = v_u = 0$ yields:

$$S(\Delta v_d, \Delta v_u) - S(0,0) = \frac{\partial S}{\partial v_d}\cdot \Delta v_d + \frac{\partial S}{\partial v_u}\cdot \Delta v_u + \frac{1}{2!}\left[\frac{\partial^2 S}{\partial^2 v_d}\cdot (\Delta v_d)^2 + \frac{\partial^2 S}{\partial^2 v_u}\cdot (\Delta v_u)^2\right] + \frac{\partial^2 S}{\partial v_d \partial v_u}\cdot \Delta u_d \Delta v_u + \ldots \quad , \tag{B1}$$

where the derivatives indicate their acquired values at $v_d = v_u = 0$.

Using a numerical difference approximation for the various derivatives in (B1) (see Fig B1 for illustration) based on *S* values obtained in the four simulations described in sub-section 3b(3) item (*ii*), yields:

$$S(\Delta v_d, \Delta v_u) - S(0,0) = S_{62L} - S_{31L}, \tag{B2}$$

$$\frac{\partial S}{\partial v_d} \cdot \Delta v_d = \frac{S(\Delta v_d, 0) - S(0,0)}{\Delta v_d} \cdot \Delta v_d = S_{DNL} - S_{31L}, \tag{B3}$$

$$\frac{\partial S}{\partial v_u} \cdot \Delta v_u = \frac{S(0, \Delta v_u) - S(0,0)}{\Delta v_u} \cdot \Delta v_u = S_{UPL} - S_{31L}, \tag{B4}$$

and

$$\frac{\partial^2 S}{\partial v_d \partial v_u} \Delta v_d \cdot \Delta v_u = \frac{(S(\Delta v_d, \Delta v_u) - S(0, \Delta v_u)) \frac{1}{\Delta v_d} - (S(\Delta v_d, 0) - S(0,0)) \frac{1}{\Delta v_d}}{\Delta v_u} \cdot \Delta v_d \cdot \Delta v_u =$$

$$= S_{62L} - S_{UPL} - S_{DNL} + S_{31L}, \tag{B5}$$

where $\Delta v_d = \Delta v_u = 0.5$.

In approximating (B1) using *S* values of only four simulations [the minimum needed to approximate (B1)] the additional higher order derivatives are zero. Hence using (B1)-(B5) yields the factor separation Eq. (4) with the linear contribution of the two factors given by (B3) and (B4). The synergy term (reflecting the non-linear interaction between the two varying factors) which is given by (B5), is represented by the second order mixed derivative of *S* in (B1). It is worth noting that equivalent to the derivation above, applying Taylor's theorem of the mean yields the same results. Finally, using the methodology described in this appendix, a factor separation equation can be derived also when the number of factors is larger than two.

References

Aligo, E.A., W.A. Gallus, Jr., and M. Segal, 2007: Summer rainfall forecast spread in an ensemble initialized with different soil moisture analyses. *Wea. Forecasting*, **22,** 299-314.

Baldwin, M. E., and K. E. Mitchell, 1997: The NCEP hourly multi-sensor U.S. precipitation analysis for operations and GCIP research. Prepints, *13th AMS Conference on Hydrology*, Long Beach, CA, 54-55.

Betts, A.K., 1986: A new convective adjustment scheme. Part I: Observational and theoretical basis. *Quart. J. Roy. Meteor. Soc.*, **112,** 677-692.

____, and M.J. Miller, 1986: A new convective adjustment scheme. Part II: Single column tests using GATE wave, BOMEX, ATEX and arctic air-mass data sets. *Quart. J. Roy. Meteor. Soc.*, **112,** 693-709.

Bryan, G. H., J. C. Wyngaard and J. M. Fritsch, 2003: Resolution requirements for the simulation of deep moist convection. *Mon. Wea. Rev.*, **131,** 2394-2416.

Colle, B. A. and S. E. Yuter, 2007: The impact of coastal boundaries and small hills on the precipitation distribution across southern Connecticut and Long Island, New York. *Mon. Wea. Rev.*, **135**, 933-954.

Davis, C., and Coauthors, 2004: The bow echo and MCV experiment: observations and opportunities. *Bull. Amer. Meteor. Soc.*, **85,** 1075-1093.

Ebert, E. E., 2001: Ability of a poor man's ensemble to predict the probability and distribution of precipitation. *Mon. Wea. Rev.,* **129,** 2461-2480.

Ek, M. B., K.E. Mitchell, Y. Lin, E. Rogers, P. Grunmann, V. Koren, G. Gayno, and J.D. Tarplay, 2003: Implementation of Noah land surface model advances in the National Centers for Environmental Prediction operational mesoscale Eta model. *J. Geophys. Res.*, **108,** 8851, doi:10.1029/2002JD003296.

Gallus, W. A. Jr. and M. Segal, 2001: Impact of improved initialization of mesoscale features on convective system rainfall in 10-km Eta simulations. *Wea. Forecasting*., **16,** 680-696.

_____, W. A. Jr., J. Correia Jr. and I. Jankov, 2005: The 4 June 1999 derecho event: A particularly difficult challenge for numerical weather prediction. *Wea. Forecasting.*, **20**, 705-728.

Gilmore, M. S., J. M. Straka and E. N. Rasmussen, 2004: Precipitation and evolution sensitivity in simulated deep convective storms: Comparisons between liquid-only and simple ice and liquid phase microphysics, *Mon. Wea. Rev*., **132,** 1897-1916.

Grams, J. S., W. A. Gallus, Jr. S. E. Koch, L. S. Wharton, A. Loughe and E. E. Ebert, 2006: The use of a modified Ebert-McBride Technique to evaluate mesoscale model QPF as a function of convective system morphology during IHOP 2002. *Wea. Forecasting*, **21,** 288-306.

Hong, S. –H., J. Dudhia and S. –H. Chen, 2004: A revised approach to ice microphysical processes for the bulk parameterization of clouds and precipitation. *Mon. Wea.Rev.*, **132,** 103-120.

_____ and J. –O. Lim, 2006: The WRF single-moment 6-class microphysics scheme (WSM6). *Journal of the Korean Meteorological Society*, **42,** 129-151

Janjic, Z.I., 1994: The step-mountain Eta coordinate model: Further developments of the convection closure schemes. *Mon. Wea. Rev.*, **122,** 927-945.

_____, 2002: Nonsingular implantation of the Mellor-Yamada level 2.5 scheme in the NCEP meso model. NOAA/NWS/NCEP Office Note #437, 61 pp.

Jankov, I. and W. A. Gallus Jr., 2004: MCS rainfall forecast accuracy as a function of large-scale forcing. *Wea. Forecasting.*, **19**, 428-439.

_____, W.A. Gallus Jr., M. Segal, B. Shaw and S. E. Koch, 2005: The impact of different WRF model physical parameterizations and their interactions on warm season MCS rainfall. *Wea. Forecasting.*, **20**, 1048-1060.

_____, _____, _____ and S. E. Koch, 2007: Influence of initial conditions on the WRF-ARW model QPF response to physical parameterization changes. *Wea. Forecasting.*, **22,** 501-519.

Jewett, B. F. and R. B. Wilhelmson, 2006: The role of forcing in cell morphology and evolution within midlatitude squall lines. *Mon Wea. Rev.*, **134,** 3714-3734.

Kain J. S. and J. M. Fritsch, 1993: The role of convective "trigger function" in numerical forecasts of mesoscale convective systems. *Meteor. Atmos. Phys.*, **49,** 93-106.

_____ and _____, 1998: Multiscale convective overturning in mesoscale convective systems: Reconciling observations, simulations, and theory. *Mon Wea. Rev.*, **126,** 2254-2273.

Kallos, G. and M. Segal, 1991: On the meteorological conditions during postprecipitation periods: Implications to pollutant dispersion. *J. Appl. Meteor.,* **30,** 297-311.

Kimball, S. K. and F. C. Dougherty, 2006: The sensitivity of idealized hurricane structure and development to the distribution of vertical levels in MM5. *Mon Wea. Rev*., **134,** 1987-2008.

Lin, Y. –L., R. D. Farley and H. D. Orville, 1983: Bulk parameterization of the snow field in a cloud model. *J. Appl. Meteor.,* **22,** 1065-1092.

Lindzen, R. S. and M. Fox-Rabinovitz, 1989: Consistent Vertical and Horizontal Resolution. *Mon. Wea. Rev*., **117,** 2575-2583.

Markowski, P. M., E. N. Rasmussen, J. M. Straka and D. C. Dowell, 1998: Observations of low-level baroclinicity generated by anvil shadows. *Mon Wea. Rev*., **126,** 2942-2958.

Mass, C.F., D. Ovens, K. Westrick, and B.A. Colle, 2002: Does increasing horizontal resolution produce better forecasts? The results of two years of real-time numerical weather prediction over the Pacific Northwest. *Bull.Amer.Meteor*. Soc., **82,** 407-430.

McCumber, M., W-K. Tao, J. Simpson, R. Penc ands-T Soong, 1991: Comparison of ice-phase microphysical parameterization schemes using numerical simulations of tropical convection. *J. Appl. Meteor.,* **30,** 985-1004.

Molinari, J. and M. Dudek, 1992: Parameterization of convective precipitation in mesoscale numerical models: A critical review. *Mon Wea. Rev*., **120,** 326-344.

Ookouchi, Y., M. Segal, R. C. Kessler and R. A. Pielke, 1984: Evaluation of soil moisture effects on the generation and modification of mesoscale circulations. *Mon Wea. Rev*., **112,** 2281-2292.

Panofsky, H. A. and J. A. Dutton, 1984: *Atmospheric Turbulence.* John Wiley & Sons, Inc., 397.

Pecnick, M. J., and D. Keyser, 1989: The effect of spatial resolution on the simulation of upper-tropospheric frontogenesis using a sigma-coordinate primitive equation model. *Meteor. Atmos. Phys.*, **40,** 137-149.

Roebber, P. J. and J. Eise, 2001: The 21 June 1997 flood: Storm-scale simulations and implications for operational forecasting. *Wea. Forecasting*, **16,** 197-218.

_____, P.J., D.M. Schultz, B.A. Colle, and D.J. Stensrud, 2004: The risks and rewards of high-resolution and ensemble numerical weather prediction. *Wea. Forecasting*, **19,** 936-949.

Rogers, E., T. Black, B. Ferrier, Y. Lin, D. Parrish and G. DiMego, 2001: Changes to the NCEP Meso Eta analysis and forecast system: Increase in resolution, new cloud microphysics, modified precipitation assimilation, modified 3DVAR analysis. NWS Technical Procedures Bulletin 488, NOAA/NWS [Available online at http://www.emc.ncep.noaa.gov/mmb/mmbpll/eta12tpb/].

Rosenberg, N. J., B. L. Blad and S. B. Verma, 1983: *Microclimate*, John Wiley & Sons, Inc., 495.

Schaefer, J.T., 1990: The critical success index as an indicator of warning skill. *Wea. Forecasting*, **5,** 570-575.

Segal, M., J. F. W. Purdom, J. L. Song, R. A. Pielke and Y. Mahrer, 1986: Evaluation of cloud shading effects on the generation and modification of mesoscale circulations. *Mon Wea. Rev*., **114,** 1201-1212.

Shaw, B. L., 2004: An objective inter-comparison of WRF,MM5, and NCEP ETA shortrange quantitative precipitation forecasts for the International H_2O Project (IHOP) domain. *Extended Abstract, 5th WRF/14th MM5 Users' Workshop,* Boulder, CO, National Center for Atmospheric Research, 3.6. [Available online at http://www.mmm.ucar.edu/mm5/workshop/workshop-papers_ws04.html].

Skamarock, W.C., J.B. Klemp, J. Dudhia, D.O. Gill, D.M. Barker, W. Wang, and J.G. Powers, 2005: A description of the advanced research WRF version 2. NCAR Tech. Note NCAR/TN-468+STR, 88 pp. [Available online at http://www.wrf-model.org/wrfadmin/docs/arw_v2.pdf]

Stein U. and P. Alpert, 1993: Factor separation in numerical simulations. *J. Atmos. Sci.*, **50,** 2107-2115.

Thompson, G., P. R. Field, W. D. Hall and R. M. Rasmussen, 2006: A new bulk microphysical parameterization for WRF (&MM5). Preprints, *7th WRF Users' Workshop,* Boulder, CO, National Center for Atmospheric Research, 1-11.

Tribbia, J. J. and D. P. Baumhefner, 1988: The reliability of improvements in deterministic short-range forecasts in the presence of initial state and modeling deficiencies. *Mon. Wea. Rev*., **116,** 2276-2288.

Warner, T. T. and H-M Hsu, 2000: Nested-model simulation of moist convection: The impact of coarse-grid parameterized convection on fine-grid resolved convection. *Mon. Wea. Rev*., **128,** 2211-2231.

Wei, H., M. Segal, W. J. Gutowksi Jr., Z. Pan, R. W. Arritt and W. A. Gallus Jr., 2001: Sensitivity of simulated regional surface thermal fluxes during warm advection snowmelt to selection of the lowest model level height. *J. Hydrometeor*., **2,** 395-405.

Weismann, M. L., C. Davis and J. Done, 2004: The promise and challenge of explicit convective forecasting with the WRF model. Preprints, *22nd Conference on Severe Local Storms*, Hyannis, MA, American Meteorological Society, 17-2.

Zhang, D.-L., and X. Wang, 2003: Dependence of hurricane intensity and structure on vertical resolution and time-step size. *Advances in Atmospheric Sciences*, **20,** 711-725.

List of Figures

Figure 6. Percentage of evaluation periods (all hours and cases) with the highest 3D domain-peak upward vertical velocities (labeled peak) and with the highest 3D domain-averaged upward vertical velocities (labeled average). The values of the upward vertical velocities (m s^{-1}) are indicated above the bars.

Figure 7. West-east vertical cross-section of relative humidity (as depicted by the line segment in Fig. 10b) at 00 UTC 19 June 2002 prior to convective initiation in the (a) 21L, (b) 31L and (c) 62L runs. The contour interval is 10% with values above 70% shaded. The height is above mean sea level.

Figure. 8. The 21 UTC 22 June 2003 (a) 31L surface friction velocity, u_*, (m s^{-1}), (b) Δu_* (contoured) and $\Delta u_* / u_{*31L}$ (shaded), (c) 31L surface sensible heat fluxes, H_s ,(W m^{-2}), and (d) surface ΔH_s (contoured) and $\Delta H_s / H_{s31L}$ (shaded) (see text for the notation). The area presented is indicated by the dashed box in Fig. 11c. The contour interval in (a) is 0.2 m s^{-1} and the contour levels in (c) are 0, ±50, 100, 200 and 300 W m^{-2}. The contour and shading levels in (b) are ±0.05, ±0.10, ±0.25 and ±0.5 (in m s^{-1} when contoured). The contour levels in (d) are ±50, ±100 and ±200 W m^{-2}, while the shading levels are ±0.05, ±0.10, ±0.25 and ±0.5.

Figure 9. The values for the various terms in the factor separation analysis of ETS using Eq. 4 (identified by the gray coding in the inset) for the indicated rainfall thresholds for (a) 18-19 June 2002, (b) 20-23 June 2003, (c) 22-23 June 2003 and (d) 23-24 June 2003. ETS_{FS} represents the values of *sy*, *d*, *du* and *d*.

Figure 10. The 18 hour accumulated rainfall (mm) ending at 12 UTC 19 June 2002 from (a) observations, (b) the 21L run, (c) the 31L run and (d) the 62L run. The location of the west-east vertical cross section in (b) is presented in Fig. 7.

Figure 11. The 18 hour accumulated rainfall (mm) ending at 12 UTC 23 June 2003 from (a) observations, (b) the 21L run and (c) the 31L run. The area outlined by the solid box in (a) will be considered in Fig. 12. The area outlined by the dashed box in (c) was considered in Fig. 8.

Figure 12. The 22 UTC 22 June 2003 (a) 2 m temperature (K), (b) near-surface horizontal wind divergence (10^{-4} s^{-1}) in the 21L run, (c) the 2 m temperature and (d) near-surface horizontal wind divergence in the 31L run. This area is indicated by the solid box in Fig. 11a. In (b) and (d) the divergence is represented by solid contours while convergence is represented by dashed contours with shading. The interval of contours and shading is $3 \cdot 10^{-4}$ s^{-1}.

Figure B1. Schematic illustration related to the analytic and the finite difference approximation of Eq. B1 used for the factor separation analysis of DNL and UPL. The values of the analytic skill index, $S(v_d,v_u)$, and these based on the simulations (in brackets), are indicated.

List of Tables

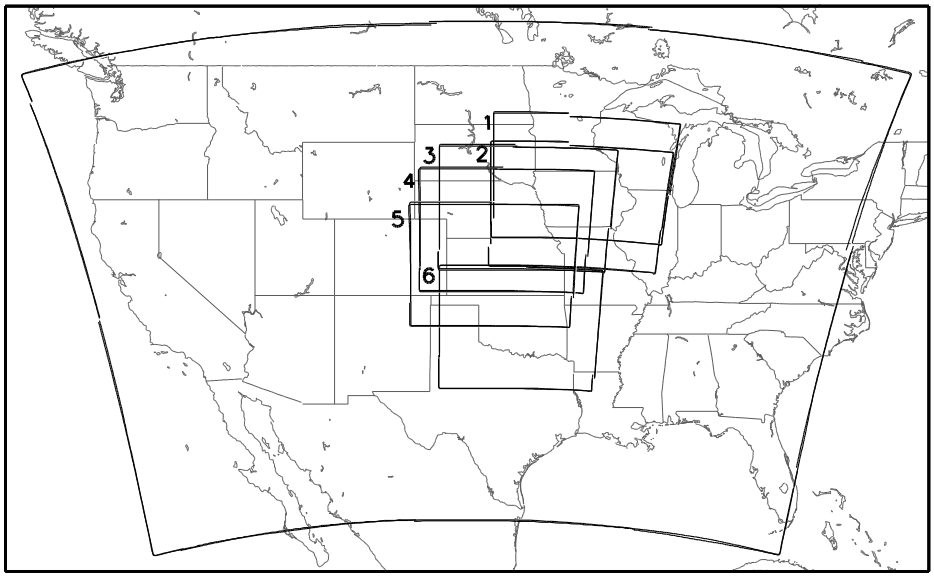

Figure 1. Illustration of the simulated inner 4 km nests and the outer 12 km nest for each of the cases studied (strongly forced cases: #1- 18-19 June 2002; #3- 23-24 June 2003; #4- 22-23 June 2003; #5- 28-29 June 2003; #6- 20-21 June 2003, weakly forced cases: #2- 20-21 June 2005 and 24-25 July 2005).

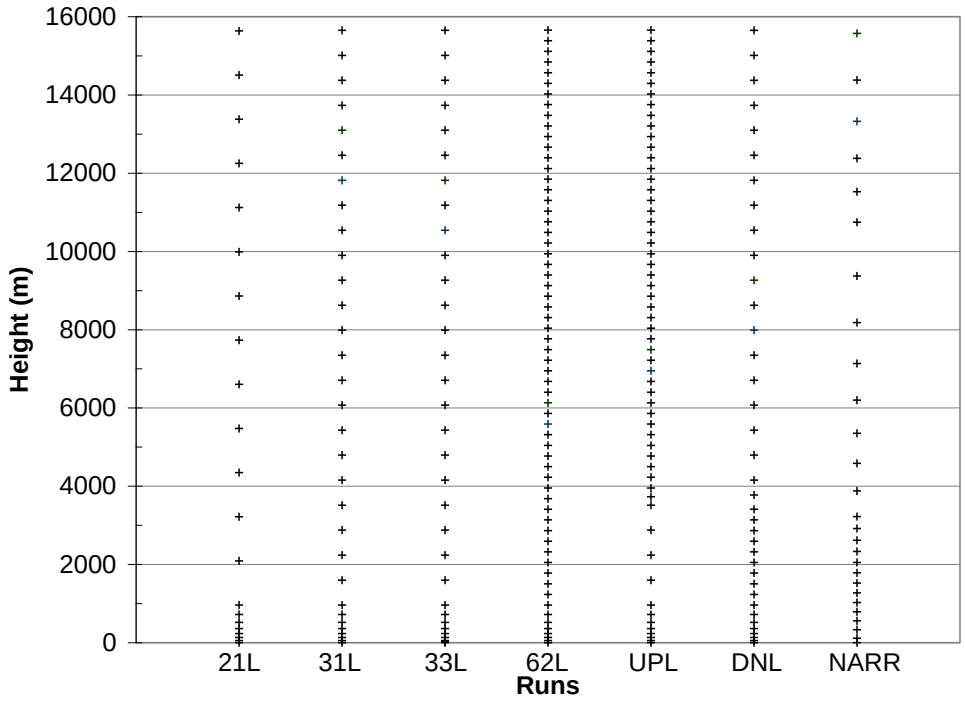

Figure 2. The heights of the model levels above the surface for each of the indicated runs and above sea level for the NARR. The heights of the NARR levels were computed assuming a standard atmosphere.

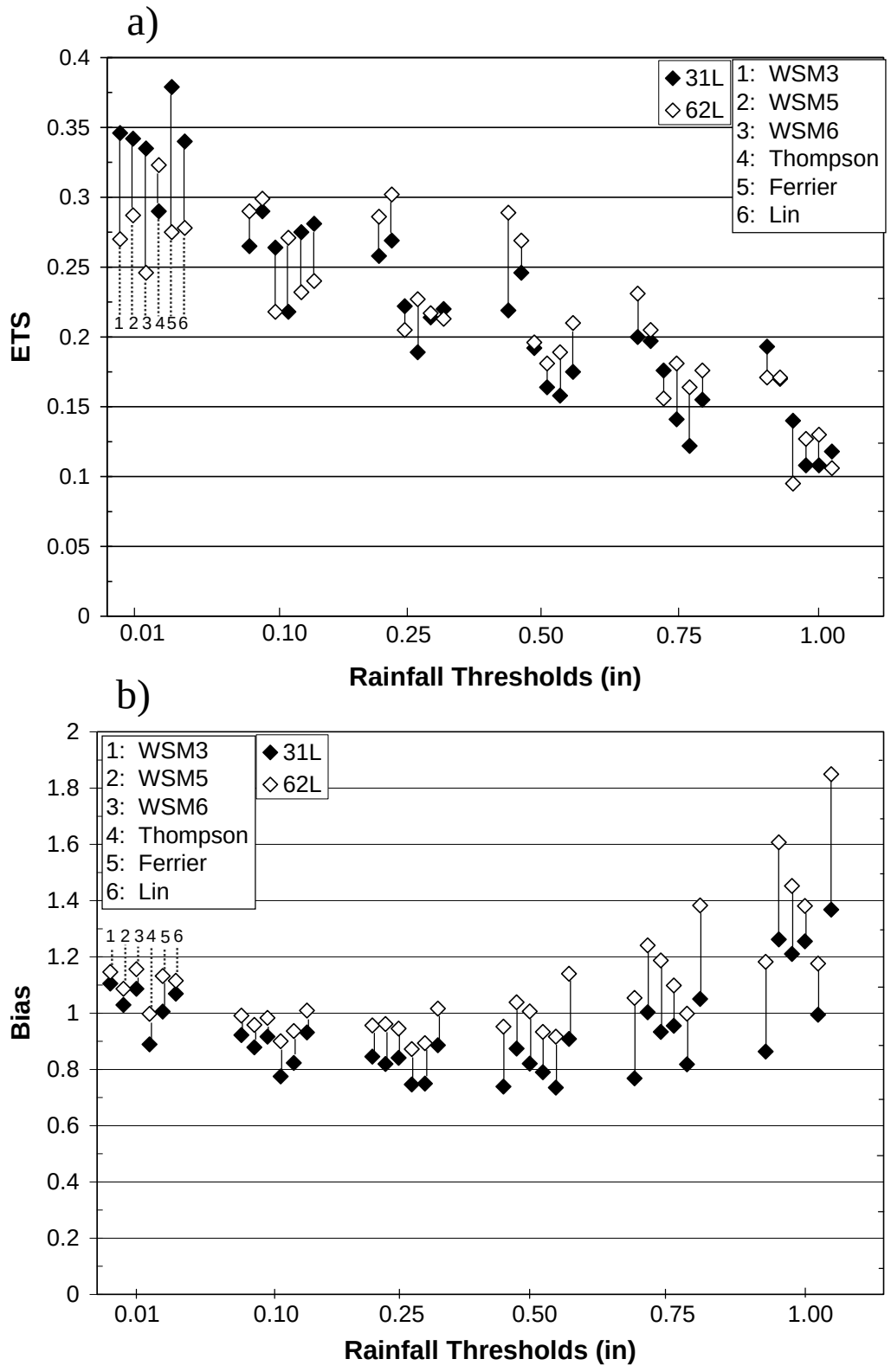

Figure 3. The 23-24 June 2003 (a) ETS and (b) Bias for the indicated rainfall thresholds, the six microphysical schemes (as sequenced in the inset) and for 31L and 62L. For each threshold, results for each scheme are presented as delineated by the dotted line for the 0.01" threshold.

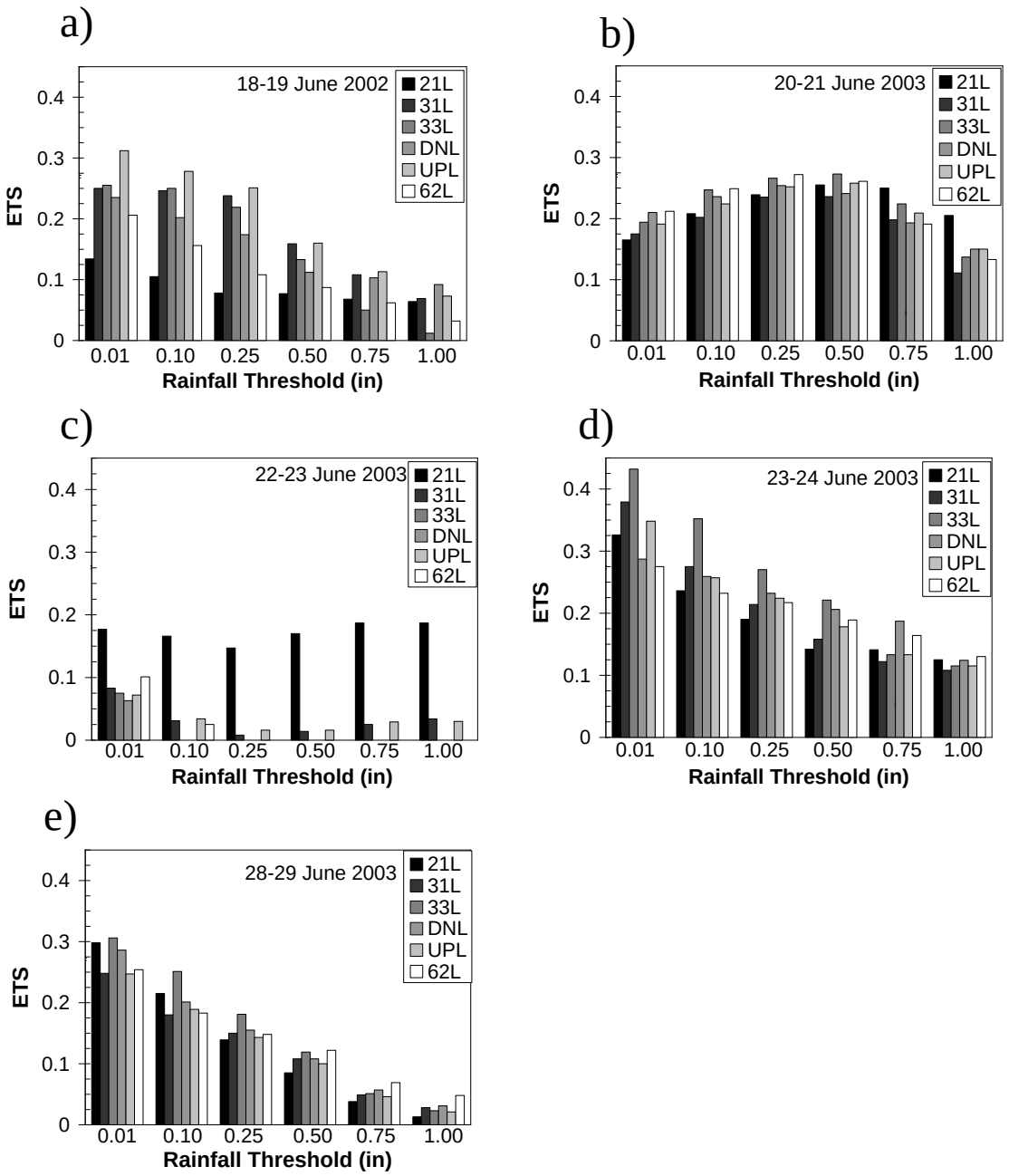

Figure 4. The ETS values for the indicated rainfall thresholds for the various VGRs (identified by the gray coding in the inset) for (a) 18-19 June 2002, (b) 20-21 June 2003, (c) 22-23 June 2003, (d) 23-24 June 2003 and (e) 28-29 June 2003.

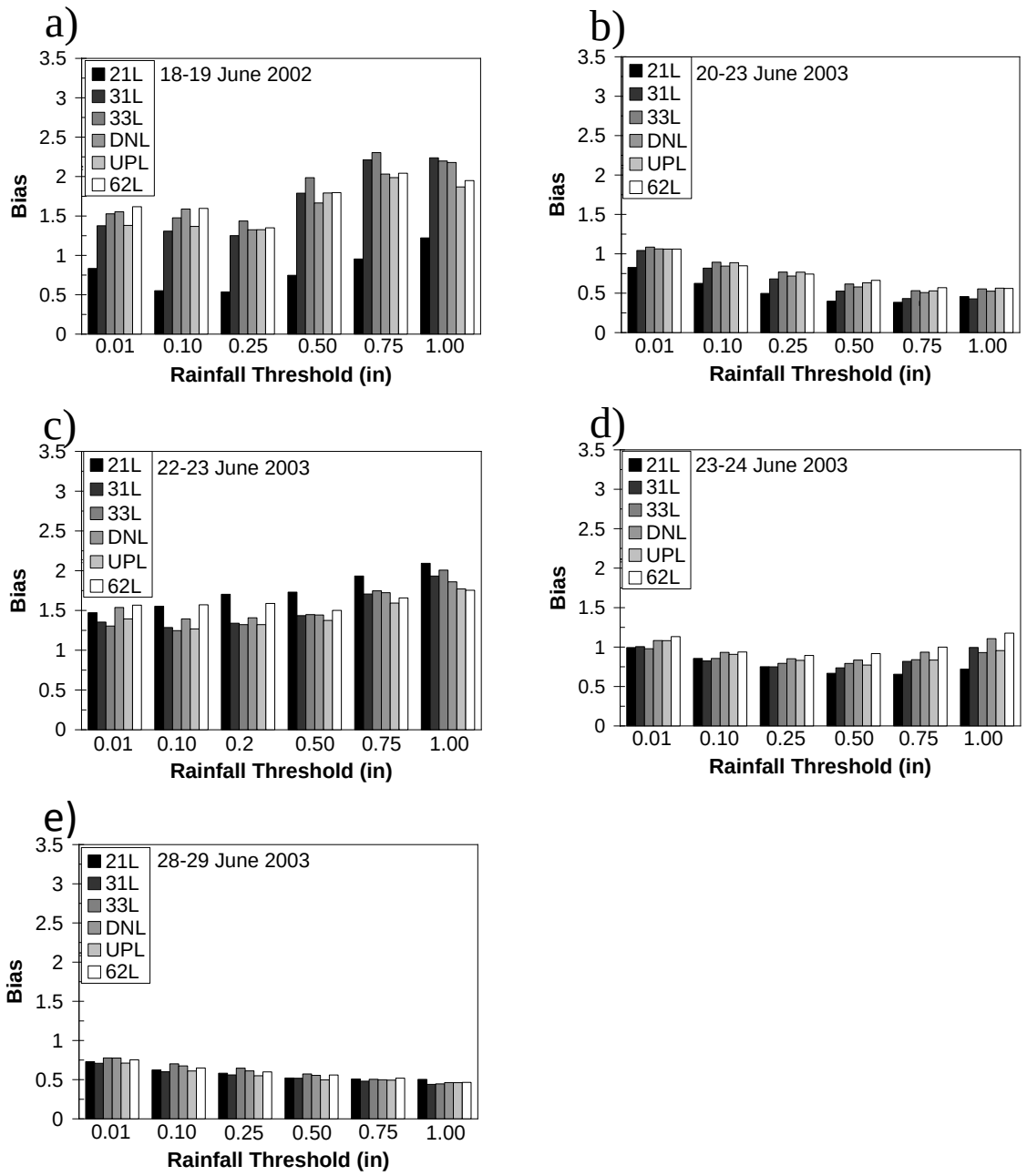

Figure 5. Same as in Fig. 4 except for Bias.

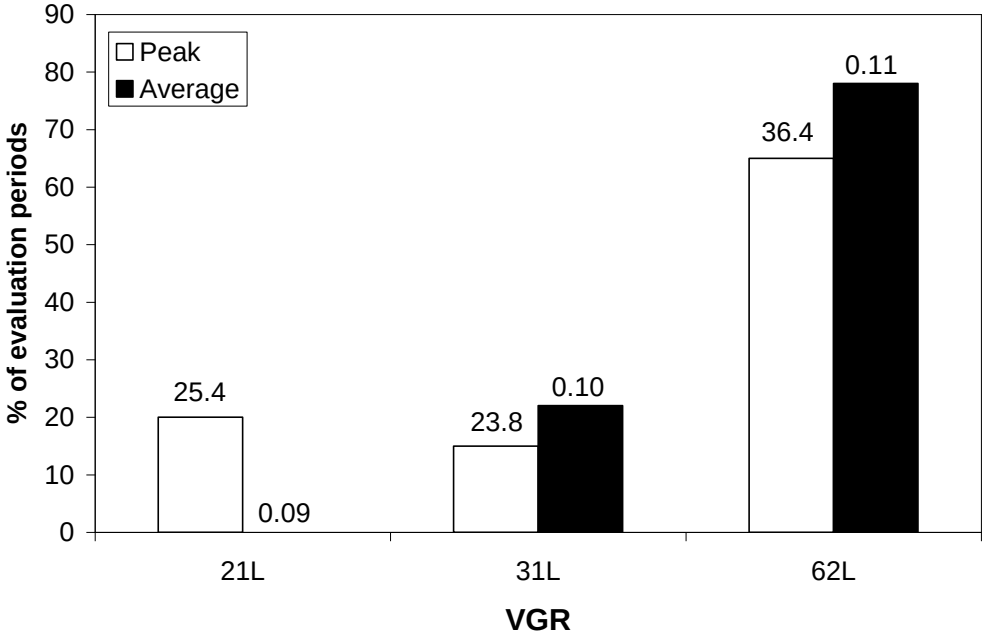

Figure 6. Percentage of evaluation periods (all hours and cases) with the highest 3D domain-peak upward vertical velocities (labeled peak) and with the highest 3D domain-averaged upward vertical velocities (labeled average). The values of the upward vertical velocities (m s^{-1}) are indicated above the bars.

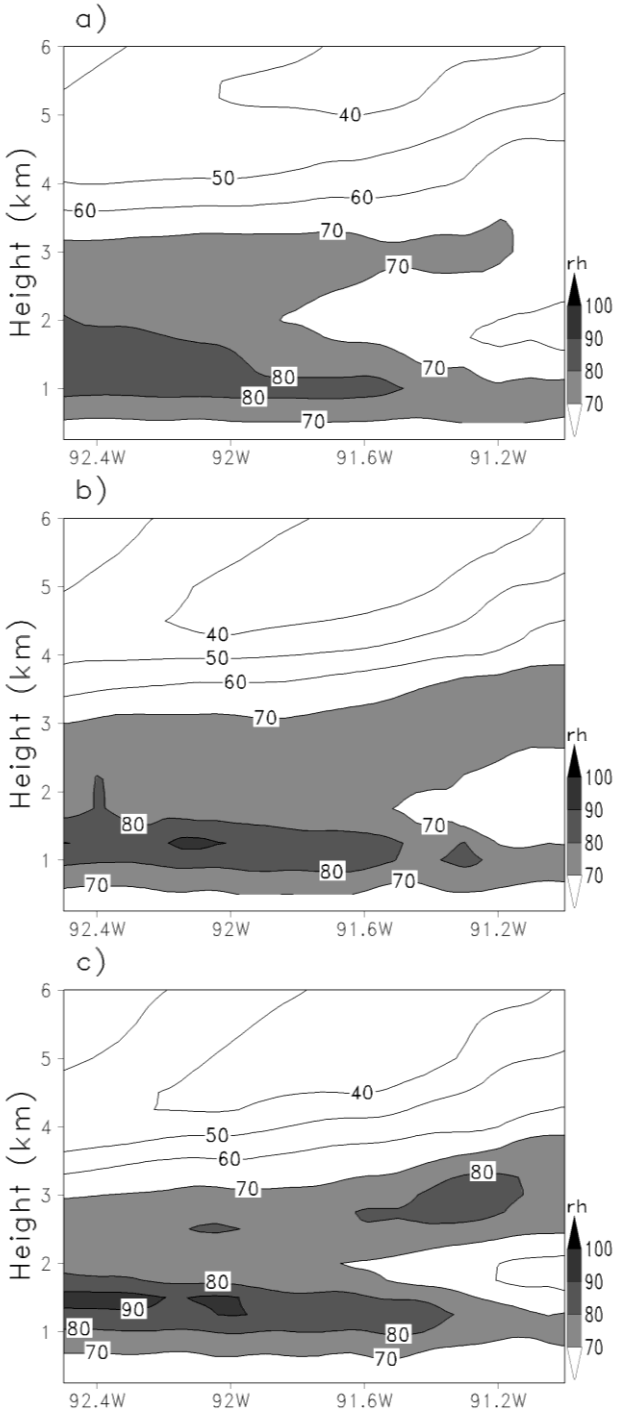

Figure 7. West-east vertical cross-section of relative humidity (as depicted by the line segment in Fig. 10b) at 00 UTC 19 June 2002 prior to convective initiation in the (a) 21L, (b) 31L and (c) 62L runs. The contour interval is 10% with values above 70% shaded. The height is above mean sea level.

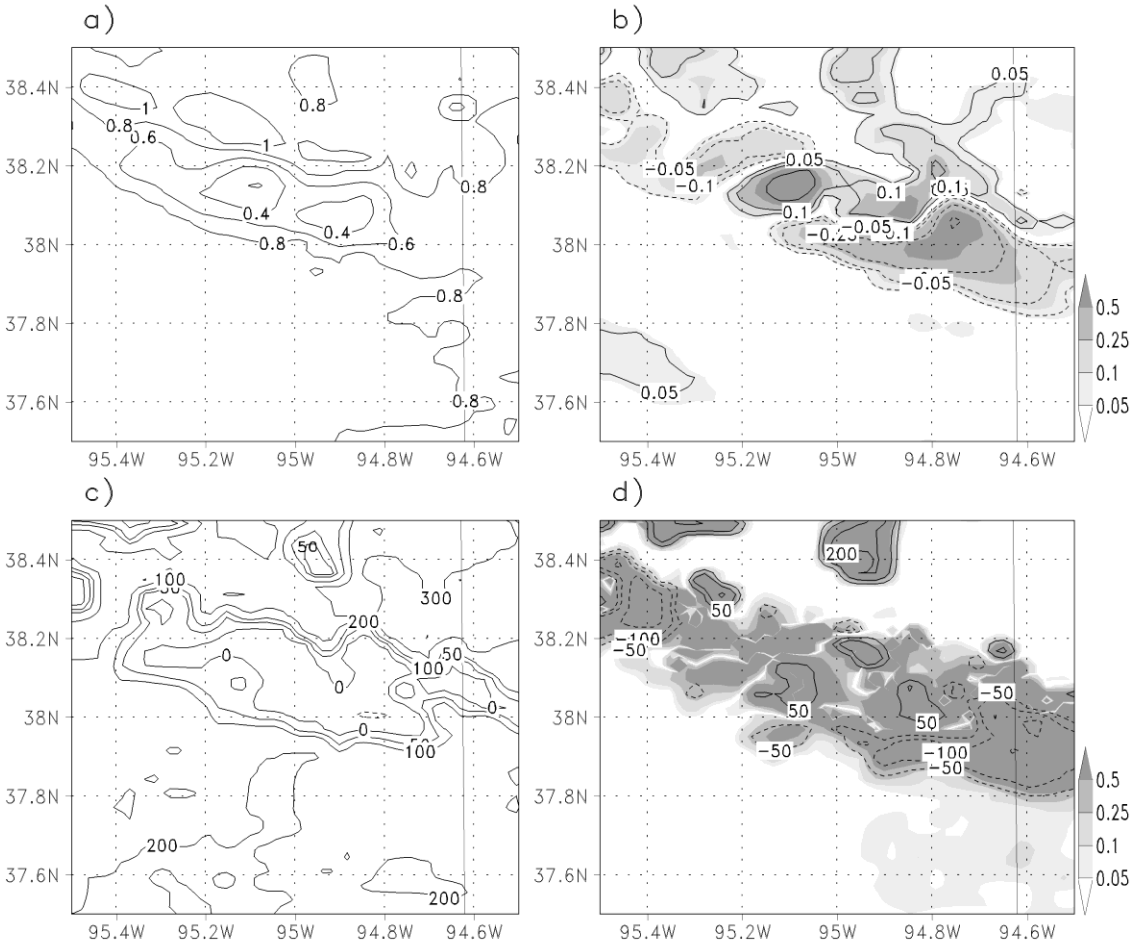

Figure. 8. The 21 UTC 22 June 2003 (a) 31L surface friction velocity, u_*, (m s^{-1}), (b) Δu_* (contoured) and $\Delta u_*/u_{*31L}$ (shaded), (c) 31L surface sensible heat fluxes, H_s ,(W m^{-2}), and (d) surface ΔH_s (contoured) and $\Delta H_s/H_{s31L}$ (shaded) (see text for the notation). The area presented is indicated by the dashed box in Fig. 11c. The contour interval in (a) is 0.2 m s^{-1} and the contour levels in (c) are 0, ±50, 100, 200 and 300 W m^{-2}. The contour and shading levels in (b) are ±0.05, ±0.10, ±0.25 and ±0.5 (in m s^{-1} when contoured). The contour levels in (d) are ±50, ±100 and ±200 W m^{-2}, while the shading levels are ±0.05, ±0.10, ±0.25 and ±0.5.

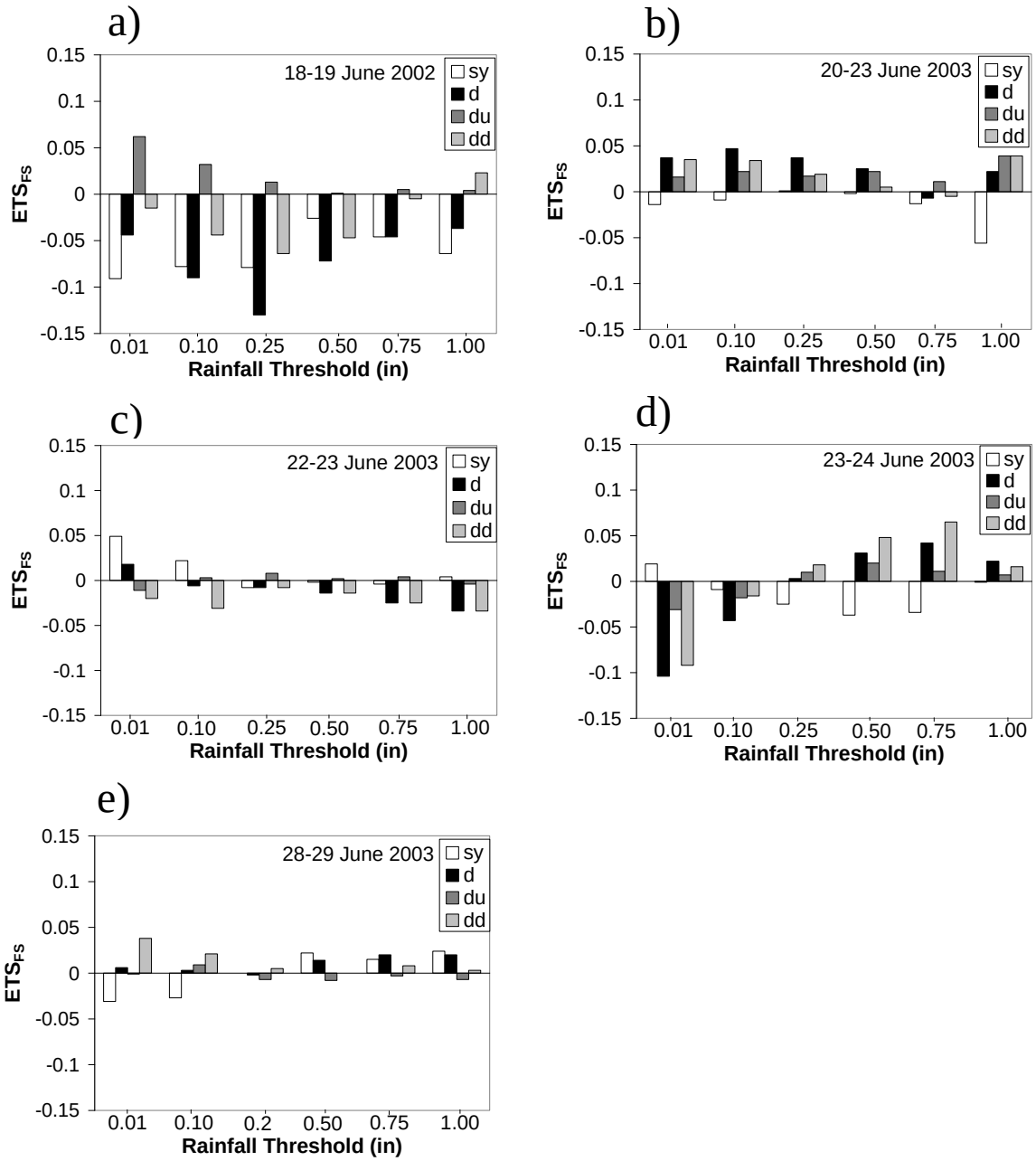

Figure 9. The values for the various terms in the factor separation analysis of ETS using Eq. 4 (identified by the gray coding in the inset) for the indicated rainfall thresholds for (a) 18-19 June 2002, (b) 20-23 June 2003, (c) 22-23 June 2003 and (d) 23-24 June 2003. ETS_{FS} represents the values of *sy*, *d*, *du* and *d*.

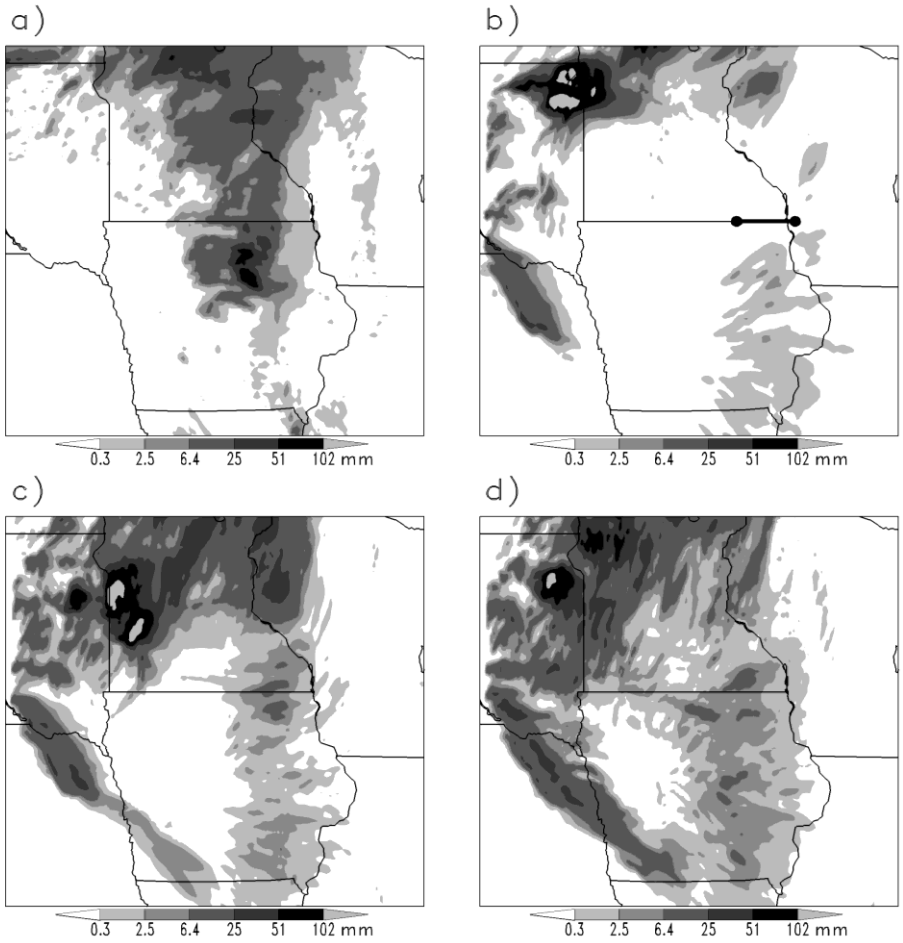

Figure 10. The 18 hour accumulated rainfall (mm) ending at 12 UTC 19 June 2002 from (a) observations, (b) the 21L run, (c) the 31L run and (d) the 62L run. The location of the west-east vertical cross section in (b) is presented in Fig. 7.

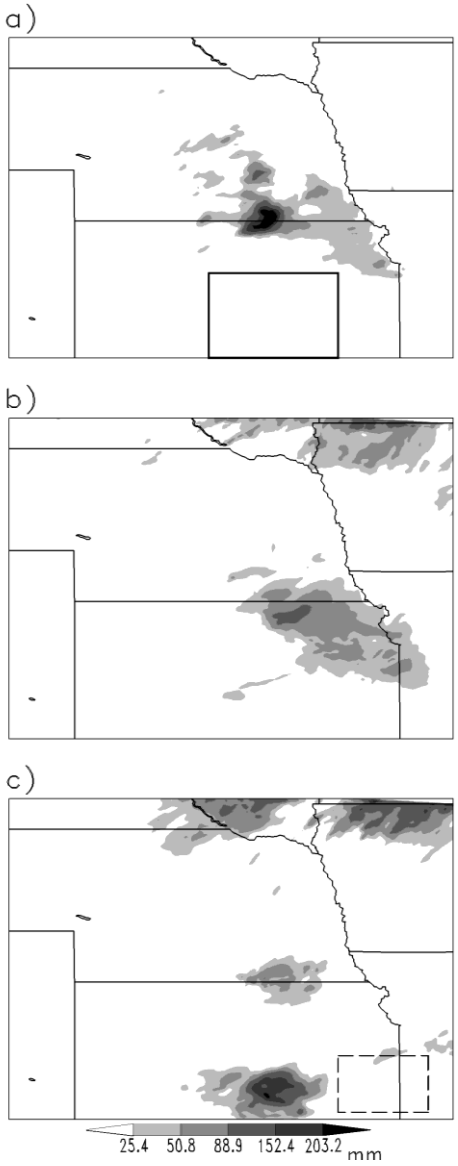

Figure 11. The 18 hour accumulated rainfall (mm) ending at 12 UTC 23 June 2003 from (a) observations, (b) the 21L run and (c) the 31L run. The area outlined by the solid box in (a) will be considered in Fig. 12. The area outlined by the dashed box in (c) was considered in Fig. 8.

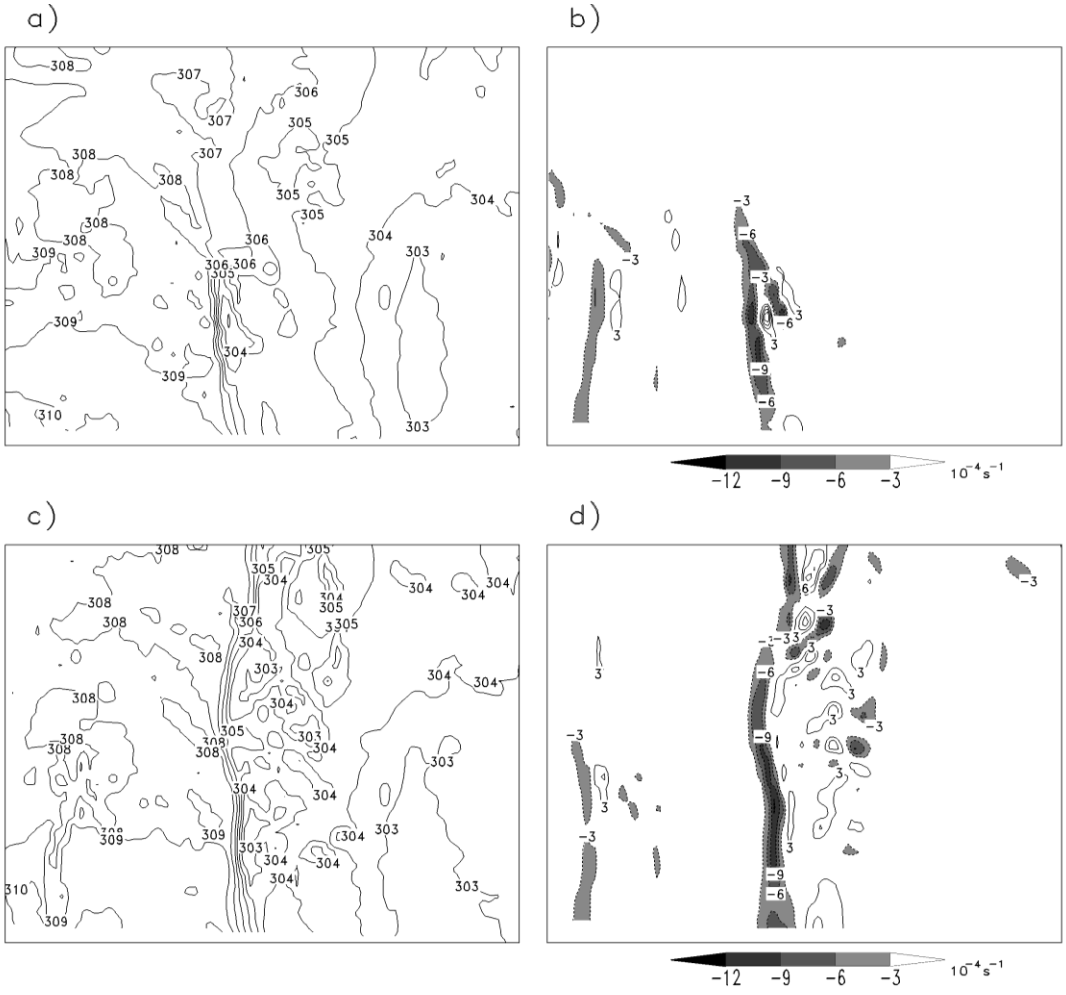

Figure 12. The 22 UTC 22 June 2003 (a) 2 m temperature (K), (b) near-surface horizontal wind divergence (10^{-4} s^{-1}) in the 21L run, (c) the 2 m temperature and (d) near-surface horizontal wind divergence in the 31L run. This area is indicated by the solid box in Fig. 11a. In (b) and (d) the divergence is represented by solid contours while convergence is represented by dashed contours with shading. The interval of contours and shading is $3 \cdot 10^{-4}$ s^{-1}.

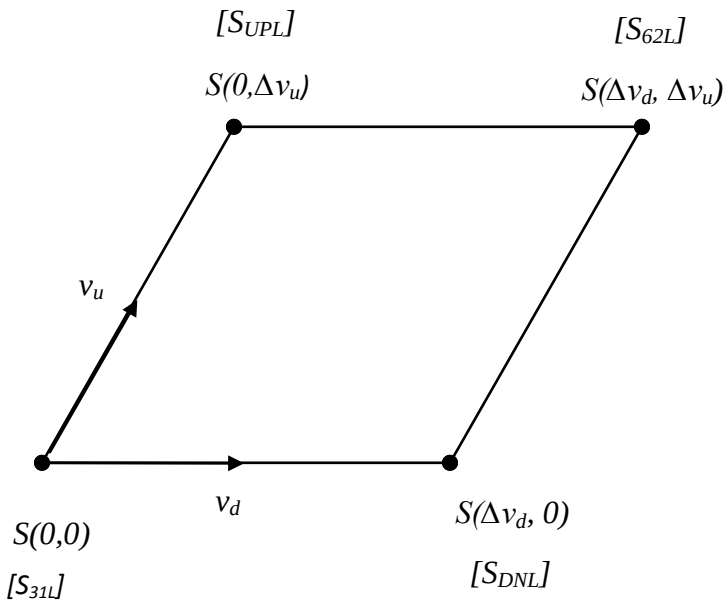

Figure B1. Schematic illustration related to the analytic and the finite difference approximation of Eq. B1 used for the factor separation analysis of DNL and UPL. The values of the analytic skill index, $S(v_d,v_u)$, and these based on the simulations (in brackets), are indicated.

Table 1. Values of ETS and Bias averaged over six runs using different microphysical schemes for the indicated rainfall thresholds for 23-24 June 2003 and for the indicated runs. The ETS and Bias values for 62L_det are bold (bold-italicized) to indicate an increase (decrease) in these values from 31L_det (similarly for 62L_ens and 31L_ens). See text for the description of the runs.

Run	Rainfall threshold (in)					
	0.01	0.10	0.25	0.50	0.75	1.00
			ETS			
31L_det	0.339	0.266	0.229	0.192	0.165	0.140
62L_det	***0.280***	***0.258***	**0.242**	**0.222**	**0.186**	***0.133***
31L_ens	0.352	0.303	0.260	0.222	0.181	0.134
62L_ens	***0.277***	***0.255***	**0.274**	**0.281**	**0.219**	**0.143**
			Bias			
31L_det	1.031	0.874	0.814	0.811	0.921	1.159
62L_det	**1.105**	**0.963**	**0.941**	**0.998**	**1.160**	**1.441**
31L_ens	1.197	1.039	0.919	0.868	0.986	1.146
62L_ens	**1.224**	**1.077**	**1.059**	**1.111**	**1.241**	**1.486**

Table 2. The values of ETS and Bias for the indicated rainfall thresholds averaged over five strongly forced cases and for various runs. The ETS and Bias for 21L, 33L, UPL and DNL are bold (bold-italicized) to indicate these values increased (decreased) from the 31L run. The 31L_WK and 62L_WK represent averages over two weakly forced cases where 62L_WK is bold (bold-italicized) to indicate these values increased (decreased) from the 31L_WK run. The runs 31L_KF and 62L_KF were performed using the five strongly forced cases and using the KF CP in the outer nest.

	Rainfall threshold (in)					
Run	0.01	0.10	0.25	0.50	0.75	1.00
			ETS			
31L	0.227	0.187	0.169	0.135	0.100	0.070
62L	***0.210***	***0.169***	***0.149***	***0.132***	***0.097***	***0.069***
21L	***0.220***	***0.186***	***0.159***	**0.146**	**0.137**	**0.119**
33L	**0.252**	**0.220**	**0.187**	**0.149**	***0.099***	***0.059***
UPL	**0.234**	**0.196**	**0.177**	**0.142**	**0.106**	**0.078**
DNL	***0.216***	***0.180***	***0.163***	***0.133***	**0.108**	**0.079**
31L_WK	0.311	0.322	0.322	0.252	0.130	0.066
33L_WK	**0.315**	**0.324**	***0.320***	***0.251***	**0.134**	***0.051***
62L_WK	***0.304***	***0.320***	***0.318***	**0.256**	**0.134**	**0.068**
31L_KF	0.233	0.226	0.192	0.156	0.130	0.116
62L_KF	0.229	0.197	0.172	0.149	0.112	0.085
			Bias			
31L	1.097	0.967	0.916	1.000	1.130	1.206
62L	**1.225**	**1.120**	**1.034**	**1.087**	**1.157**	**1.180**
21L	***0.970***	***0.841***	***0.813***	***0.812***	***0.886***	***0.999***
33L	**1.134**	**1.034**	**0.993**	**1.082**	**1.185**	**1.226**
UPL	**1.125**	**1.008**	**0.959**	**1.013**	***1.087***	***1.123***
DNL	**1.202**	**1.086**	**0.982**	**1.015**	**1.139**	**1.226**
31L_WK	1.418	1.484	1.530	1.569	1.766	2.005
33L_WK	**1.506**	**1.656**	**1.763**	**1.703**	**1.792**	**2.014**
62L_WK	**1.451**	**1.511**	**1.540**	***1.558***	***1.716***	***1.931***
31L_KF	0.821	0.691	0.644	0.678	0.757	0.829
62L_KF	0.962	0.847	0.809	0.811	0.837	0.850

Table 3. The values of the various terms in the factor separation analysis of ETS using Eq. 4 averaged over the 5 cases for the indicated rainfall thresholds (in ETS units). The value of *n* represents the number of situations for each threshold included in the averaging that satisfies either *sy* > 0 or *sy* < 0.

	Rainfall threshold (in)					
Term	0.01	0.10	0.25	0.50	0.75	1.00
			sy > 0			
sy	0.034	0.022	0.001	0.022	0.015	0.014
dd	-0.056	-0.031	0.019	0.000	0.008	-0.031
du	-0.021	0.003	0.017	-0.008	-0.003	-0.011
d	-0.043	-0.006	0.037	0.014	0.020	-0.014
			n			
	2	1	1	1	1	2
			sy < 0			
sy	-0.045	-0.032	-0.037	-0.017	-0.024	-0.039
dd	0.019	-0.009	-0.018	-0.002	0.008	0.009
du	0.026	0.012	0.010	0.011	0.008	0.013
d	0.000	-0.029	-0.045	-0.008	-0.009	-0.016
			n			
	3	4	3	4	4	3

CHAPTER 4: USING FALL SPEED DISTRIBUTIONS FROM A BIN MICROPHYSICAL SCHEME TO IMPROVE BULK SCHEME WARM-SEASON RAINFALL FORECASTS

Eric A. Aligo

William A. Gallus, Jr.

* Dept. of Geological and Atmospheric Sciences

Iowa State University

Ames, IA

[+]Dept. of Agronomy

Iowa State University

Ames, IA

(A paper to be submitted to Monthly Weather Review)

Corresponding author address: Eric A. Aligo, Iowa State University, 3010 Agronomy Hall,

Ames, IA , 50011 email: eric.aligo@noaa.gov

Abstract

Over the last decade horizontal grid spacing commonly used in research and forecast models has decreased almost an order of magnitude. With horizontal grid spacing decreasing, more attention is being given to potential improvements in microphysical schemes to provide accurate forecasts of warm-season mesoscale convective systems (MCSs). Summertime MCSs in the central and northern Plains provide a substantial portion of the annual rainfall to that region. Spectral (bin) microphysical schemes, rarely used today in operational and research settings because of their computational expense, may better represent the structure of convective systems, partly because of their ability to predict interactions between as many as 100 particle sizes, a task bulk schemes cannot do. While it is not yet feasible to use a bin scheme operationally, a technique has been developed to incorporate fall speed information from a bin scheme into a bulk scheme in order to improve sedimentation. This technique was tested in the Weather Research and Forecasting (WRF) Advanced Research WRF (ARW) model with a bin and bulk microphysical scheme in two and three dimensional model simulations.

In 2D simulations the fall speed modifications resulted in heavier convective rain in one case due to faster falling graupel in the convective region with all cases showing a narrower region of stratiform rainfall due to slower falling snow throughout the system. In 3D simulations, the fall speed modifications generally improved the rainfall forecasts. Biases generally decreased as fewer hydrometeors reached the ground and instead remained aloft contributing to a narrower stratiform rainfall region but larger anvil. Biases increased for the heaviest rainfall likely due to the faster falling graupel.

1. **Introduction**

Numerical weather prediction models at operational centers are typically run at horizontal grid spacings too coarse for moist convective processes to be treated explicitly. Convective parameterizations have been employed in order to resolve such sub-grid scale moist processes (Kain and Fritsch 1990). With increasing computer power, high-resolution model runs are becoming more common, and it has been shown that the horizontal grid spacing below which convective schemes can be omitted, while still adequately simulating mesoscale convective systems, is approximately 4 km (Weisman 1997). An example is the NCEP High-Resolution Window Forecast System (HIRESW), which consists of model runs of the Weather Research and Forecast (WRF) Advanced Research WRF (ARW) and the WRF nonhydrostatic mesoscale model (NMM), both run without the use of a convective parameterization. Treating moist convective processes explicitly by decreasing horizontal grid spacing should result in better forecasts of moist convective processes (Fritsch and Carbone 2004). Without convective parameterizations, precipitation processes are represented completely by grid-scale microphysical schemes.

The most commonly used microphysical schemes are single moment schemes, which predict only the mass mixing ratios of different hydrometeor types (e.g. Lin et al. 1983; Cotton et al. 1986; Hong and Lim 2006). More sophisticated microphysical schemes are double moment in some hydrometeor categories such as rain and cloud ice (Thompson et al. 2008), and some are double moment in all hydrometeor categories (Ferrier 1994, Morrison and Gettleman 2008). Typically, a double moment scheme predicts the mass mixing ratios and number concentrations of one or more hydrometeor types. Milbrandt and Yau (2005) discuss the advantages of double

moment versus single moment schemes, including the ability for the particle mass and number concentration to act independently of each other and the ability for the slope intercept parameter, which is held constant in single moment schemes, to more realistically vary in time and space. Triple moment schemes are used less frequently because of their computational expense and predict the mass mixing ratios, number concentrations and reflectivity of different hydrometeor types (Milbrandt and Yau 2005).

Even more sophisticated spectral (bin) microphysical schemes have appeared occasionally in studies; however, such schemes are far from being implemented operationally because they are computationally expensive. Bin schemes are double moment schemes in that they predict both mixing ratio and number concentration, but differ from double moment bulk schemes in that they allow different-sized particles to exist at each model grid point. As many as 100 bins or different-sized particles can exist in a bin scheme at a single grid point (Houze 1993). Sedimentation is treated more realistically in bin schemes; the mean sedimentation velocity used in bulk schemes can result in spatial errors in the interactions of different hydrometeor types (Lynn et al. 2005).

Various studies have performed microphysical sensitivity tests altering particle densities (Gilmore 2004b), using different fall speed relations (Colle and Mass 2000) and using different diameter assumptions (Potter 1991), all to better understand the uncertainties associated with microphysics and how these uncertainties can affect storm structure and surface precipitation. Jankov et al. (2005) evaluated the potential of using different microphysical schemes as part of an ensemble forecast system and found substantial differences in predicted warm-season surface rainfall between the different schemes. Lynn and Khain (2007) compared a bin scheme to

different bulk schemes and found the bin scheme to produce better surface convective rain rates and a better defined stratiform cloud. They attributed the improved forecast to better depiction of hydrometeor distributions, and more specifically, the presence of slower falling particles in the bin scheme being advected farther away from the updraft region.

Warm-season rainfall is often associated with linear systems that have trailing stratiform (TS) regions, but a smaller percentage of systems exhibit a leading stratiform (LS) region also exist and differ in terms of kinematics and microphysical processes. Parker and Johnson (2000) showed that at least initially hydrometeor advection determines the location of the stratiform region with respect to the convective region in both TS and LS systems. The transport of buoyant air rearward from the convective region can result in further ascent in the stratiform region (Knupp and Cotton 1987) in TS systems with ascent being aided by condensation, freezing and deposition (Houze 1982; Churchill and Houze 1984). Parker (2004c) and Storm et al. (2007) showed that LS systems can be sustained by microphysical processes such as melting and evaporation, which can act to destabilize the atmosphere ahead of the convective line. Both types of MCSs can produce severe weather, but Gallus et al. (2008) showed that trailing stratiform (TS) systems were most often associated with wind damage, while leading stratiform (LS) systems were most often associated with hail and tornadoes.

Since a 3D bin simulation could not be run in this study because of the computational expenses associated with such a scheme, an attempt was made instead to use 2D bin fall speed information in 3D bulk scheme simulations. We employed a probability matching technique that used fall speed information from a bin scheme to drive a bulk scheme model simulation in order to examine the effects of this better representation of sedimentation. We also evaluated use of the

technique for both LS and TS systems to determine if any impacts differed. The probability matching technique has the potential to be a valuable tool for operational centers that must keep computational expenses minimized. Discussion of the model and data used for the 2D and 3D experiments are in Section 2 followed by results in Section 3 and conclusions in Section 4.

2. Data and Methodology

a. Model configuration and data

Since the computational costs of a bin microphysical scheme are very large the bin scheme had to be run in 2D. Direct comparisons between the bin and bulk schemes also restricted some bulk scheme simulations to 2D. However, 3D bulk scheme simulations were used when only features of the bin scheme were incorporated into the bulk scheme.

Two dimensional (2D) Weather Research and Forecast (WRF) Advanced Research WRF (ARW) (Skamarock et al. 2005) idealized simulations at a grid spacing of 1 km were performed using the Geresdi bin microphysical scheme (Geresdi 1998; Rasmussen et al. 2002) and the Thompson bulk microphysical scheme (Thompson et al. 2008). The Thompson scheme was used because it is one of the most sophisticated schemes available in the WRF model (it is double moment in ice and rain).

The three idealized simulations in this study simulate a squall line in the x direction (east-west) and were initialized with three distinct soundings. The first two soundings produced TS systems (Weisman et al. 1988 default sounding provided with the WRF package, and a modified sounding from 12 June 2002 from the International H_2O Project [IHOP; Parsons 2002]), while

the third sounding produced a leading stratiform (LS) system (Parker and Johnson 2004c). Convection was initiated with a warm thermal perturbation having a 4-km radius and a maximum perturbation of 3K at the center of the domain. A smaller perturbation was used for the 12 June 2002 case to prevent gravity-wave initiated convection from interfering with the main system. The simulations were run for six hours using a horizontal grid spacing of 1 km with 80 vertical levels and 600 horizontal grid points. The idealized runs used flat terrain, and did not consider radiation, surface fluxes or frictional effects.

A total of four 3D real cases were run using the Thompson scheme, and consisted of a 1 km domain nested within 3 km and 9 km domains using two-way nested interfaces. The four cases included: 12-13 June 2002, 19 June 2002, 30-31 May 2003 and 09-10 June 2003, and were integrated over 18, 15, 12 and 15 hour periods, respectively (Fig. 1). The 12-13 June 2002 and 30-31 May 2003 cases depicted LS systems while the other two depicted TS systems. All cases were initialized at 18 UTC, except for the 19 June 2002 case, which was initialized at 00 UTC. The initialization time and length of the integrations were chosen to allow enough time (at least 6 hours) for model spin up and in consideration of available computational resources. The 09-10 June and 30-31 May 2003 cases were part of the Bow Echo and Mesoscale Convective Vortex Experiment (BAMEX; Davis et al. 2004) project

The model physical configuration is that described in Aligo et al. (2007) with the exception of the planetary boundary layer (PBL) scheme and the land surface model (LSM), which in the present study are, respectively, the Mellor-Yamada-Janjic (MYJ; Janjic 2002) scheme and the Noah LSM (Ek et al. 2003). In addition to the above configuration, the 9 km

outer domain used the Betts-Miller-Janjic convective scheme (Betts 1986; Betts and Miller 1986; Janjic 1994) which currently is used operationally at NCEP.

b. Experimental design

The following describes the treatment of fall speeds in the Thompson and Geresdi schemes followed by a description of the two experiments. The tools used to evaluate quantitative precipitation forecasts (QPF) in 3D simulations also are presented.

Falling particles often follow the power law relation from Ferrier (1994):

$$V(D) = \left(\frac{\rho_0}{\rho}\right)^{1/2} \alpha D^{\beta} e^{-fD}, \qquad (1)$$

where ρ_0 is a reference air density usually chosen to be close to the surface, ρ is the air density at a particular altitude, D is the diameter of the particle and α, β and f are constants that are defined in Table 1. The hydrometeor fall speed formulation deviates from (1) for liquid and graupel in Geresdi with droplet fall speeds following three separate equations found in Pruppacher and Klett (1997). Graupel fall speeds in the Geresdi scheme are described in Rasmussen and Heymsfield (1987).

For the Thompson scheme, mean mass-weighted fall speeds are determined for cloud ice, rain, snow and graupel using the relation:

$$\hat{V} \equiv \frac{\int_0^\infty V(D)m(D)N(D)dD}{\int_0^\infty m(D)N(D)dD}, \qquad (2)$$

where $V(D)$ also follows (1), $m(D)$ is described using the following power law relation:

$$m(D) = aD^b, \qquad (3)$$

and $N(D)$ is the particle number concentration. The coefficients, a and b, in (3) are microphysical-scheme dependent, and will not be shown here for the sake of brevity.

The first of the two experiments modified the Thompson fall speeds and is denoted as hybrid Thompson. The main objective of this experiment was to determine the effects of using bin fall speeds in the simulation of MCSs in 3D Thompson bulk simulations. Rain fall speeds from the bin scheme were not used because of the very crude method that scheme uses to treat melting ice. Tests were done with and without the use of the bin rain fall speeds in the experiment, and only minor differences in the simulated storm structure and surface precipitation were noticed. Additionally, Colle and Mass (2000) noted that ice microphysics is more important than warm rain microphysics in developing the stratiform region of convective systems. Cumulative frequency tables of cloud ice, snow and graupel fall speeds were constructed for the control Thompson and bin scheme idealized simulations using the ten minute output data over the entire length of the simulations. In order to adjust the 3D Thompson fall speeds in real time, both the 2D Thompson and Geresdi cumulative frequency tables had to be added to the Thompson microphysics subroutine. Fall speeds from the real time run of the 3D Thompson scheme were then matched to the fall speeds in the 2D Thompson cumulative frequency table, so that a frequency value could be obtained, and matched to the frequency value

in the 2D bin scheme cumulative frequency table. The fall speed that the bin scheme would have for that frequency was then used in the 3D bulk simulation. This probability matching technique (Ebert 2001) was applied at every grid point and model time step. This approach forced the hybrid Thompson simulations to use the fall speed distributions inherent to the Geresdi bin scheme while also retaining computational efficiency by not having to add hundreds of new arrays to the microphysics subroutine.

The second experiment, denoted as hybrid Geresdi, was simply a sensitivity test that computed mass-weighted fall speeds and assigned these fall speeds to each of the 36 size-dependent bins, thus enforcing a uniform fall speed value at each grid point. Such a treatment of ice, snow and graupel fall speeds in the bin scheme should have some impact on the structure of the stratiform and the convective regions of the MCS as well as on the surface rainfall patterns that might resemble those of bulk schemes.

To better understand how altering the fall speeds can impact the microphysical processes associated with both TS and LS systems, a microphysical budget was computed following Colle et al. (2005):

$$\overline{Pqqqq} = \frac{\sum_{i,k} p^*(i) \times Pqqqq(i,k) \times \Delta\sigma(k)}{\sum_{i,k} p^*(i) \times WVL(i,k) \times \Delta\sigma(k)}, \qquad (4)$$

where $Pqqqq(i,k)$ is a source/sink term averaged for the layer between two sigma levels, $WVL(i,k)$ is the water vapor loss rate (*pri_inu+ pri_ide+ prs_ide+prs_sde+ prg_gde+ prw_vcd* in the Thompson scheme), $\Delta\sigma$ is the distance between any two sigma levels, and $p^*(i)$ is the pressure difference between the top of the model and the surface. Source/sink terms in the

tendency equations of Thompson are provided in the appendix. Since the tendency equations of Geresdi are similar to those in Thompson only those terms from Thompson will be shown here for the sake of brevity. Colle et al. (2005) performed their budget over a volume fixed in space and time. In this study, however, the budget was evaluated beginning one hour into the simulation and for the convective and stratiform regions separately. Note that while all of the source/sink terms were accumulated over every model time step (2 seconds), only ten minute accumulations were used for the budget computations. For a grid point to be considered in the budget analysis, it had to be in either the convective or stratiform region for the time being evaluated and the previous time (ten minutes earlier). This condition limited the grid points being evaluated to those that likely were in the convective or stratiform region throughout the ten minute time interval over which the microphysical processes were accumulated. It is important to note that $WVL(i,k)$ in the Thompson scheme will naturally be different from that in the Geresdi scheme. In this study, $WVL(i,k)$ is the time-averaged water vapor loss for the combined stratiform and convective regions of the control simulation for a given species of water, thus making comparisons between the convective and stratiform regions as well as control and hybrid simulations possible.

To separate the convective region from the stratiform region for the microphysical budget analysis, an algorithm by Steiner et al (1995), which is a modification of the Churchill and Houze (1984) algorithm, was used. This algorithm uses instantaneous values of radar reflectivity to perform the separation of rainfall into the convective and stratiform regimes, and assumes that any reflectivity value of 40 dBZ or greater is convective. Surrounding grid points are considered convective if they exceed a value dependent on the mean background reflectivity.

Quantitative and qualitative evaluations of QPF skill were performed. The quantitative evaluations were done using the Equitable Threat Score (ETS; Schaefer 1990) and Bias, where

$$\mathrm{ETS}=\frac{\mathrm{CFA}-\mathrm{CHA}}{F+O-\mathrm{CFA}-\mathrm{CHA}}, \tag{5}$$

$$\mathrm{CHA}=\frac{FO}{V}, \tag{6}$$

and

$$\mathrm{Bias}=\frac{F}{O}. \tag{7}$$

In (5), (6) and (7), each variable indicates the number of grid points at which: (i) rainfall was correctly forecasted to exceed the specified threshold (CFA), (ii) rainfall was forecasted to exceed the threshold (*F*), (iii) rainfall was observed to exceed the threshold (*O*), and (iv) a correct forecast would occur by chance (CHA), where *V* is the total number of evaluated grid points. The NCEP 4 km gridded Stage IV multi-sensor data (Baldwin and Mitchell, 1997) were used for verification. It should be noted that given the study goals it is advantageous to use the ETS and Bias as they provide a simple method to score the overall QPF for a given case while being compared to other cases. These skill indices, however, are known to penalize forecasts relatively more as the horizontal grid interval decreases due to possible small spatial or temporal shifts in rainfall forecasts (Mass et al. 2002). However, since these shifts are assumed to be random, these indices are assumed adequate for the comparative needs of this study as all simulations use the same horizontal grid spacing.

3. Results

An analysis of results from the 2D idealized simulations will be followed by an analysis of results from the 3D simulations, with the latter analysis focusing mostly on QPF skill.

a) 2D idealized simulations

A detailed evaluation of the storm structure, microphysical budget and rainfall patterns for the Thompson simulations will be presented first. Since no substantial differences in the microphysical budget were noted between the control and hybrid Geresdi simulations, a microphysical budget analysis was not included for these simulations.

1) THOMPSON VERSUS HYBRID THOMPSON

i) Storm structure

In the hybrid Thompson simulations, the stratiform rainfall area decreased for all three cases as indicated by the Hovmöller diagrams of rain rate (Fig. 2). The horizontal extent of the system increased above the melting level (575 hPa) and in the anvil region (250 hPa) as depicted by simulated radar reflectivity for the 12 June 2002 simulation (Fig. 3). Similar features in the radar reflectivity were simulated in the other two cases but are not shown here.

As a complement to the Hovmöller diagrams of rainfall, cumulative frequency distributions of accumulated rainfall and rain rate are presented in units of inches where 1 inch = 25.4 mm. The accumulated 6-hour rainfall plot (Fig. 4) indicates an increased frequency of the lightest rainfall (< 0.5 in. where 1 in. = 25.4 mm) and a decreased frequency of the heaviest rainfall in the hybrid simulations. An increased frequency of rainfall (Fig. 5) occurred in the 0.01-0.1 in. rainfall bin amount with a decrease for heavier rainfall, although differences between the control and hybrid simulations were smaller for the heavier rainfall. The increased frequency in the lightest rainfall rate in all three cases was due in part to the heavier stratiform rain diminishing in intensity.

Since bin schemes can depict a wider spectrum of fall speeds than bulk schemes, it was not surprising for the Geresdi scheme to have faster falling graupel compared to the Thompson scheme (Fig. 6a), and a higher frequency of the slowest fall speeds (~ 0.21 m s^{-1}). A wider distribution was also seen for snow (Fig. 6b). It was surprising, however, to see a narrower stratiform rain region in the hybrid simulation (Fig. 2). The spatial distribution of graupel fall speeds four hours into the simulation (Fig. 7a,b) for the control and hybrid Weisman simulations showed higher fall speeds in the hybrid simulation compared to the control simulation with a narrow band of 9 m s^{-1} values extending through a deep layer in the convective region in the hybrid simulation and peak values as large as 13 m s^{-1}. With faster falling graupel, the downward fluxes of graupel were larger (not shown), and the particles fell out sooner near the convective region, and contributed to the larger rain rates in the hybrid simulation. Also, fewer graupel particles were advected away from the updraft region potentially limiting the horizontal extent of the stratiform region.

The smaller stratiform region in the hybrid Thompson simulation for the Weisman case could also be explained by the changes to the spatial distribution of snow fall speeds. In contrast to what was seen with graupel fall speeds, snow fall speeds decreased in all parts of the system. An example of this can be seen in Fig. 7d, which is a vertical cross section of snow fall speeds valid four hours into the simulation. The slower fall speeds reduced the downward fluxes of snow in the stratiform region, which resulted in less fallout of rainfall below the melting level. The slower fall speeds also resulted in more snow particles being advected farther away from the main updraft region and helped produce the slightly larger anvil that was seen in Fig. 3c-d. Similar features of snow and graupel fall speeds were also noted in both the 12 June 2002 and LS simulations (not shown).

The cumulative frequency plots in Fig. 6a discussed previously show that for the very slow falling graupel, the probability matching technique forced the Thompson fall speeds to be adjusted down because of the large spike in fall speeds in the first illustrated bin. For faster falling graupel in or near the convective region, however, Thompson graupel fall speeds were adjusted up. The Geresdi graupel fall speed distribution resulted in graupel particles attaining faster speeds in the convective region, which then allowed these particles to fall out sooner.

ii) Microphysical budget

The most substantial differences in the microphysics occurred between the two different morphologies (TS versus LS), and not between the control and hybrid simulations, but even the TS and LS differences were only modest. In the stratiform region, rain water was produced mostly by melting snow (SMLT) and to a lesser extent melting graupel (GMLT) in all cases (Fig.

8). Morrison et al. (2009) identified snow and graupel melting as the largest contributors to rain in the stratiform region with the smallest contributions from collision and coalescence in their simulations. The reverse was true in the convective region in their simulations, and also in the simulations in this paper with rain collecting graupel (RCG) and rain collecting cloud water (RCW) the most important in the control and hybrid simulations. The results in this paper agree with those from McCumber et al. (1991), which showed larger snow mixing ratios in the stratiform region, thus contributing more than graupel to the stratiform rainfall (not shown). Melting snow and graupel contributed less to the budget in the hybrid simulations, and this supports what was shown in the vertical cross sections and hövmuller diagrams. Rain evaporation was larger in the 12 June 2002 case, compared with the other TS case, but this is not surprising considering that the environment in the sounding used to initialize the 12 June 2002 case was drier (not shown) .

In both control and hybrid simulations, horizontal snow advection was the largest producer of snow in the stratiform region (Fig. 9). The importance of rearward hydrometeor advection in the development of the stratiform region has been studied by many (e.g., Smull and Houze 1987; Hamilton and Johnson 1988; Gallus and Johnson 1991, Braun and Houze 1994; Parker and Johnson 2000). In this paper, advection of snow was nearly balanced by snow melting (SMLT), sublimation (SDEP) and rain collecting snow (RCS) combined. Rutledge and Houze (1987) noted that about one quarter of surface rainfall in the stratiform region is due to advection of hydrometeors, and additional ice growth via mesoscale ascent is needed to have a full-fledged stratiform region; however for the cases in this study, the presence of snow in the stratiform region was in large part due to horizontal advection.

In the convective region, autoconversion of cloud ice to snow (SAUT) was equally important as snow deposition (SDEP) in the LS simulation, but SAUT was negligible in the TS cases (Fig. 9). More cloud ice in the LS case likely explained the larger autoconversion in the LS case versus the TS cases (not shown). The higher cloud ice might have been the result of more cloud water freezing (CWF) in the LS versus TS simulations (Fig. 10), which could have been a result of increased cloud water condensation (COND; Fig. 11). More condensation in the convective region in the LS simulation compared to the TS simulations might have been due to an intrinsic difference between the LS and TS systems as sublimation of snow and cloud ice ahead of the convective line below the cirrus cloud is a common feature of LS systems, and will cool and moisten the environment and even increase the instability ahead of the convective line, helping to sustain the leading stratiform system (e.g., Parker and Johnson 2004c; Storm et al. 2007). The higher relative humidity contributes to earlier grid cell saturation, and might explain the increased importance of condensation in the convective region in the LS simulation.

The most noteworthy feature in Fig. 11 may be the change in sign of the horizontal advection of water vapor in the stratiform region from negative in the two TS cases to positive in the LS case. For the TS systems, an influx of greater water vapor (up to $10 \cdot 10^{-3}$ kg kg^{-1} over the last five hours of the simulation) associated with the front to rear flow was negated by a reduction of water vapor associated with the rear inflow jet with amounts as large as $-10 \cdot 10^{-3}$ kg kg^{-1}(Fig. 12) in the same five hour period. The large swath of negative values near $-1 \cdot 10^{-3}$ kg kg^{-1} was a consequence of subsidence associated with the rear inflow jet and drier air from the surrounding environment (not shown) being advected toward the convective line.

The source of water vapor from horizontal advection present in the hybrid, but not in the control simulation of the LS system, was due to a less developed stratiform region in the hybrid simulation. The stratiform region in the control simulation of the LS system was better developed (Fig. 11), and this resulted in more moistening just ahead of the convective line. Drier air was advected toward the leading edge of the system around 500 hPa leading to a reduction of water vapor out ahead of the LS system (Fig. 13a). In the hybrid simulation, a weaker stratiform region led to less moistening and relatively less dry air being advected in toward the leading edge of the system (Fig. 13b). Additionally, less cooling from snow and ice sublimation (Fig. 13c,d) decreased the precipitation drag and associated subsidence, which led to larger average upward vertical velocities in the hybrid simulation (Fig. 13e,f). With larger average upward velocities, dry air remained aloft and allowed relatively moister air to be advected toward the front portion of the system. The reduced moistening at mid-levels from sublimation of ice and snow just ahead of the convective line coupled with the moister air being advected toward the system at lower levels resulted in a net positive source of water vapor from horizontal advection in the hybrid simulation.

There were only minor differences in the budget for graupel between the LS, TS, control and hybrid simulations (Fig. 14). Processes involving graupel in the stratiform region of the LS case were small compared to those in the TS cases as the stratiform region was weaker in the LS case as mentioned earlier. This was true for snow and rain as well. Rain collecting snow (RCS) was the largest producer of graupel in the convective region, and rain collecting graupel (RCG) was the largest sink and microphysical process associated with the graupel tendency.

2) GERESDI VERSUS HYBRID GERESDI

The following describes the results from 2D idealized bin scheme experiments that explored the sensitivity of TS and LS systems to the replacement of bin fall speeds with mass-weighted fall speeds. Fig. 15 shows three hovmöller diagrams of rain rate for the two TS and one LS cases. In the hybrid Geresdi simulation, the stratiform region was more widespread horizontally in all cases. This was not as clear in the LS simulation with rain rates, but could be seen in the radar reflectivity field (Fig. 16), which showed a wider system just above the melting level at 575 hPa (Fig. 16a,b) and at 250 hPa (Fig. 16c,d).

Faster falling snow in the hybrid versus control Geresdi was simulated on average in a large portion of the system, especially near the melting level away from the convective region for the Weisman case. Fig. 17 shows vertical cross sections of snow fall speeds from the control (Fig. 17a) and hybrid (Fig. 17b) bin simulations valid three hours into the simulation. A similar feature of faster falling snow in the hybrid versus control Geresdi was noted in the remaining three hours of the simulation. As in the hybrid Thompson simulations, this feature enhanced the downward snow fluxes and led to higher stratiform rainfall. The higher fall speeds could be seen also in the shift in the fall speed distribution of snow to higher values in the hybrid Geresdi simulation (Fig. 18). The fall speed modifications altered the size distribution function (Fig. 19) by shifting the particles from the small sizes to the larger sizes resulting in larger fall speeds of snow. At low-levels, near the melting level, larger particles were more likely to be present thus explaining the faster falling snow there in the hybrid simulations. It is interesting to note that in the first two hours of the simulation, slower falling snow was generally simulated below 300 hPa. It was not until close to three hours into the simulation, when snow reached 900 hPa, that

the hybrid bin run began to experience higher snow fall speeds compared to the control simulations. Note that the unrealistically low level at which ice was predicted in Geresdi likely indicates a potential bug in the bin scheme that needs to be addressed (not shown). The slower fall speeds early in the simulation likely were responsible for the hybrid simulation developing a larger anvil.

b) 3D real runs

In this section, the influence of the probability matching technique in the Thompson scheme is evaluated for a total of four 3D real cases consisting of two TS and LS systems. The focus will be on objective verification in addition to a qualitative evaluation of the differences between the control and hybrid simulations.

1) ETS AND BIAS

Overall, rainfall forecasts improved in the hybrid Thompson simulations; however, differences between individual cases were substantial. Figs. 20 and 21 illustrate the ETS and bias for each of the four cases. For the 09-10 June 2003 case, only the lightest (0.01"; 1" = 25.4 mm) and heaviest rainfall threshold (1") were improved with the fall speed modifications. No improvements were seen in the 30-31 May 2003 case; however, an improved rainfall forecast for every threshold (0.01, 0.1, 0.25, 0.5, 0.75 and 1") was seen in the 12-13 June 2002 case. The first and last three thresholds improved in the 19 June 2002 case.

Biases increased and signaled an improved forecast for the highest rainfall threshold in all four cases. Excluding the lightest and heaviest rainfall thresholds, the remaining four

thresholds showed a worsened forecast as biases decreased. A decrease in Bias in the first threshold in two cases represented an improvement in the rainfall forecast.

Averaged over all cases, ETS values increased for the lightest as well as the three heaviest rainfall thresholds in the hybrid runs (Table 2). Rainfall forecasts worsened for the middle three thresholds. Biases decreased for all but the highest rainfall threshold with an improved forecast for the lightest two thresholds and the heaviest threshold.

2) QUALITATIVE ANALYSIS

The fall speed modifications in the 3D real cases as well as in the 2D cases resulted in a larger anvil and a smaller stratiform rainfall region, changes reflected in the lower biases noted in the previous section. Fig. 22 illustrates the total observed rainfall on 19 June 2002 ending at 15 UTC and forecasted by the control and hybrid runs. Clearly, both model simulations did poor in predicting nearly 3" of rain in southeastern South Dakota where no rainfall was observed. However, the hybrid run did better in predicting the location and intensity of the 3" rainfall amount in northeastern Iowa although it underestimated peak amounts by 1". This underestimate is less severe than in the control run which had separate areas of rainfall of generally less than 1.5". Outside the small-scale heavy rain areas, rain amounts were lower in the hybrid run, and as such, helped improve the forecast in northwestern Iowa by removing rainfall in that area. Similar features of reduced stratiform rainfall and a better prediction of the most intense rainfall were noticed in two other cases, while minor differences in rainfall patterns between the control and hybrid runs were noticed in the 30-31 May 2003 case (not shown).

Finally, to show how the anvil in the hybrid simulation differed from the control, the incoming shortwave radiation at the surface was plotted for both model runs at 15 UTC 19 June 2002 and compared to a visible satellite image valid at 15:15 UTC (Fig. 23). The larger anvil forecasted in the hybrid run appeared to be similar in extent to that observed with the dense overcast extending several hundred miles east of Iowa, whereas the control run kept the deepest clouds confined primarily to Iowa.

The improvement in the forecast of the heaviest rainfall in the 19 June 2002 case in the hybrid was also a feature noted in the 2D hybrid Weisman simulation (Figs. 2a, b). Additionally in the 19 June 2002 run, graupel fall speeds were nearly 3 m s^{-1} faster (approaching 10.5 m s^{-1}) in the hybrid run near the melting level and in the vicinity of intense convection, but were slower than the control run in the stratiform region. As in the 2D runs, the faster falling graupel in the 3D hybrid Thompson simulations in the convective regions likely resulted in more intense convective rainfall, and is the result of an intrinsic nature of the Geresdi scheme graupel fall speed distribution.

4. Summary and Conclusions

While bin microphysical schemes are thought to have an advantage over bulk microphysical schemes in better representing certain processes such as sedimentation, they are far from being used operationally due to their computational expense. In this study fall speed distributions of cloud ice, snow and graupel were extracted from the Geresdi bin scheme using a probability matching technique, and were fed into the Thompson bulk scheme in order to test the

sensitivity of such fall speed modifications to the structure of TS and LS systems and to evaluate the impacts on QPF skill.

In the 2D simulations the fall speed modifications in the hybrid Thompson simulations resulted in slower falling snow, and this resulted in a narrower stratiform region, lighter stratiform surface rainfall and fewer grid points with rain due to reduced downward snow fluxes. In one idealized simulation, the increase in graupel fall speeds in the convective region resulted in a discernible increase in convective rainfall intensity. The slower falling snow remained suspended in the cloud longer and resulted in a larger anvil in all simulations. Minor differences in the microphysical processes were noted between the control and hybrid simulations; however, more substantial differences in the microphysical processes were seen between the TS and LS systems and most notably with the horizontal advection of water vapor. A reduction in water vapor by horizontal advection in the TS system was caused by the rear-inflow jet bringing drier air into the system. In the LS system, water vapor increases in the stratiform region associated with the overturning updraft as well as moisture convergence near the surface were negated by drier air moving in at mid-levels to the front of the system underneath cooling and moistening that had occurred from snow and ice sublimation. In the hybrid Thompson simulation, the weaker stratiform region produced less cooling, moistening and precipitation drag, which led to slightly stronger upward motions and a slight increase in water vapor through horizontal advection.

A sensitivity test whereby the Geresdi bin fall speeds were replaced with mass-weighted fall speeds resulted in the hybrid Geresdi simulation attaining faster snow and graupel fall speeds compared to the control simulations, increasing the downward fluxes of ice particles

near the melting level and resulting in a wider stratiform region of both TS and LS systems. The large fall speeds were attributed to the evolution of the snow size distribution, with larger, faster falling particles eventually being simulated.

For the 3D real hybrid Thompson simulations of TS and LS systems, QPF skill improved overall with improvements in the lightest and heaviest rainfall. Biases generally decreased for most rainfall thresholds and reflected what was observed in the 2D simulations, namely the presence of a weaker stratiform region and a larger anvil resulting from slower falling snow. The larger anvil in the hybrid run presented in one case was an improvement over the control run, comparing better to visible satellite imagery.

The probability matching technique provided a means of incorporating detailed bin scheme information into a bulk scheme that improved some aspects of simulated warm-season TS and LS systems. Future work should evaluate this technique more rigorously for many more cases and perhaps for different seasons.

Acknowledgements

The authors would like to thank Moti Segal, Brad Ferrier and Greg Thompson for their input. This research was funded by NSF Grants ATM-0848200 and ATM-0537043.

References

Aligo, E.A., W.A. Gallus, Jr., and M. Segal, 2007: Summer rainfall forecast spread in an ensemble initialized with different soil moisture analyses. *Wea. Forecasting,* **22,** 299-314.

Baldwin, M. E., and K. E. Mitchell, 1997: The NCEP hourly multi-sensor U.S. precipitation analysis for operations and GCIP research. Preprints, *13th AMS Conference on Hydrology*, Long Beach, CA, 54-55.

Betts, A.K., 1986: A new convective adjustment scheme. Part I: Observational and theoretical basis. *Quart. J. Roy. Meteor. Soc.*, **112,** 677-692.

____, and M.J. Miller, 1986: A new convective adjustment scheme. Part II: Single column tests using GATE wave, BOMEX, ATEX and arctic air-mass data sets. *Quart. J. Roy. Meteor. Soc.*, **112,** 693-709.

Braun, S. A., and R. A. Houze Jr., 1994: The transition zone and secondary maximum of radar reflectivity behind a midlatitude squall line: Results retrieved from Doppler radar data. *J. Atmos. Sci.*, **51,** 2733-2755.

Churchill, D. D. and R. A. Houze, Jr., 1984: Development and structure of winter monsoon cloud clusters on 10 December 1978. *J. Atmos. Sci.*, **41**, 933-960.

Colle, B. A., and C. F. Mass, 2000: The 5-9 February 1996 flooding event over the Pacific Northwest: Sensitivity studies and evaluation of the MM5 precipitation forecasts. *Mon. Wea. Rev.*, **128,** 593-617.

_____, M. F. Garvert, J. B. Wolfe, C. F. Mass and C. P. Woods, 2005: The 13-14 December 2001 IMPROVE-2 event. Part III: Simulated microphysical budgets and sensitivity studies. *J. Atmos. Sci.*, **62,** 3535-3558.

Cotton, W. R., G. J. Tripoli, R. M. Rauber, and E. A. Mulvihill, 1986: Numerical simulation of the effects of varying ice crystal nucleation rates and aggregation processes on orographic snowfall. *J. Climate Appl. Meteor*., **25**, 1658-1680.

Davis, C., and Coauthors, 2004: The bow echo and MCV experiment: observations and opportunities. *Bull. Amer. Meteor. Soc*., **85,** 1075-1093.

Doswell III, C. A., H. E. Brooks, and R. A. Maddox, 1996: Flash flood forecasting: An ingredients-based methodology. *Wea. Forecasting*, **11**, 560-581.

Ek, M. B., K.E. Mitchell, Y. Lin, E. Rogers, P. Grunmann, V. Koren, G. Gayno, and J.D. Tarplay, 2003: Implementation of Noah land surface model advances in the National Centers for Environmental Prediction operational mesoscale Eta model. *J. Geophys. Res.*, **108,** 8851, doi:10.1029/2002JD003296.

Ferrier, B. S., 1994: A double-moment multiple-phase four-class bulk ice scheme. Part I: Description. *J. Atmos. Sci.*, **51,** 249-280.

Fritsch, J. M., R. J. Kane, and C. R. Chelius, 1986: The contribution of mesoscale convective weather systems to the warm-season precipitation in the United States. *J. Climate Appl. Meteor.*, **25**, 1333-1345.

_____, and R. E. Carbone, 2004: Improving quantitative precipitation forecasts in the warm season: A USWRP research and development strategy. *Bull. Amer. Meteor. Soc.,* **85,** 955-965.

Gallus, W. A. Jr., and R. H. Johnson, 1995: The dynamics of circulations within the trailing stratiform regions of squall lines. Part I: The 10-11 June PRE-STORM system. *J. Atmos. Sci.*, **52,** 2161-2187.

_____, and M. Pfeifer, 2008: Intercomparision of simulations using 5 WRF microphysical schemes with dual-Polarization data for a German squall line. *Advances in Geosciences,* **16**, 109-116.

_____, N. A. Snook, E. V. Johnson, 2008: Spring and summer severe weather reports over the Midwest as a funciton of convective mode: A preliminary study. *Wea. Forecasting,* **23**, 101-113.

Geresdi, I., 1998: Idealized simulation of the Colorado hailstorm case: comparison of bulk and detailed microphysics. *Atmospheric Research,* **45**, 237-252.

Gilmore, M. S., J. M. Straka, and E. N. Rasmussen, 2004b: Precipitation uncertainty due to variations in precipitation particle parameters within a simple microphysics scheme. *Mon. Wea. Rev.,* **132,** 2610-2627.

Hong, S.-Y. and J. –O. Lim, 2006: The WRF single-moment 6-class microphysics scheme (WSM6). *Journal of the Korean Meteorological Society,* **42,** 129-151.

Houze, R. A., Jr., 1982: Cloud clusters and large-scale vertical motions in the tropics, 1982. *J. Meteorol. Soc. Japan,* **60**, 396-409.

_____, 1993: *Cloud Dynamics.* Academic Press, 605pp.

Janjic, Z.I., 2002: Nonsingular implantation of the Mellor-Yamada level 2.5 scheme in the NCEP meso model. NOAA/NWS/NCEP Office Note #437, 61 pp.

_____, 1994: The step-mountain Eta coordinate model: Further developments of the convection closure schemes. *Mon. Wea. Rev*., **122,** 927-945.

Jankov, I., W.A. Gallus Jr., M. Segal, B. Shaw and S. E. Koch, 2005: The impact of different WRF model physical parameterizations and their interactions on warm season MCS rainfall. *Wea. Forecasting,* **20**, 1048-1060.

Kain, J. S., and J. M. Fritsch, 1990: A one-dimensional entraining/detraining plume model and its application in convective parameterization. *J. Atmos. Sci.*, **47,** 2784-280.

Knupp, K.R., and W. R. Cotton, 1987: Internal structure of a small mesoscale convective system. *Mon. Wea. Rev.,* **115**, 629-645.

Lin, Y. –L., R. D. Farley and H. D. Orville, 1983: Bulk parameterization of the snow field in a cloud model. *J. Appl. Meteor.,* **22,** 1065-1092.

Lynn, B. H., A. P. Khain, J. Dudhia, D. Rosenfeld, A. Pokrovsky and A. Seifert, 2005: Spectral (Bin) microphysics coupled with a mesoscale model (MM5). Part II: Simulation of a CaPE rain event with a squall line. *Mon.Wea.Rev.*, **133,** 59-71.

_____ and _____, 2007: Utilization of spectral bin microphysics and bulk parameterization schemes to simulate the cloud structure and precipitation in a mesoscale rain event. *J. Geophys. Res.*, **112,** 22205, doi:10.1029/2007JD008475.

Marshall, J.S. and W. Mc K. Palmer, 1948: The distribution of raindrops with size. *J. Meteor*., **5,** 165-166.

Mass, C.F., D. Ovens, K. Westrick, and B.A. Colle, 2002: Does increasing horizontal resolution produce better forecasts? The results of two years of real-time numerical weather prediction over the Pacific Northwest. *Bull. Amer. Meteor*. Soc., **82,** 407-430.

McCumber, M., W-K. Tao, J. Simpson, R. Penc, and S-T Soong, 1991: Comparison of ice-phase microphysical parameterization schemes using numerical simulations of tropical convection. *J. Appl. Meteor.,* **30,** 985-1004.

Milbrandt, J.A., and M. K. Yau, 2005a: A multimoment bulk microphysics parameterization. Part I: Analysis of the role of the spectral shape parameter. *J. Atmos. Sci.*, **62,** 3051-3064.

Morrison, H, and A. Gettelman, 2008: A new two-moment bulk stratiform cloud microphysics scheme in the Community Atmosphere Model Version 3 (CAM3). Part I: Description and numerical tests. *J. Climate*, **21,** 3660-3679.

_____, G. Thompson, and V. Tatarskii, 2009: Impact of cloud microphysics on the development of trailing stratiform precipitation in a simulated squall line: Comparison of one- and two-moment schemes. *Mon. Wea. Rev.,***128,** 991-1007.

Parker, M.D., and R. H. Johnson, 2000: Organizational modes of midlatitude mesoscale convective systems. *Mon. Wea. Rev.,***128,** 3413-3436.

_____, _____, 2004a: Structures and dynamics of quasi-2D mesoscale convective systems. *J. Atmos. Sci.*, **61,** 545-567.

_____, _____, 2004c: Simulated convective lines with leading precipitation. Part II: Evolution and maintenance. *J. Atmos. Sci.*, **61,** 1656-1673.

Parsons, D., cited 2002: IHOP_2002 Water Vapor Intercomparisons Workshop Presentations. [Available online at [http://www.atd.ucar.edu/dir_off/projects/2002/IHOPwsOct03 /presentations.html].

Potter, B. E., 1991: Improvements to a commonly used cloud microphysical bulk parameterization. *J. Appl. Meteor.,* **30,** 1040-1042.

Pruppacher, H. R., and J. D. Klett, 1978: *Microphysics of Clouds and Precipitation.* D. Reidel, 714 pp.

Rasmussen, R. M. and A. J. Heymsfield, 1987: Melting and shedding of graupel and hail. Part I: Model physics. *J. Atmos. Sci.*, **44,** 2754-2763.

_____, I. Geresdi, G. Thompson, K, Manning and E. Karplus, 2002: Freezing drizzle formation in stably stratified layer clouds: The role of radiative cooling of cloud droplets, cloud condensation nuclei, and ice initiation. *J. Atmos. Sci.*, **59,** 837-860.

Raymond, W. H., and R. M. Aune, 1998: Improved precipitation forecasts using parameterized precipitation drag in a hydrostatic forecast model. *Mon. Wea. Rev.,***135,** 693-710.

Rutledge, S. A., and R. A. Houze Jr., 1987: A diagnostic modeling study of the trailing stratiform region of a midlatitude squall line. *J. Atmos. Sci.*, **44,** 2640-2656.

Schaefer, J.T., 1990: The critical success index as an indicator of warning skill. *Wea. Forecasting*, **5,** 570-575.

Skamarock, W.C., J.B. Klemp, J. Dudhia, D.O. Gill, D.M. Barker, W. Wang, and J.G. Powers, 2005: A description of the advanced research WRF version 2. NCAR Tech. Note NCAR/TN-468+STR, 88 pp. [Available online at http://www.wrf-model.org/wrfadmin/docs/arw_v2.pdf]

Steiner, M., R. A. Houze Jr., and S. E. Yuter, 1995: Climatological characterization of three-dimensional storm structure from operational radar and rain gauge data. *J. Appl. Meteor.,* **34,** 1978-2007.

Storm, B.A., M. D. Parker, and D. P. Jorgensen, 2007: A convective line with leading stratiform precipitation from BAMEX. *Mon. Wea. Rev.,***135,** 1769-1785.

Thompson, G., P. R. Field, R. M. Rasmussen, and W. D. Hall 2008: Explicit forecasts of winter precipitation using an improved bulk microphysics scheme. Part II: Implementation of a new snow parameterization. *Mon. Wea. Rev.,* **136,** 5095-5115.

Walko, R. L., W. R. Cotton, M. P. Meyers, and J. Y. Harrington, 1995: New RAMS cloud microphysics parameterization. Part I: The single-moment scheme. *Atmos. Res.*, **38**, 29–62.

Verlinde, J., P. J. Flatau, and W. R. Cotton, 1990: Analytical solutions to the collection growth equation: Comparison with approximate methods and application to the cloud microphysics parameterization schemes. *J. Atmos. Sci.*, **47**:2871–2880.

Weisman, M. L., J. B. Klemp, and R. Ruttunno, 1988: Structure and evolution of numerically simulated squall lines. *J. Atmos. Sci.,* **45**, 1990-2013

_____, W. C. Skamarock, and J. B. Klemp, 1997: The resolution dependence of explicitly modeled convective systems. *Mon. Wea. Rev.,* **136,** 527-548.

List of Figures

Figure 6. Cumulative frequency plots of graupel and snow fall speeds for a range of fall speeds for the Geresdi and Thompson simulations using the Weisman case.

Figure. 7. Vertical cross sections of (a),(b) graupel and (c),(d) snow fall speeds valid four hours into the Weisman case for the control (first column) and hybrid Thompson (second column) simulations. The grid points are depicted along the absicaa and units of the fall speeds are in m s^{-1}.

Figure. 8. Percentage contribution of microphysical processes to the total microphysical budget for the control and hybrid simulations as well as convective and stratiform regions for the (a) Weisman, (b) 12 June 2002 and (c) LS cases. The processes are defined as follows: SMLT: snow melting, GMLT: graupel melting, RCW: Rain collecting cloud water, RAUT: autoconversion of cloud water to rain water, RCG: rain collecting graupel, GRFZ: rain freezing to form graupel, IFZ: rain freezing to form ice, RCI: rain collecting ice, RCS: rain collecting snow, E: rain evaporation, HAD: horizontal advection of rain and VAD: vertical advection of rain. Stratiform region in the control (hybrid) simulations is depicted by the solid (hatched) blue color with the convective region in the control (hybrid) depicted by the solid (hatched) red colors.

Figure. 9. Same as in Fig. 8 but for snow. The processes are defined as follows: SDEP: snow deposition/sublimation, SCI: snow collecting ice, SCW: snow collecting water, SAUT: autoconversion of cloud ice to snow, RCS: rain collecting snow, IDEP: Ice deposition/sublimation, SMRS: ice

multiplication from rime-splinters, SMLT: snow melting, HAD: horizontal advection of snow and VAD: vertical advection of snow.

Figure. 10. Same as in Fig. 8, but for cloud water. The processes are defined as follows:
RAUT: autoconversion of cloud water to rain, CWF: cloud water freezing, RCW: rain collecting cloud water, SCW: snow collecting cloud water, RIME: rimed snow becoming graupel, GCW: graupel collecting cloud water, HAD: horizontal advection of cloud water and VAD: vertical advection of cloud water.

Figure. 11. Same as in Fig. 8, but for water vapor. The processes are defined as follows:
CNDF: condensation freezing, IDEP: ice deposition/sublimation, SIDEP: ice deposition/sublimation, SDEP: Snow deposition/sublimnation, GDEP: graupel deposition/sublimation, COND: cloud water condensation, E: rain evaporation, HAD: horizontal advection of water vapor and VAD: vertical advection of water vapor.

Figure 12. Vertical cross section of time-averaged (last five hours of simulation) u (east-west) winds (shaded) and five hour accuulated horizontal adection of water vapor for the Weisman case. Units of wind are m s^{-1} while units of the horizontal water vapor advection are kg kg^{-1} $10min^{-1}$.

Figure. 13. Vertical cross section of (a) control and (b) hybrid Thompson u (east-west) winds (shaded), and (e) control and (f) hybrid Thompson vertical velocities averaged from t=4h to t=5h. Also, accumluated from t=4h to t=5h is the (a) control and (b) hybrid Thompson advection of water vapor (contoured), and (c) control and (d) hybrid Thompson diabatic heating/cooling (shaded). Contour levels used in (a) and (b) are -1.5, -1, -0.5, -0.2, 0.2, 0.5, 1, 1.5. Units of advection are 10^{-3} kg kg^{-1} h^{-1} . The model grid points are depicted along the absicaa.

Figure. 14. Same as in Fig. 8, but for graupel. The processes are defined as follows:
FRZ: rain freezing, RCG: rain collecting graupel, GCW: graupel collecting cloud water, RCI: rain collecting ice, GCW: graupel collecting cloud water, RIME: rimed snow becoming graupel, GMRS: ice multiplication from rime-splinters, GMLT: graupel melting, HAD: horizontal advection of graupel and VAD: vertical advection of graupel.

Figure. 15. Hovmöller diagrams of surface rainfall for the control (first column) and hybrid (second column) idealized Geresdi simulations using the (a),(b) Weisman, (c),(d) 12 June 2002 and (e),(f) LS soundings with the absicaa indicating the model grid points and rainfall in inches (1 inch = 25.4 mm).

Figure 16. Hövmuller diagrams of simulated radar reflectivity for the (a),(c) control and (b),(d) hybrid LS idealized Geresdi simulations with the absicaa indicating the model grid points. Units are dBZ.

Figure 17. Vertical cross sections of snow fall speeds at hour three of the (a) control and (b) hybrid Geresdi simulations for the Weisman case. The grid points are depicted along the absicaa and units of the fall speeds are in m s^{-1}.

Figure 18. Cumulative frequency diagram snow fall speeds from the Geresdi control and hybrid simulations for the Weisman case.

Figure 19. Size distribution functions of snow for the Geresdi control and hybrid simulations for the Weisman case.

Figure 20. ETS values for the (a) 09-10 June 2003, (b) 12-13 June 2002, (c) 30-31 May 2003 and (d) 19 June 2002 cases for the indicated rainfall thresholds and for the control and hybrid Thompson runs.

Figure 21. Bias values for the (a) 09-10 June 2003, (b) 12-13 June 2002, (c) 30-31 May 2003 and (d) 19 June 2002 cases for the indicated rainfall thresholds and for the control and hybrid Thompson runs.

Figure 22. The 15-h accumulated rainfall (inches) ending at 15 UTC 19 June 2002 from (a) observations, (b) the control run and (c) the hybrid Thompson run.

Figure 23. The (a) visible satellite image valid at 15:15 UTC 19 June 2002 as well as the 15-h forecasted incoming surface shortwave radiation (W m^{-2}) valid at 15 UTC 19 June 2002 for the (b) control and (b) hybrid Thompson runs.

List of Tables

Appendix

Thompson Microphysical Tendency Equations

Note that q_v,q_c,q_r,q_s and q_g below are the mixing ratios of water vapor, cloud water, rain water, snow and graupel, respectively. See Table 1 for a definition of all of the source/sink terms indicated below.

$$dq_v/dt = (-pri\_inu - pri\_ide - prs\_ide - prs\_sde - prg\_gde - prw\_vcd + prv\_rev),$$

$$dq_c/dt = (-prr\_wau - pri\_wfz - prr\_rcw - prs\_scw - prg\_scw - prg\_gcw + prw\_vcd),$$

$$dq_i/dt = (+pri\_inu + pri\_ihm + pri\_wfz + pri\_rfz + pri\_ide - prs\_iau - prs\_sci - pri\_rci + sed\_i),$$

$$dq_r/dt = (+prr\_wau + prr\_rcw + prr\_sml + prr\_gml + prr\_rcs + prr\_rcg - prg\_rfz - pri\_rfz - prr\_rci - prv\_rev + sed\_r),$$

$$dq_s/dt = (+prs\_iau + prs\_sde + prs\_sci + prs\_scw + prs\_rcs + prs\_ide - prs\_ihm - prr\_sml - sed\_s),$$

$$dq_g/dt = (+prg\_scw + prg\_rfz + prg\_gde + prg\_rcg + prg\_gcw + prg\_rci + prg\_rcs - prg\_ihm - prr\_gml + sed\_g),$$

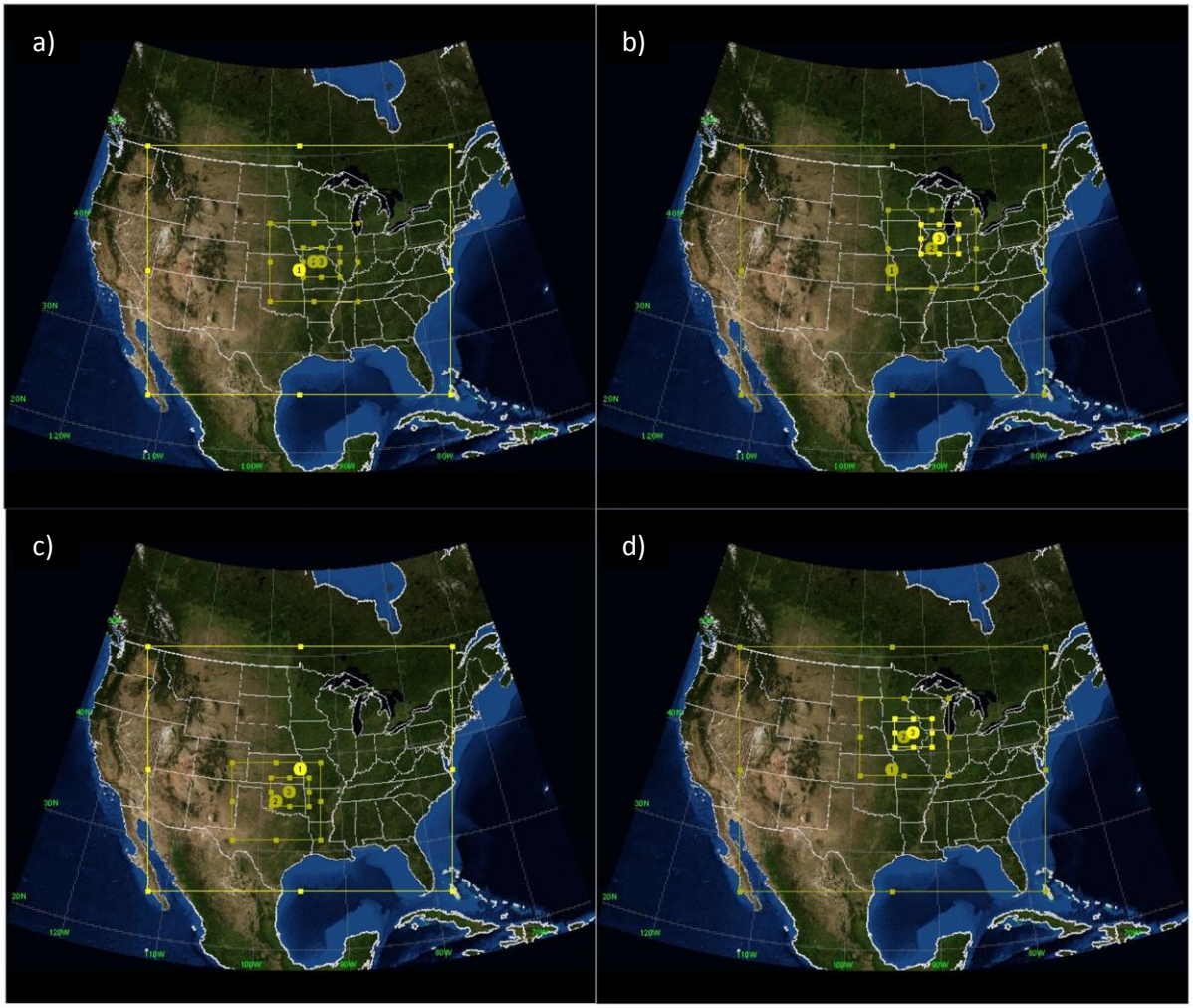

Fig. 1. Depiction of the 9 km outer nest, 3 km intermediate nest as well as the 1 km inner nest for the (a) 09-10 June 2003, (b) 30-31 May 2003, (c) 12-13 June 2002 and (d) 19 June 2002 model runs.

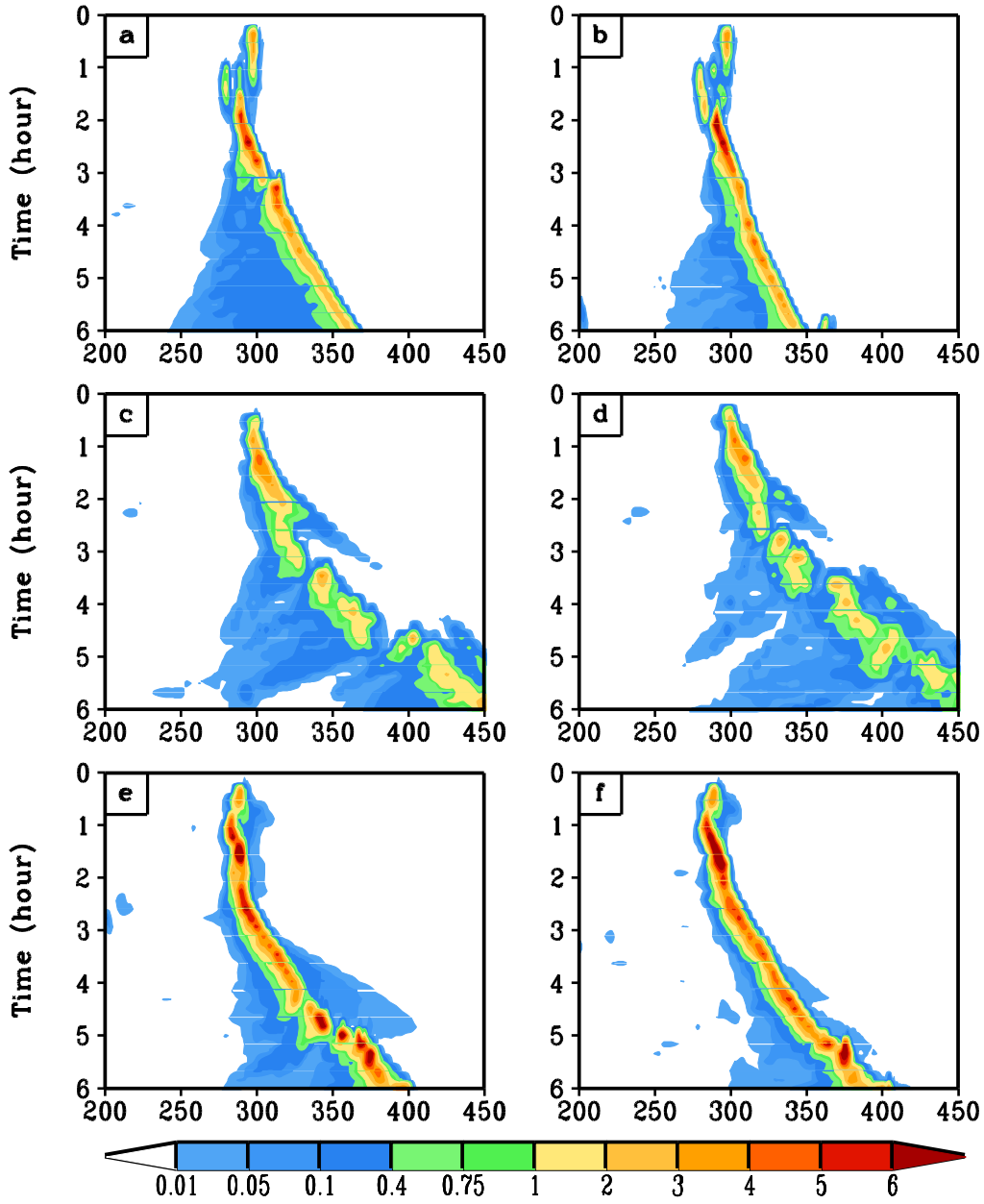

Fig. 2. Hovmöller diagrams of surface rainfall from the control (first column) and hybrid (second column) idealized simulations using the (a),(b) Weisman, (c),(d) 12 June 2002 and (e),(f) LS soundings with the abscissa indicating the model grid points and rainfall in inches (1 inch = 25.4 mm).

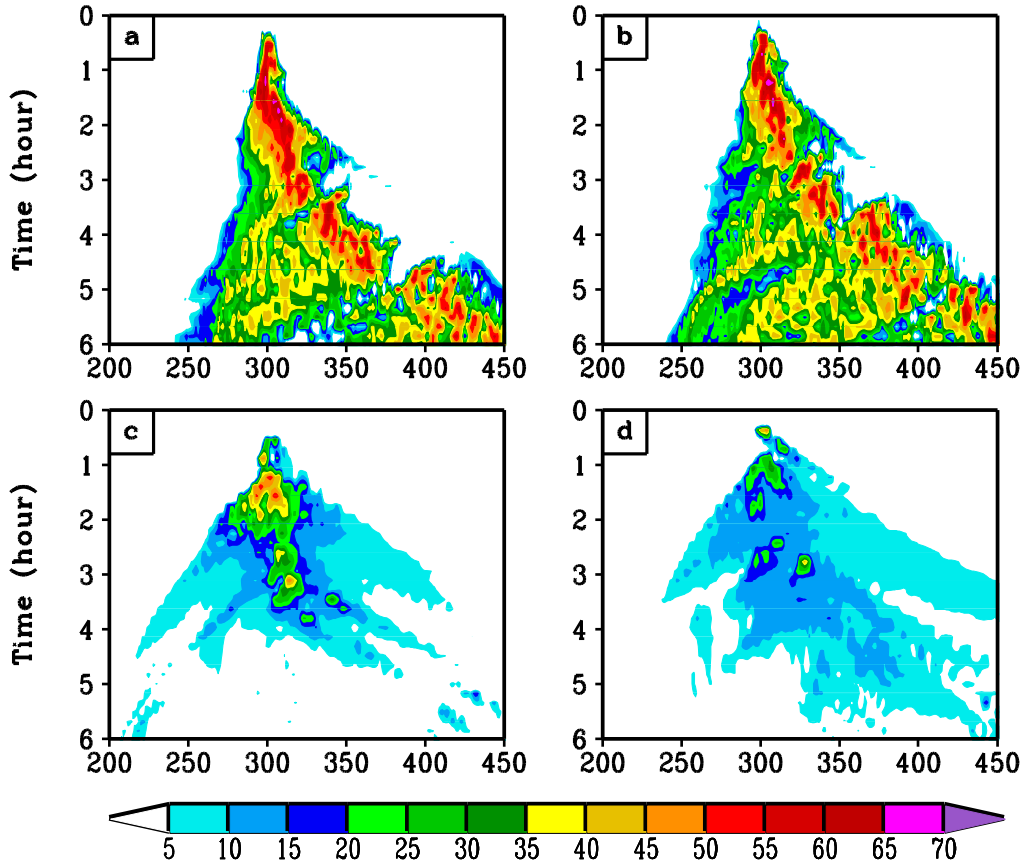

Fig. 3. Hovmöller diagrams of simulated radar reflectivity for the (a),(c) control and (b),(d) hybrid 12 June 2002 idealized Geresdi simulations near the melting level (575 hPa) (a),(b) and in the anvil (250 hPa) (c),(d) with the abscissa indicating the model grid points. Units are dBZ.

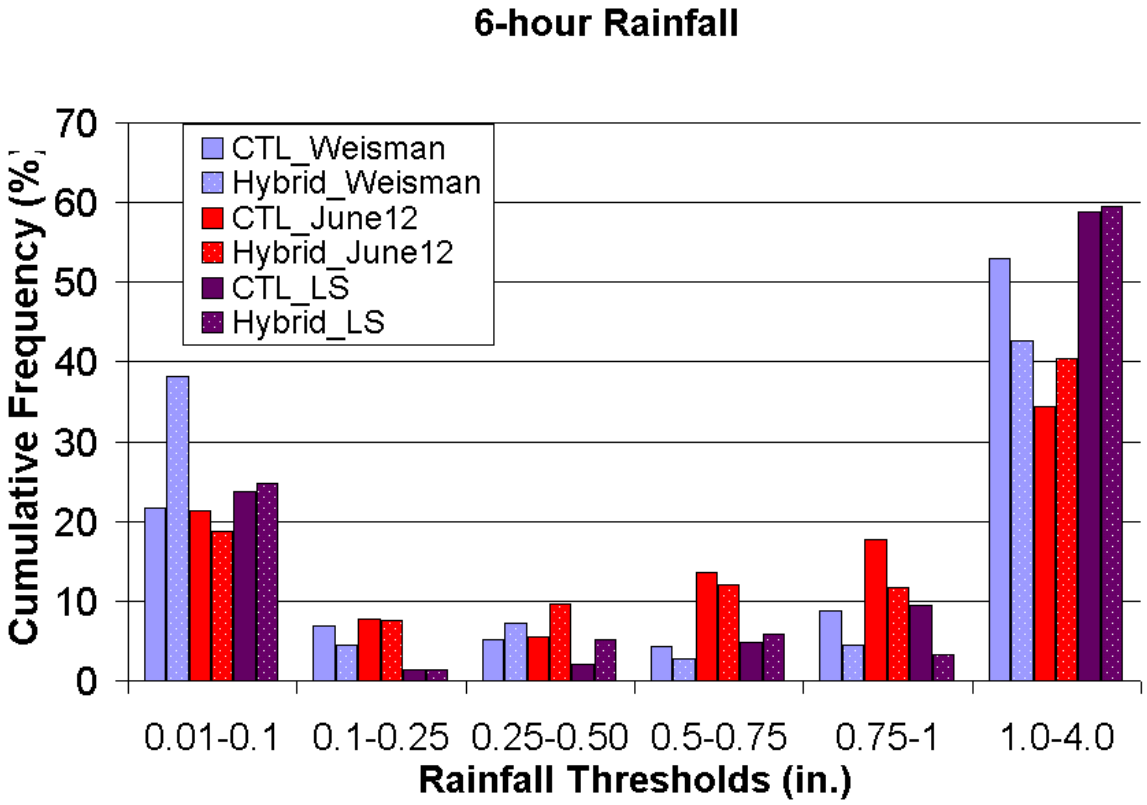

Fig. 4. Cumulative frequency plot of accumulated 6-hour rainfall for the control and hybrid simulations of the three idealized cases for various rainfall thresholds. Units are in inches (1 inch = 25.4 mm). The blue solid (hatched) color represents the Weisman control (hybrid) simulation, the red solid (hatched) represents the the 12 June 2002 control (hybrid) simulation and the purple solid (hatched) color represents the LS control (hybrid) simulation.

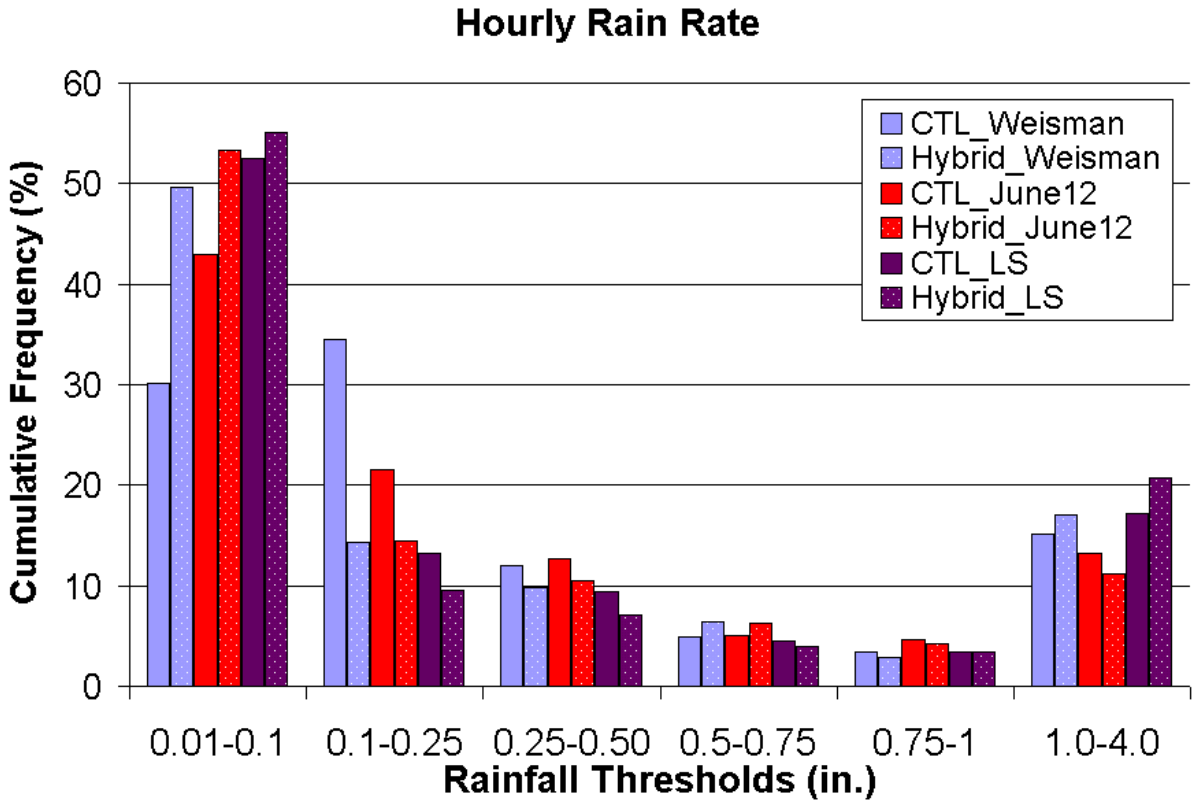

Fig. 5. Cumulative frequency plot of hourly rain rate obtained from the ten-minute available output for the control and hybrid simulations of the three idealized cases for various rainfall thresholds. Units are in inches (1 inch = 25.4 mm). The blue solid (hatched) color represents the Weisman control (hybrid) simulation, the red solid (hatched) represents the the 12 June 2002 control (hybrid) simulation and the purple solid (hatched) color represents the LS control (hybrid) simulation.

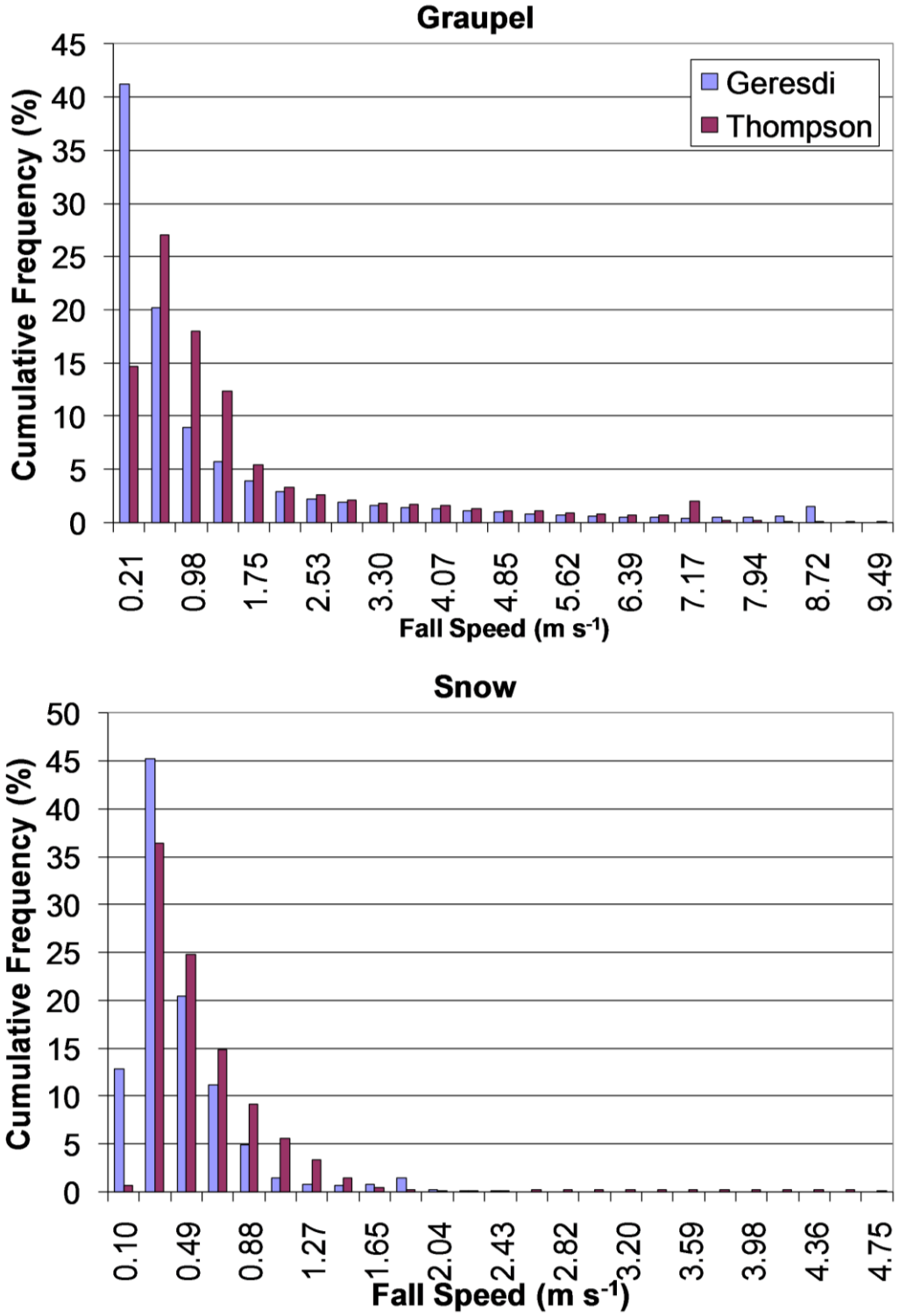

Fig. 6. Cumulative frequency plots of graupel and snow fall speeds for a range of fall speeds for the Geresdi and Thompson simulations using the Weisman case.

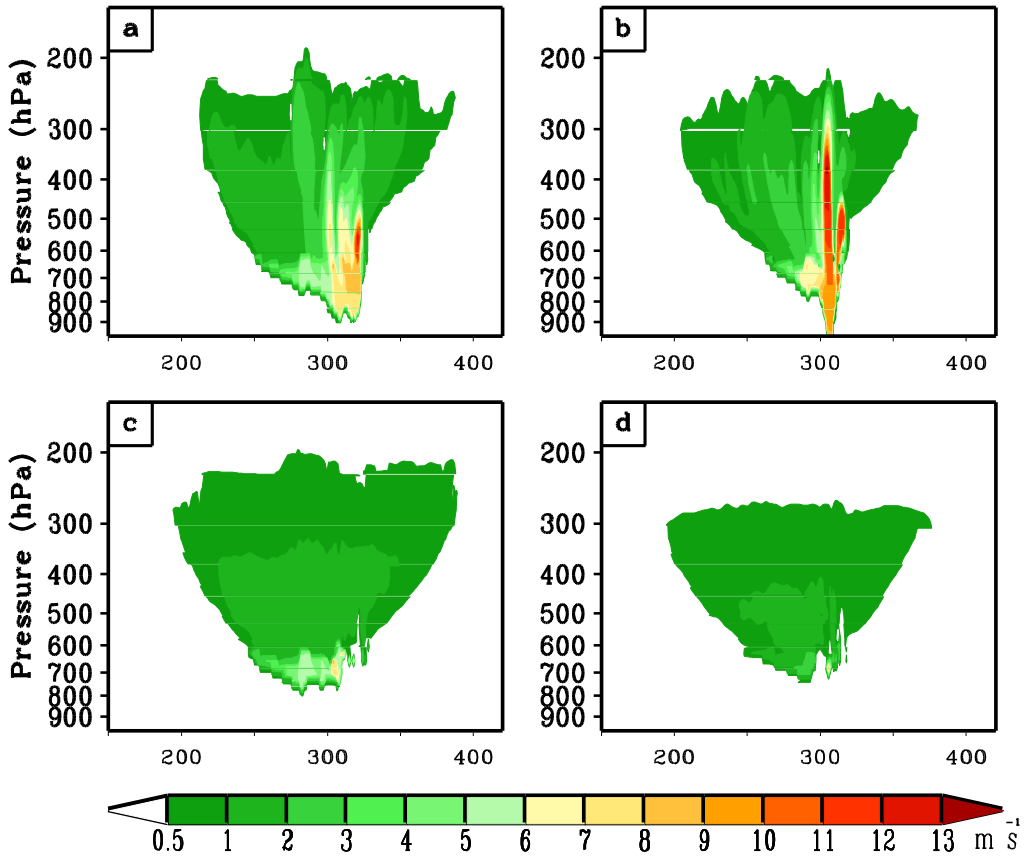

Fig. 7. Vertical cross sections of (a),(b) graupel and (c),(d) snow fall speeds valid four hours into the Weisman case for the control (first column) and hybrid Thompson (second column) simulations. The grid points are depicted along the absicaa and units of the fall speeds are in m s^{-1}.

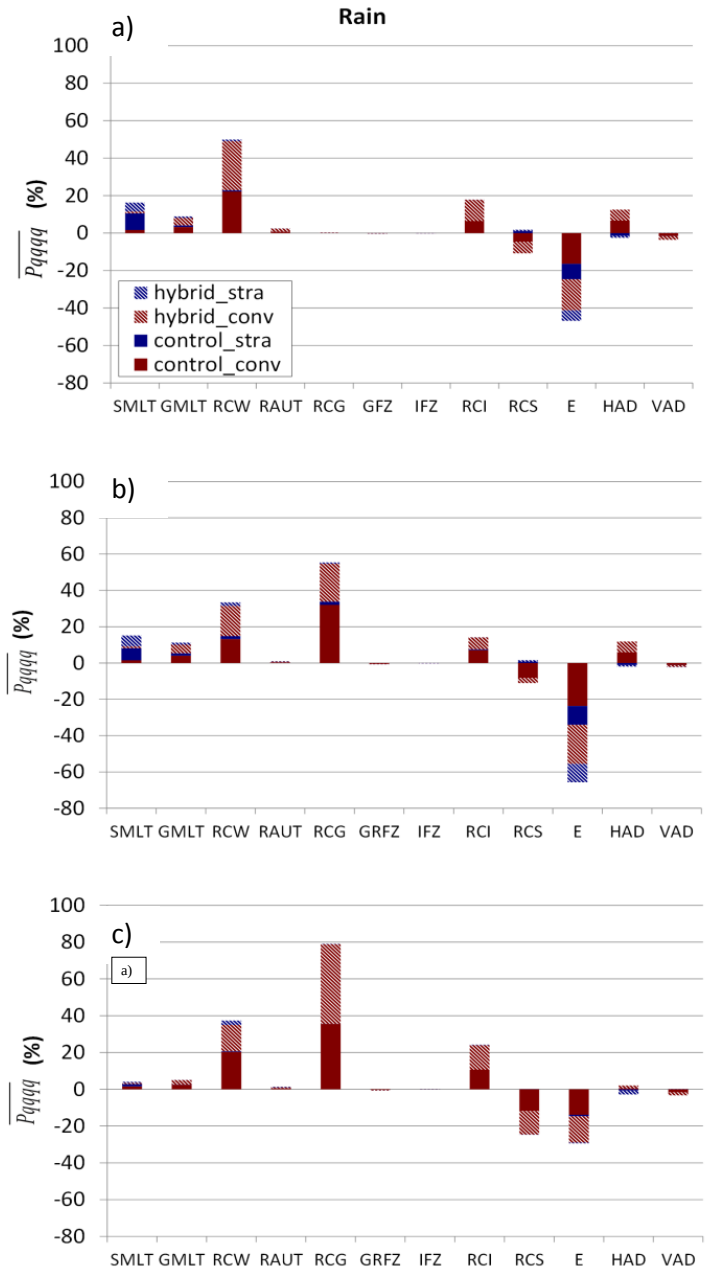

Fig. 8. Percentage contribution of microphysical processes to the total microphysical budget for the control and hybrid simulations as well as convective and stratiform regions for the (a) Weisman, (b) 12 June 2002 and (c) LS cases. The processes are defined as follows: SMLT: snow melting, GMLT: graupel melting, RCW: Rain collecting cloud water, RAUT: autoconversion of cloud water to rain water, RCG: rain collecting graupel, GRFZ: rain freezing to form graupel, IFZ: rain freezing to form ice, RCI: rain collecting ice, RCS: rain collecting snow, E: rain evaporation, HAD: horizontal advection of rain and VAD: vertical advection of rain. Stratiform region in the control (hybrid) simulations is depicted by the solid (hatched) blue color with the convective region in the control (hybrid) depicted by the solid (hatched) red colors.

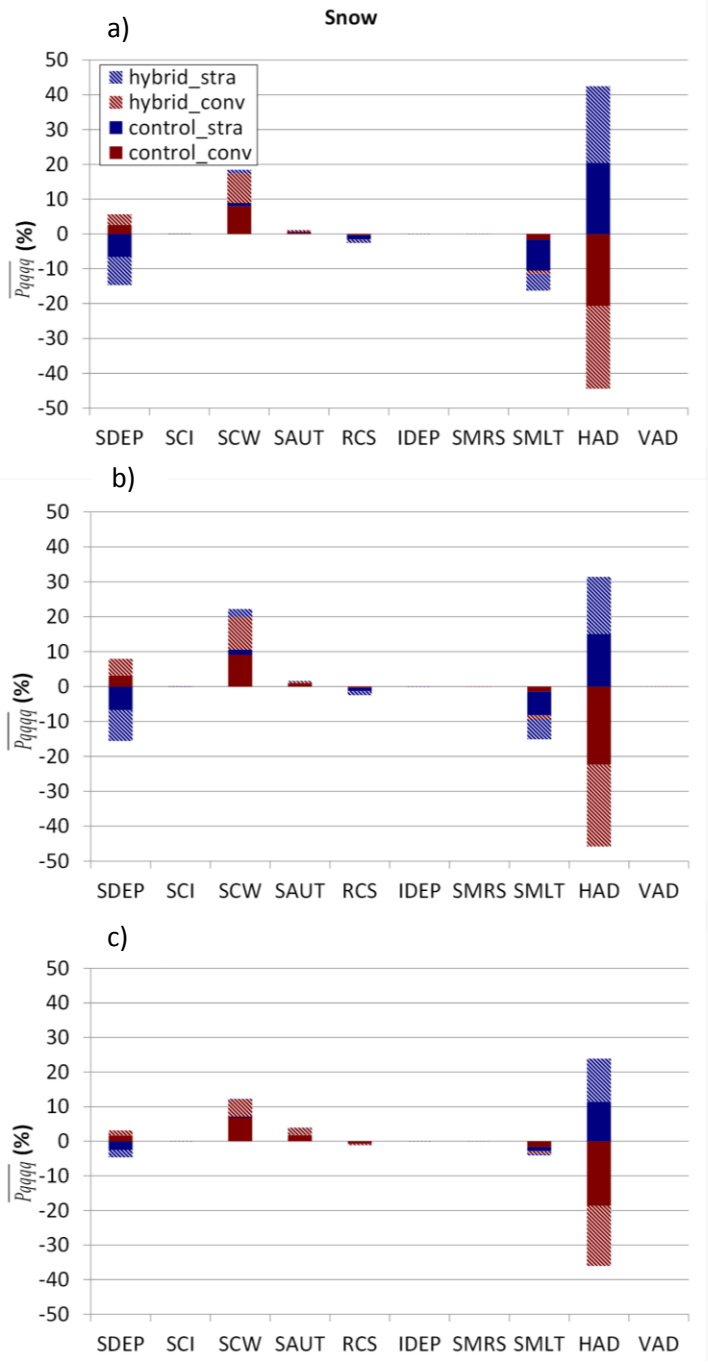

Fig. 9. Same as in Fig. 8 but for snow. The processes are defined as follows: SDEP: snow deposition/sublimation, SCI: snow collecting ice, SCW: snow collecting water, SAUT: autoconversion of cloud ice to snow, RCS: rain collecting snow, IDEP: Ice deposition/sublimation, SMRS: ice multiplication from rime-splinters, SMLT: snow melting, HAD: horizontal advection of snow and VAD: vertical advection of snow.

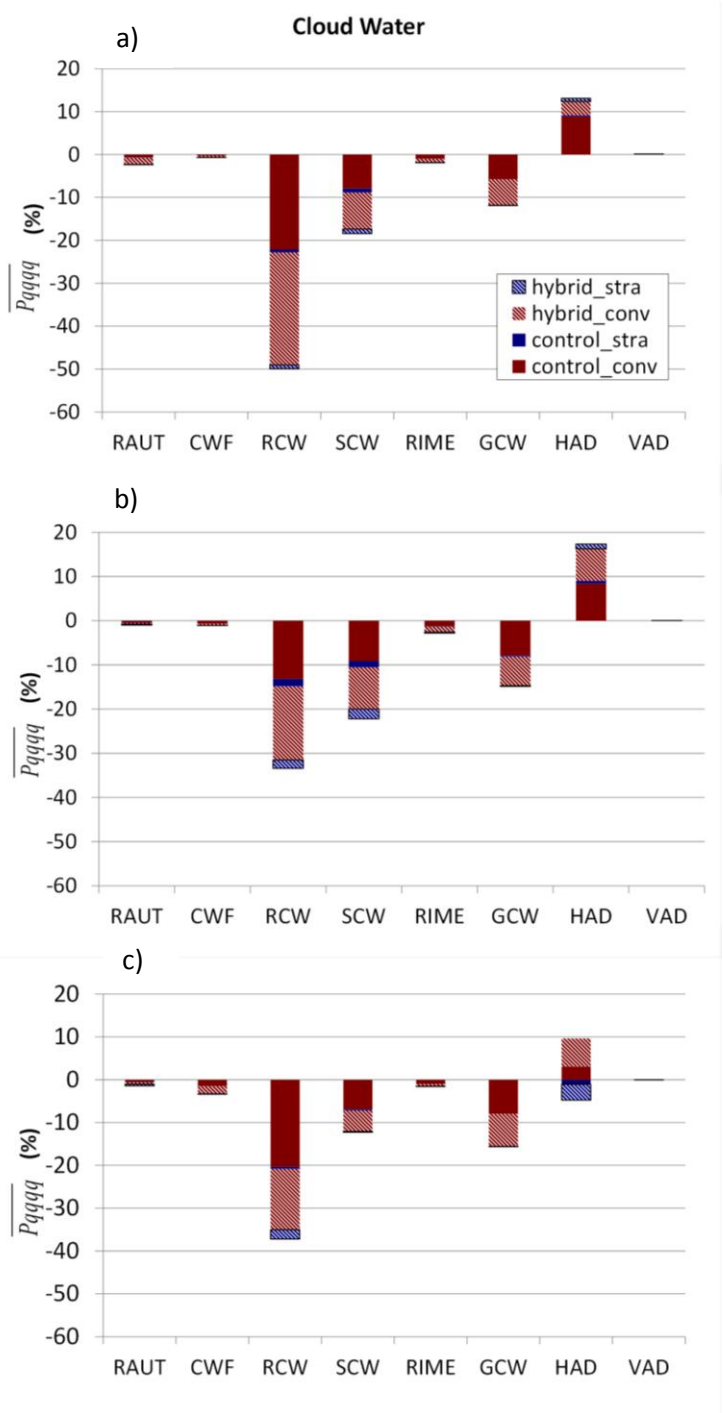

Fig. 10. Same as in Fig. 8, but for cloud water. The processes are defined as follows:
RAUT: autoconversion of cloud water to rain, CWF: cloud water freezing, RCW: rain collecting cloud water, SCW: snow collecting cloud water, RIME: rimed snow becoming graupel, GCW: graupel collecting cloud water, HAD: horizontal advection of cloud water and VAD: vertical advection of cloud water.

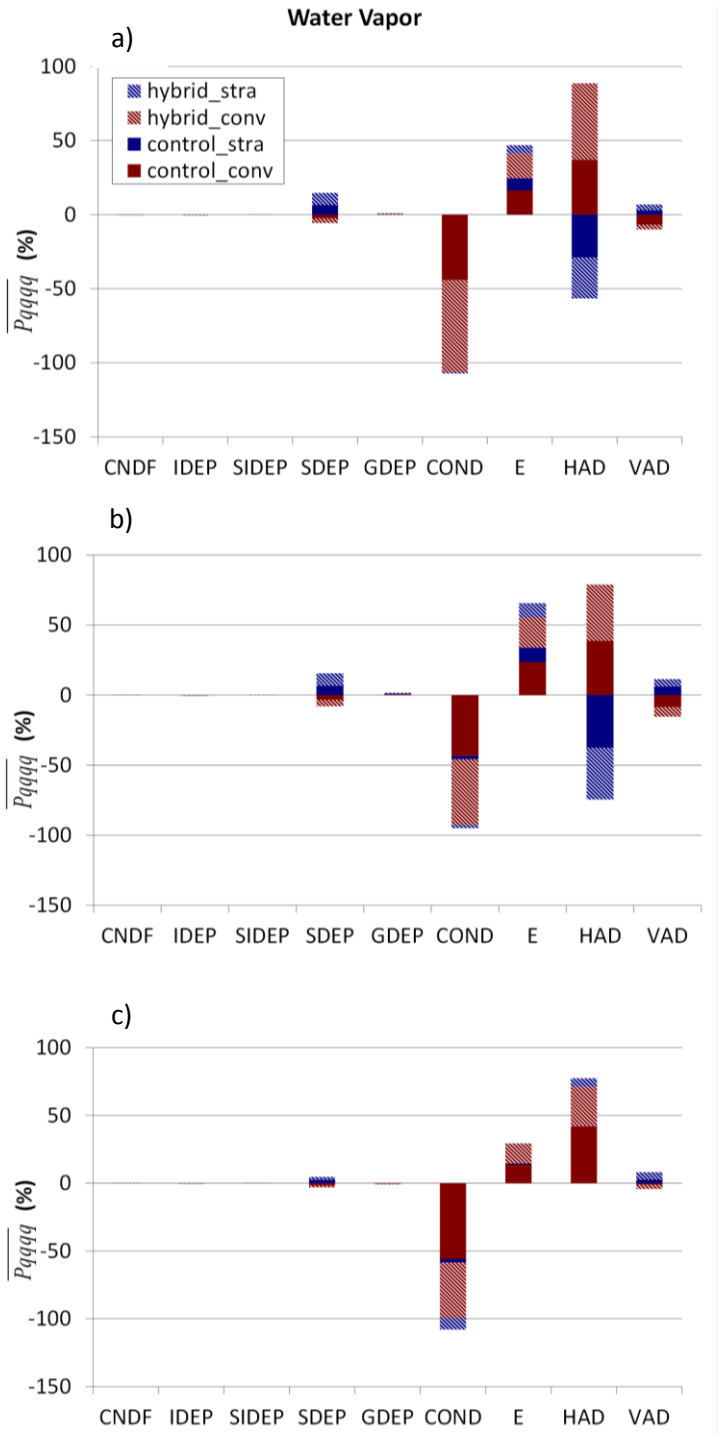

Fig. 11. Same as in Fig. 8, but for water vapor. The processes are defined as follows:
CNDF: condensation freezing, IDEP: ice deposition/sublimation, SIDEP: ice deposition/sublimation, SDEP: Snow deposition/sublimnation, GDEP: graupel deposition/sublimation, COND: cloud water condensation, E: rain evaporation, HAD: horizontal advection of water vapor and VAD: vertical advection of water vapor.

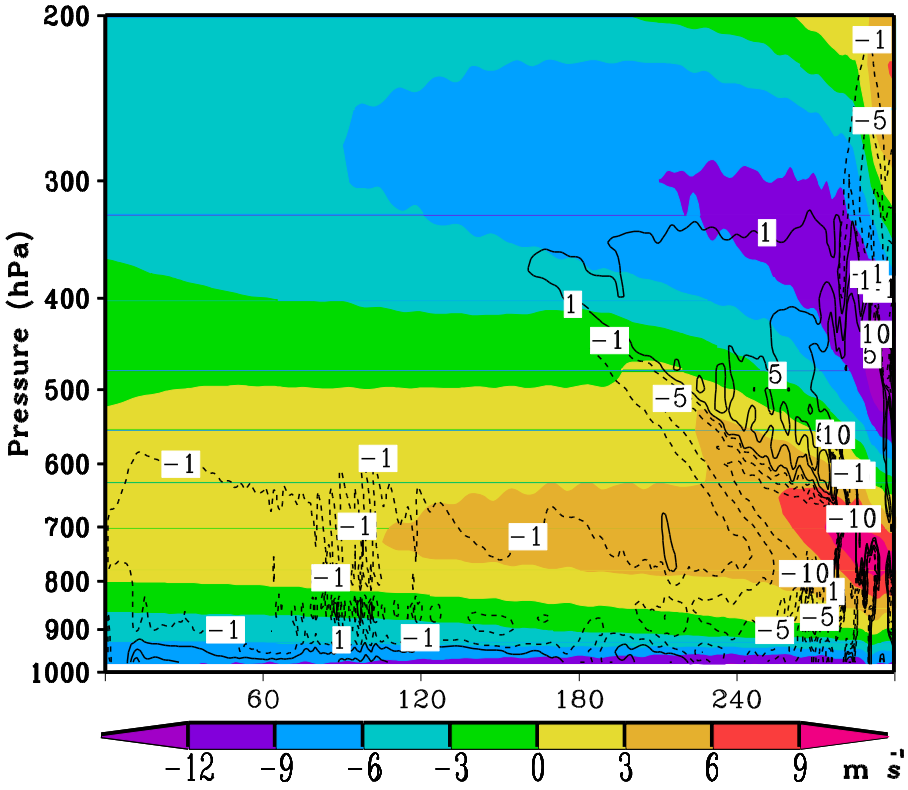

Fig. 12. Vertical cross section of time-averaged (last five hours of simulation) u (east-west) winds (shaded) and five hour accuulated horizontal adection of water vapor for the Weisman case. Units of wind are m s^{-1} while units of the horizontal water vapor advection are kg kg^{-1} $6h^{-1}$.

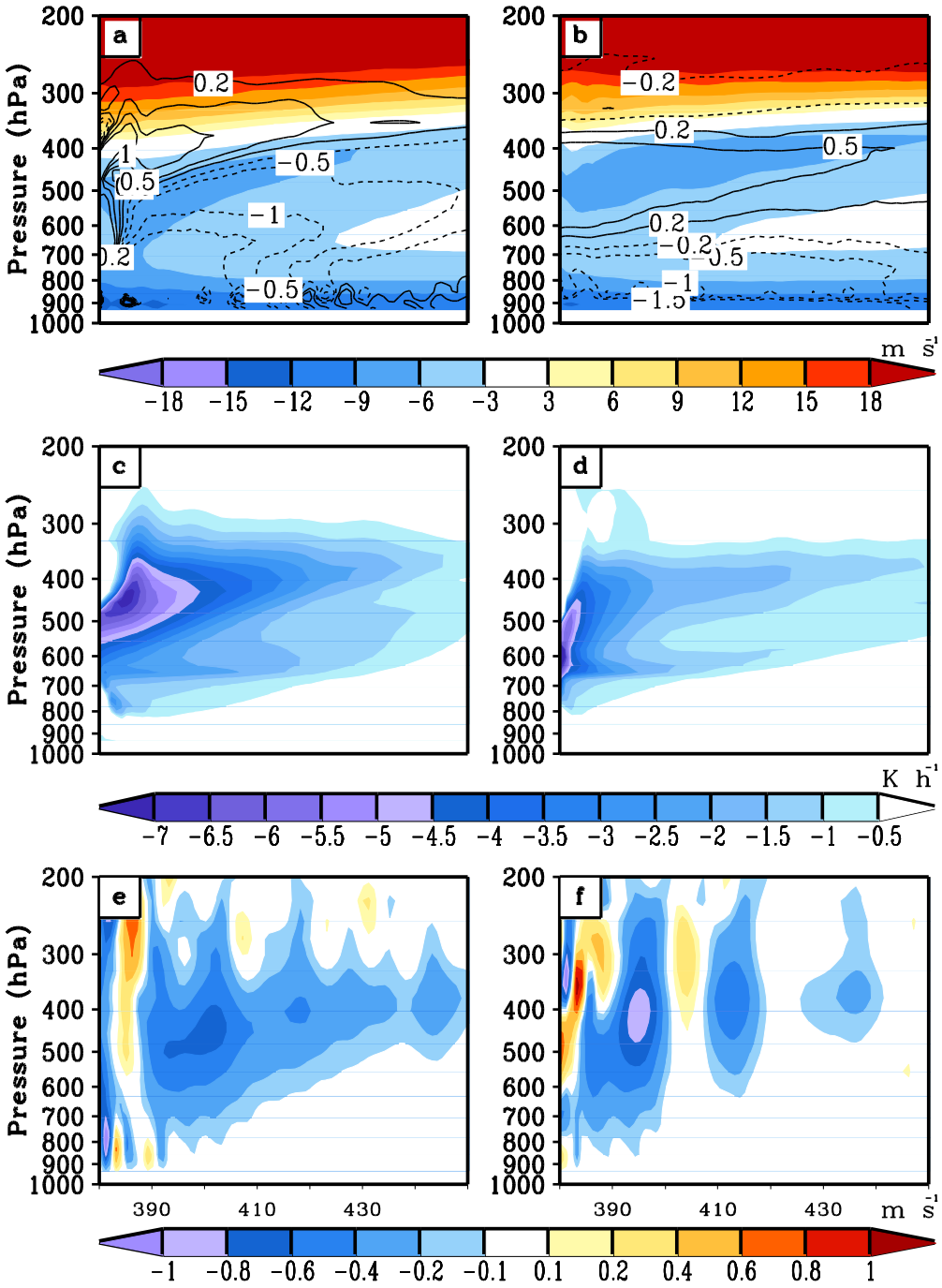

Fig. 13. Vertical cross section of (a) control and (b) hybrid Thompson u (east-west) winds (shaded), and (e) control and (f) hybrid Thompson vertical velocities averaged from t=4h to t=5h. Also, accumluated from t=4h to t=5h is the (a) control and (b) hybrid Thompson advection of water vapor (contoured), and (c) control and (d) hybrid Thompson diabatic heating/cooling (shaded). Contour levels used in (a) and (b) are -1.5, -1, -0.5, -0.2, 0.2, 0.5, 1, 1.5. Units of advection are 10^{-3} kg kg^{-1} h^{-1} . The model grid points are depicted along the absicaa.

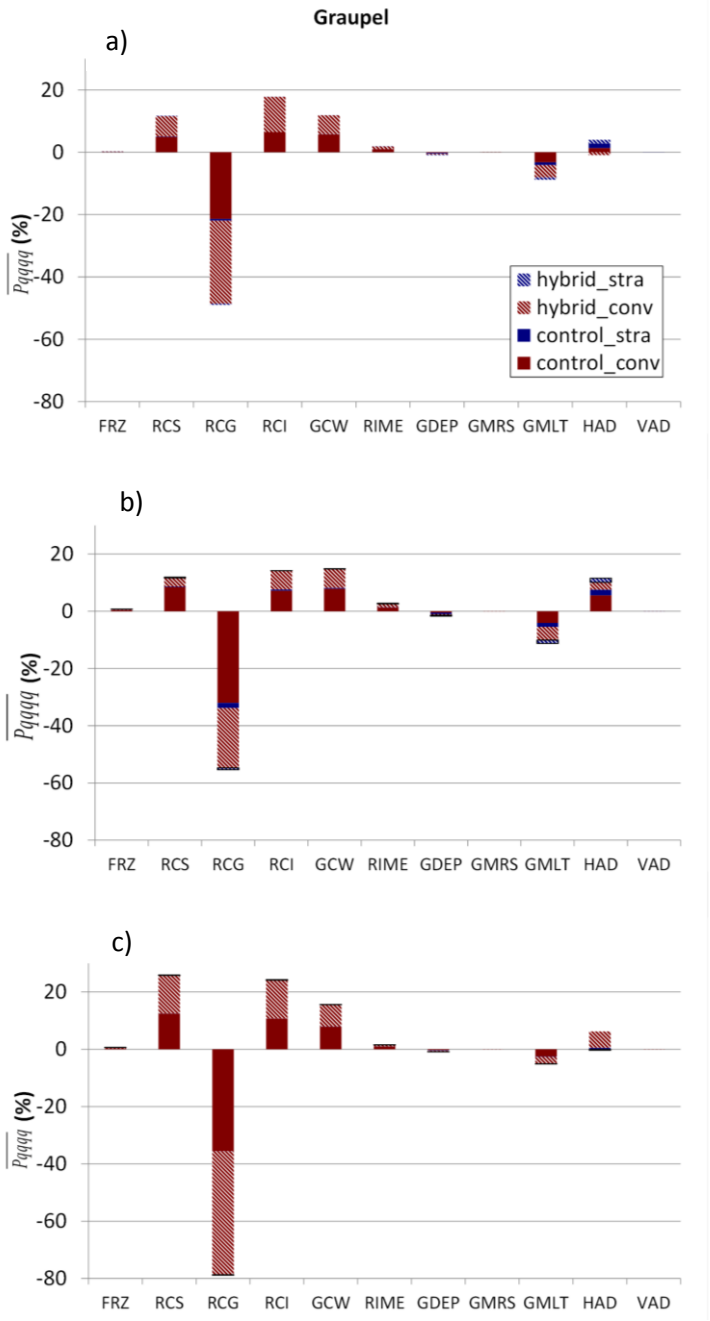

Fig. 14. Same as in Fig. 8, but for graupel. The processes are defined as follows:
FRZ: rain freezing, RCG: rain collecting graupel, GCW: graupel collecting cloud water, RCI: rain collecting ice, GCW: graupel collecting cloud water, RIME: rimed snow becoming graupel, GMRS: ice multiplication from rime-splinters, GMLT: graupel melting, HAD: horizontal advection of graupel and VAD: vertical advection of graupel.

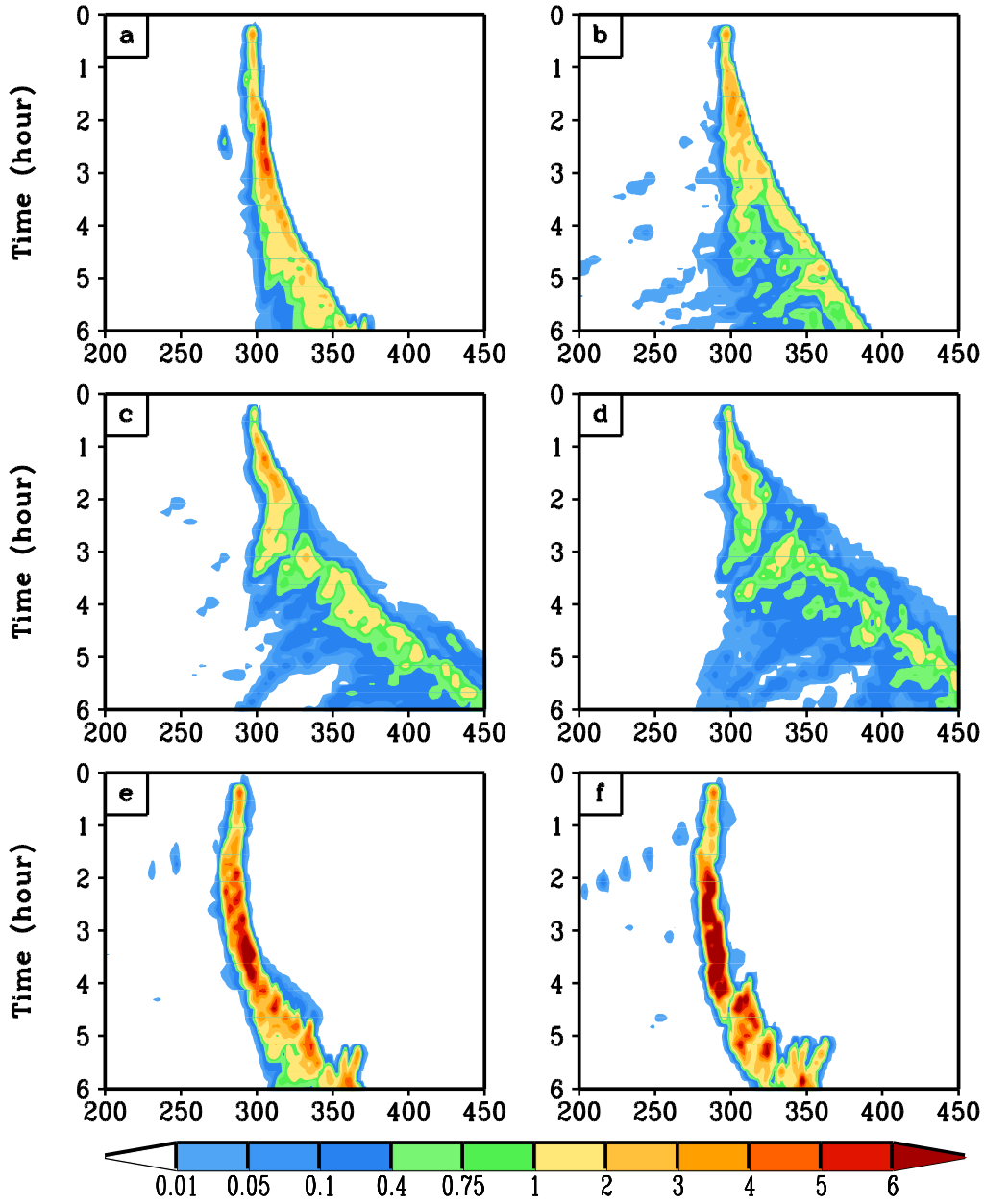

Fig. 15. Hovmöller diagrams of surface rainfall for the control (first column) and hybrid (second column) idealized Geresdi simulations using the (a),(b) Weisman, (c),(d) 12 June 2002 and (e),(f) LS soundings with the absicaa indicating the model grid points and rainfall in inches (1 inch = 25.4 mm).

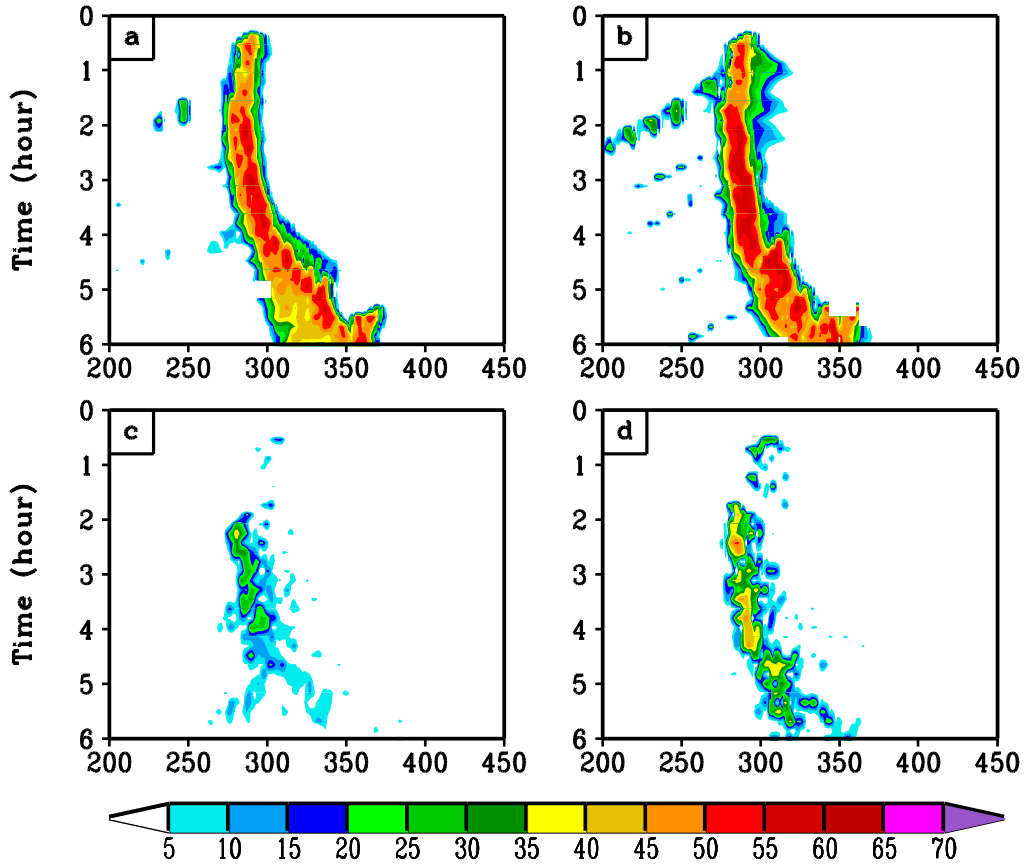

Fig. 16. Hövmuller diagrams of simulated radar reflectivity for the (a),(c) control and (b),(d) hybrid LS idealized Geresdi simulations with the absicaa indicating the model grid points. Units are dBZ.

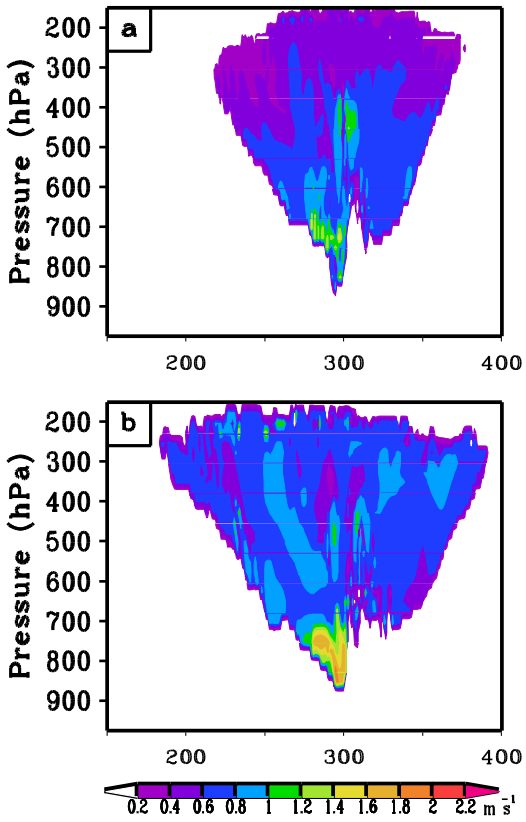

Fig. 17. Vertical cross sections of snow fall speeds at hour three of the (a) control and (b) hybrid Geresdi simulations for the Weisman case. The grid points are depicted along the absicaa and units of the fall speeds are in m s^{-1}.

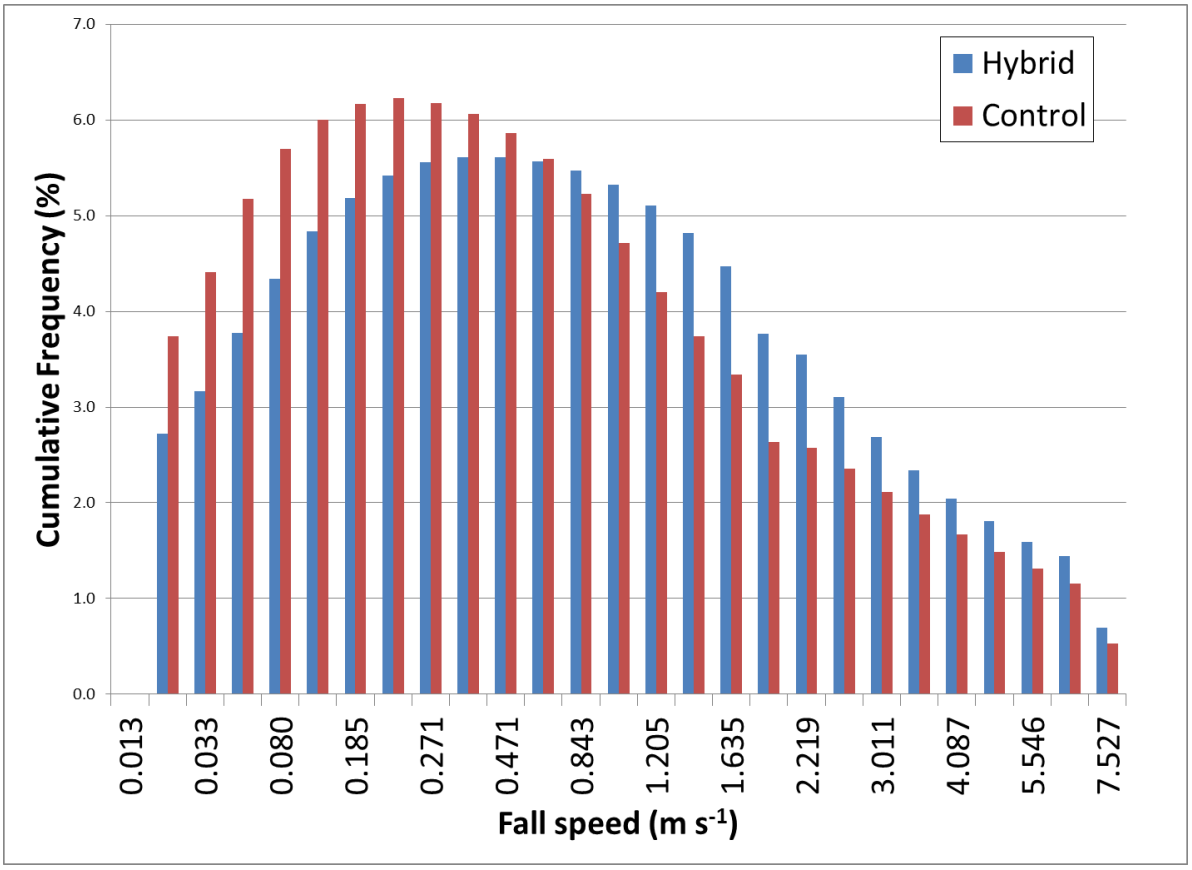

Fig. 18. Cumulative frequency diagram of snow fall speeds from the Geresdi control and hybrid simulations for the Weisman case.

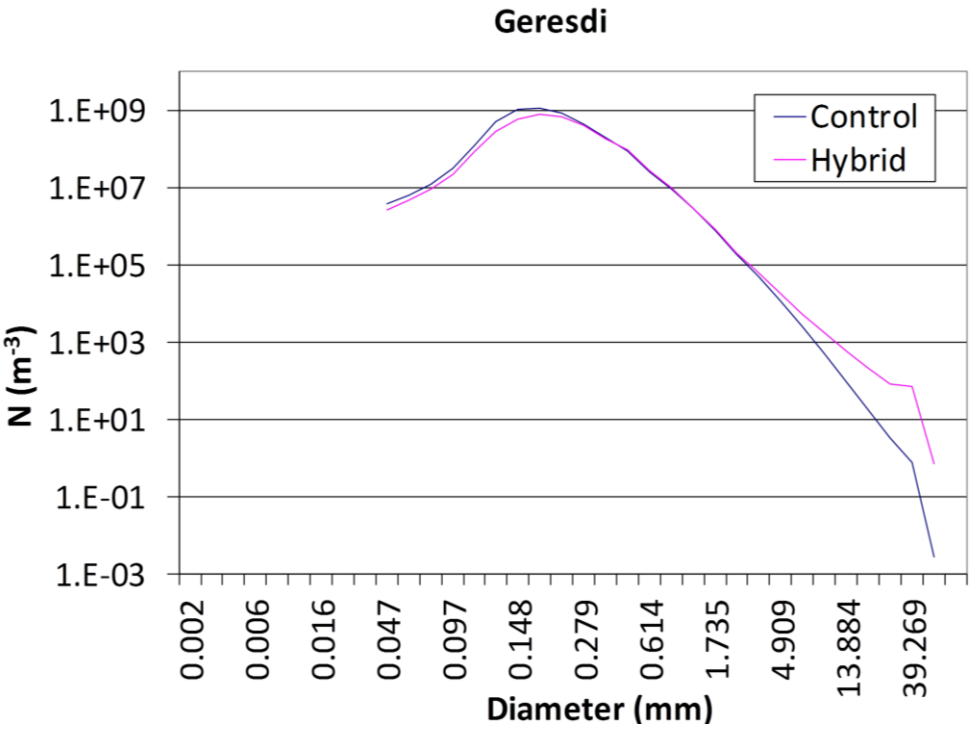

Fig. 19. Size distribution functions of snow for the Geresdi control and hybrid simulations for the Weisman case.

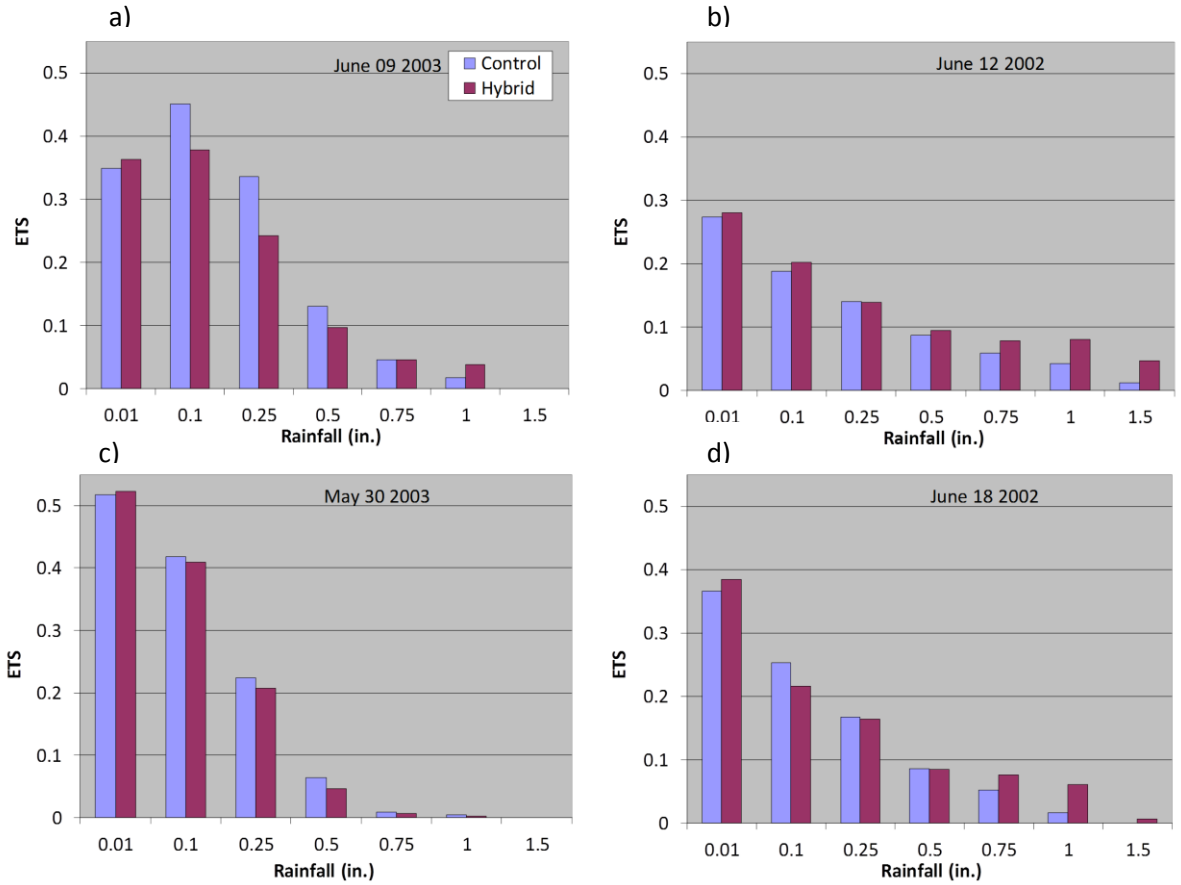

Fig. 20. ETS values for the (a) 09-10 June 2002, (b) 12-13 June 2002, (c) 30-31 May 2003 and (d) 19 June 2002 cases for the indicated rainfall thresholds and for the control and hybrid Thompson runs.

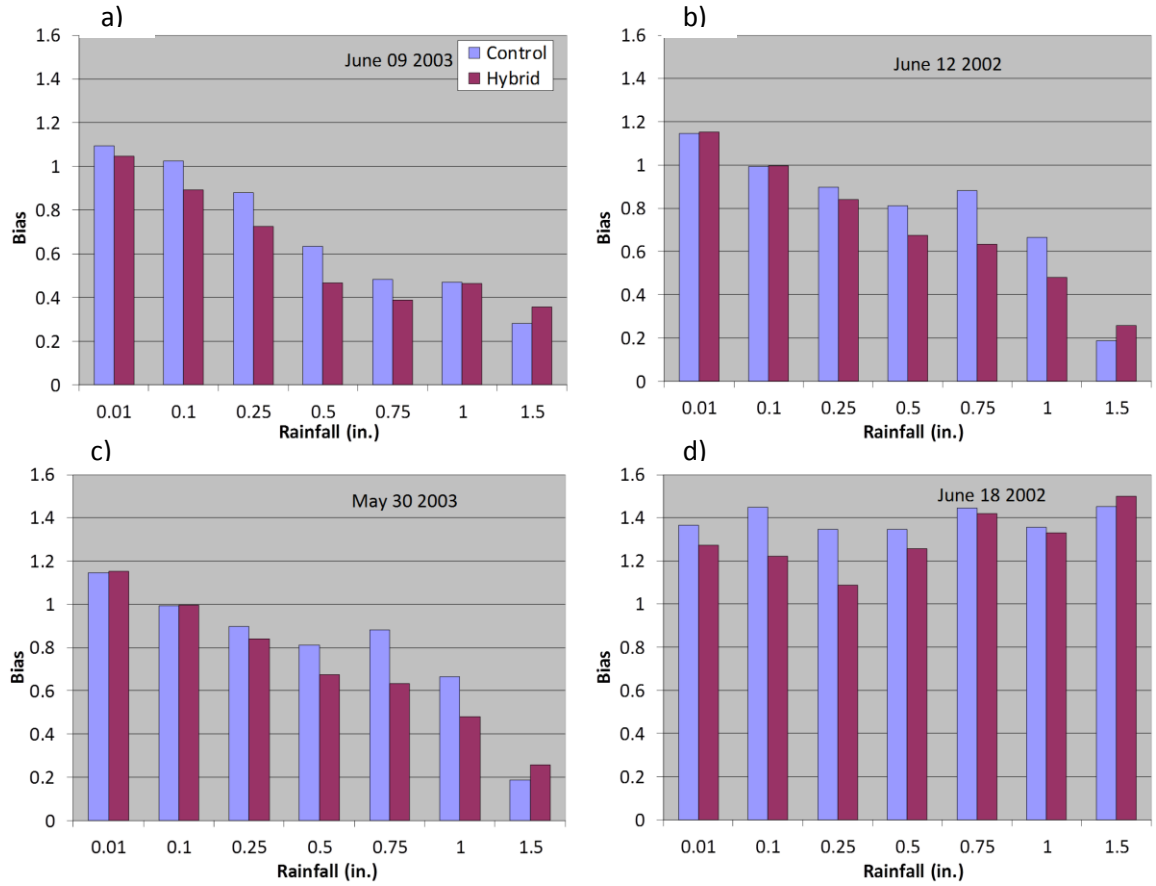

Fig. 21. Bias values for the (a) 09-10 June 2003, (b) 12-13 June 2002, (c) 30-31 May 2003 and (d) 19 June 2002 cases for the indicated rainfall thresholds and for the control and hybrid Thompson runs.

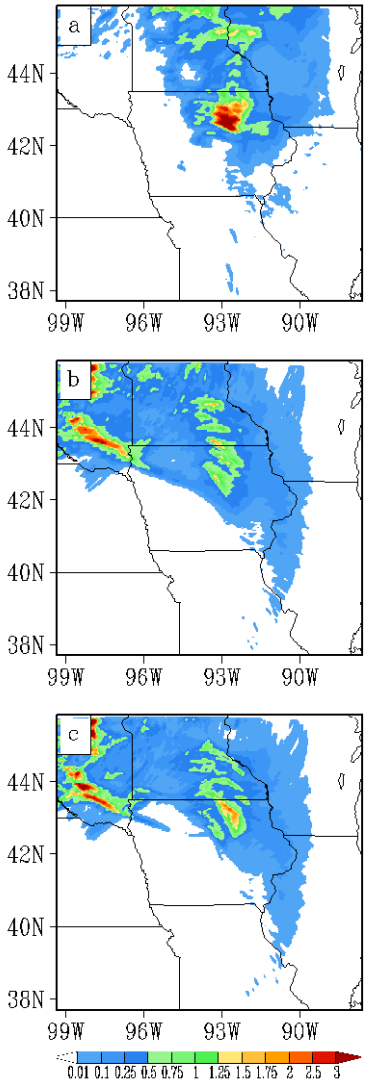

Fig. 22. The 15-h accumulated rainfall (inches) ending at 15 UTC 19 June 2002 from (a) observations, (b) the control run and (c) the hybrid Thompson run.

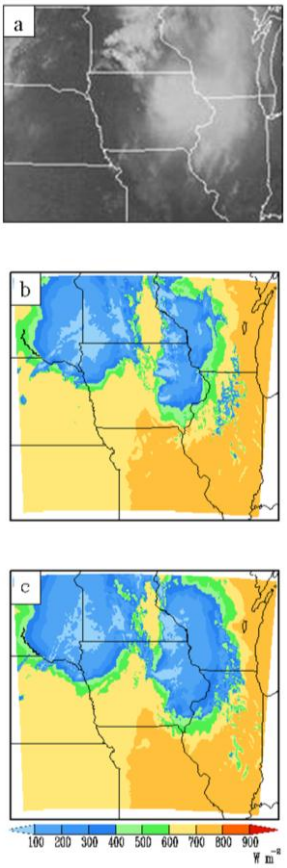

Fig. 23. The (a) visible satellite image valid at 15:15 UTC 19 June 2002 as well as the 15-h forecasted incoming surface shortwave radiation (W m^{-2}) valid at 15 UTC 19 June 2002 for the (b) control and (b) hybrid Thompson runs.

Table 1. Coeficients used in Eq.(1) for the indicated hydrometeors for the Geresdi and Thompson schemes as well as the prescribed reference density, ρ_o, used in the fall speed relations. Units of mass, m, are in kg.

Scheme Hydrometeor	α	β	f	ρ_o
Geresdi				1.20
Liquid	(Pruppacher and Klett 1997)			
Cloud ice	304	1	0	
Snow	$\alpha = \begin{cases} 1250, & m < 5.654 \cdot 10^{-9} \\ 4.84, & m \geq 5.654 \cdot 10^{-9} \end{cases}$ $\beta = \begin{cases} 1, & m < 5.654 \cdot 10^{-9} \\ 0.25, & m \geq 5.654 \cdot 10^{-9} \end{cases}$ $f = 0$			
Graupel	(Rasmussen and Hyemsfield 1987)			
Thompson				1.18
Rain	4854	1	195	
Cloud ice	1847.5	1	0	
Snow	40	0.55	125	
Graupel	442	0.89	0	

Table 2. Alphabetical listing and definitions of the Thompson source/sink terms indicated in the appendix. Units of these processes are in kg kg^{-1}.

Prg_gcw	graupel collecting cloud water
Prg_gde	graupel deposition/sublimation
Prg_ihm	ice multiplication from rime-splinters
Prg_rcg	rain collecting graupel
Prg_rci	rain collecting cloud ice
Prg_rcs	rain collecting snow
Prg_rfz	freezing of rain water into graupel
Prg_scw	rimed snow becoming graupel
Pri_rci	rain collecting ice
Pri_ide	deposition/sublimation of cloud ice
Pri_ihm	ice multiplication from rime-splinters
Pri_inu	condensation freezing
Pri_rfz	freezing rain water into cloud ice
Pri_wfz	freezing of cloud water into cloud ice
Prr_gml	graupel melting
Prr_rcg	rain collecting graupel
Prr_rci	rain collecting cloud ice
Prr_rcs	rain collecting snow
Prr_rcw	rain collecting cloud water
Prr_sml	snow melting
Prr_wau	autoconversion of cloud water to rain
Prs_iau	autoconversion of cloud ice to snow
Prs_ide	ice deposition/sublimation
Prs_ihm	ice multiplication from rime-splinters
Prs_rcs	rain collecting snow
Prs_sci	snow collecting cloud ice
Prs_scw	snow collecting cloud water
Prs_sde	snow deposition/sublimation
Prv_rev	rain evaporation
Prw_vcd	cloud water condensation/evaporation
Sed_g	sedimentation of graupel
Sed_i	sedimentation of ice
Sed_r	sedimentation of rain
Sed_s	sedimentation of snow

Table 3. Values of ETS and Bias averaged over 4 cases for the control and hybrid Thompson runs. The ETS and Bias values for the hybrid runs are bold (bold-italicized) to indicate an increase (decrease) in these values from the control runs. See text for the description of the runs.

Run	Rainfall threshold (in)						
	0.01	0.10	0.25	0.50	0.75	1.00	1.5
			ETS				
Control	0.376	0.328	0.217	0.092	0.041	0.020	0.003
Hybrid	**0.388**	***0.301***	***0.188***	***0.080***	**0.051**	**0.045**	**0.013**
			Bias				
Control	1.141	1.066	0.956	0.845	0.832	0.746	0.612
Hybrid	**1.088**	**0.944**	***0.806***	***0.728***	***0.731***	***0.699***	**0.733**

CHAPTER 5: GENERAL CONCLUSIONS

Bin microphysical schemes can better represent the sedimentation process than their bulk counterparts because of the bin scheme's ability to predict a variety of particles sizes for a given model grid box. Although bin schemes will not be used operationally in the near future, fall speed distributions from bin schemes could be used to replace bulk fall speed distributions in an attempt to improve the representation of fall speeds and resultant storm structure. This study first compared a bin scheme to commonly used bulk schemes and found microphysical processes often more important for the slowest falling particles in the bin scheme, with the reverse being true for the bulk microphysical schemes. The Lin bulk scheme was unique because it had increasing fall speeds of snow and graupel with increasing height, a feature that might be unrealistic and was caused by a small exponent used in the fall speed equation.

A probability matching technique was then used whereby bin fall speeds replaced bulk fall speeds in order to improve the storm structure of TS and LS systems. It was determined that the UPL vertical grid configuration, which doubled the number of levels above the freezing level compared to the 31 level control configuration, was the best to use for the fall speed experiment. Using the UPL vertical grid, rainfall forecasts improved, likely due to better resolved processes above the melting level, while rainfall forecasts worsened when the number of levels was doubled below the freezing level and when the levels were doubled throughout the domain. An improvement in rainfall forecasts was also noted when two levels were added to the surface layer, as turbulent momentum and heat fluxes were better resolved.

The use of the probability matching technique for the fall speed modifications in 2D hybrid Thompson simulations narrowed the stratiform rain region in both TS and LS cases,

contrary to expectations, due to reduced downward fluxes of snow especially near the melting level. The slower falling snow remained aloft for a longer period of time and contributed to a larger anvil. Sensitivity simulations whereby the Geresdi fall speeds were replaced with mass-weighted fall speeds resulted in a larger stratiform rain region from the increased downward fluxes of snow near the melting level. The larger fall speeds were caused by an evolving snow size distribution that allowed for larger particles to be predicted.

When the probability matching technique was applied to 3D hybrid Thompson simulations, an improvement in rainfall forecasts occurred for the lightest and heaviest rainfall. Similar to what was found in the 2D simulations, a narrower stratiform rain region and larger anvil were simulated in the 3D simulations, also a result of slower falling snow. Additionally, improved intensity forecasts of the heaviest rainfall were attributed to larger graupel fall speeds in the convective region, also noted in the 2D Weisman simulation.

Only modest improvements in rainfall forecasts were found using the probably matching technique. Although the sedimentation process is better represented in bin schemes, uncertainties in parameterizations within this scheme could indirectly impact its fall speed distributions negatively. An improvement in the treatment of melting ice in the bin scheme could prove to be beneficial. With a lack of observational data to verify fall speed distributions, bin schemes could provide the best opportunity to depict realistic grid volume fall speed distributions. One reason to peruse the probability matching technique or some other means of using bin fall speeds to improve bulk scheme simulations is because fall speed distributions were not case dependent suggesting that a universal technique could easily be developed. Such a technique would not only save on computational resources, but could also improve forecasts of warm-season rainfall.

REFERENCES

Aligo, E.A., W.A. Gallus, Jr., and M. Segal, 2007: Summer rainfall forecast spread in an ensemble initialized with different soil moisture analyses. *Wea. Forecasting,* **22,** 299-314.

_____, _____, _____, 2009: On the impact of WRF model vertical grid resolution on Midwest summer rainfall forecasts. *Wea. Forecasting.,* **24**, 576-594.

Baldwin, M. E., and K. E. Mitchell, 1997: The NCEP hourly multi-sensor U.S. precipitation analysis for operations and GCIP research. Prepints, *13th AMS Conference on Hydrology*, Long Beach, CA, 54-55.

Betts, A.K., 1986: A new convective adjustment scheme. Part I: Observational and theoretical basis. *Quart. J. Roy. Meteor. Soc.*, **112,** 677-692.

____, and M.J. Miller, 1986: A new convective adjustment scheme. Part II: Single column tests using GATE wave, BOMEX, ATEX and arctic air-mass data sets. *Quart. J. Roy. Meteor. Soc.*, **112,** 693-709.

Braun, S. A., and R. A. Houze Jr., 1994: The transition zone and secondary maximum of radar reflectivity behind a midlatitude squall line: Results retrieved from Doppler radar data. *J. Atmos. Sci.*, **51,** 2733-2755.

Bryan, G. H., J. C. Wyngaard and J. M. Fritsch, 2003: Resolution requirements for the simulation of deep moist convection. *Mon. Wea. Rev.,* **131,** 2394-2416.

Churchill, D. D. and R. A. Houze, Jr., 1984: Development and structure of winter monsoon

cloud clusters on 10 December 1978. *J. Atmos. Sci.*, **41**, 933-960.

Colle, B. A., and C. F. Mass, 2000: The 5-9 February 1996 flooding event over the Pacific Northwest: Sensitivity studies and evaluation of the MM5 precipitation forecasts. *Mon. Wea. Rev.*, **128,** 593-617.

_____, M. F. Garvert, J. B. Wolfe, C. F. Mass and C. P. Woods, 2005: The 13-14 December 2001 IMPROVE-2 event. Part III: Simulated microphysical budgets and sensitivity studies. *J. Atmos. Sci.*, **62,** 3535-3558.

_____, and S. E. Yuter, 2007: The impact of coastal boundaries and small hills on the precipitation distribution across southern Connecticut and Long Island, New York. *Mon. Wea. Rev.*, **135**, 933-954.

Cotton, W. R., G. J. Tripoli, R. M. Rauber, and E. A. Mulvihill, 1986: Numerical simulation of the effects of varying ice crystal nucleation rates and aggregation processes on orographic snowfall. *J. Climate Appl. Meteor*., **25**, 1658-1680.

Davis, C., and Coauthors, 2004: The bow echo and MCV experiment: observations and opportunities. *Bull. Amer. Meteor. Soc*., **85,** 1075-1093.

Doswell III, C. A., H. E. Brooks, and R. A. Maddox, 1996: Flash flood forecasting: An ingredients-based methodology. *Wea. Forecasting.,* **11**, 560-581.

Ebert, E. E., 2001: Ability of a poor man's ensemble to predict the probability and distribution of precipitation. *Mon. Wea. Rev.,* **129,** 2461-2480.

Ek, M. B., K.E. Mitchell, Y. Lin, E. Rogers, P. Grunmann, V. Koren, G. Gayno, and J.D. Tarplay, 2003: Implementation of Noah land surface model advances in the National Centers for Environmental Prediction operational mesoscale Eta model. *J. Geophys. Res.*, **108,** 8851, doi:10.1029/2002JD003296.

Ferrier, B. S., 1994: A double-moment multiple-phase four-class bulk ice scheme. Part I: Description. *J. Atmos. Sci.,* **51,** 249-280.

Fritsch, J. M., R. J. Kane, and C. R. Chelius, 1986: The contribution of mesoscale convective weather systems to the warm-season precipitation in the United States. *J. Climate Appl. Meteor.*, **25**, 1333-1345.

_____, and R. E. Carbone, 2004: Improving quantitative precipitation forecasts in the warm season: A USWRP research and development strategy. *Bull. Amer. Meteor. Soc.*, **85,** 955-965.

Gallus, W. A. Jr. and R. H. Johnson, 1995: The dynamics of circulations within the trailing stratiform regions of squall lines. Part I: The 10-11 June PRE-STORM system. *J. Atmos. Sci.*, **52,** 2161-2187.

_____, and M. Segal, 2001: Impact of improved initialization of mesoscale features on convective system rainfall in 10-km Eta simulations. *Wea. Forecasting.*, **16,** 680-696.

_____, J. Correia Jr. and I. Jankov, 2005: The 4 June 1999 derecho event: A particularly difficult challenge for numerical weather prediction. *Wea. Forecasting.,* **20**, 705-728.

_____, and M. Pfeifer, 2008: Intercomparision of simulations using 5 WRF microphysical schemes with dual-Polarization data for a German squall line. *Advances in Geosciences.,* **16**, 109-116.

_____, N. A. Snok, E. V. Johnson, 2008: Spring and summer severe weather reports over the Midwest as a funciton of convective mode: A preliminary study, *Wea. Forecasting.*, **23**, 101-113.

Geresdi, I, 1998: Idealized simulation of the Colorado hailstorm case: comparison of bulk and detailed microphysics. *Atmospheric Research,* **45**, 237-252.

Gilmore, M. S., J. M. Straka and E. N. Rasmussen, 2004A: Precipitation and evolution sensitivity in simulated deep convective storms: Comparisons between liquid-only and simple ice and liquid phase microphysics, *Mon. Wea. Rev*., **132,** 1897-1916.

_____, _____ and _____, 2004b: Precipitation uncertainty due to variations in precipitation particle parameters within a simple microphysics scheme. *Mon. Wea. Rev.,* **132,** 2610-2627.

Grams, J. S., W. A. Gallus, Jr. S. E. Koch, L. S. Wharton, A. Loughe and E. E. Ebert, 2006: The use of a modified Ebert-McBride Technique to evaluate mesoscale model QPF as a function of convective system morphology during IHOP 2002. *Wea. Forecasting*, **21,** 288-306.

Hong, S. –H., J. Dudhia and S. –H. Chen, 2004: A revised approach to ice microphysical processes for the bulk parameterization of clouds and precipitation. *Mon. Wea.Rev.*, **132,** 103-120.

_____ and J. –O. Lim, 2006: The WRF single-moment 6-class microphysics scheme (WSM6). *Journal of the Korean Meteorological Society*, **42,** 129-151

Houze, R. A., Jr., 1982: Cloud clusters and large-scale vertical motions in the tropics, 1982. *J. Meteorol. Soc. Japan*, **60**, 396-409.

Janjic, Z.I., 1994: The step-mountain Eta coordinate model: Further developments of the convection closure schemes. *Mon. Wea. Rev*., **122,** 927-945.

_____, 2002: Nonsingular implantation of the Mellor-Yamada level 2.5 scheme in the NCEP meso model. NOAA/NWS/NCEP Office Note #437, 61 pp.

Jankov, I. and W. A. Gallus Jr., 2004: MCS rainfall forecast accuracy as a function of large-scale forcing. *Wea. Forecasting.*, **19**, 428-439.

_____, W.A. Gallus Jr., M. Segal, B. Shaw and S. E. Koch, 2005: The impact of different WRF model physical parameterizations and their interactions on warm season MCS rainfall. *Wea. Forecasting.,* **20**, 1048-1060.

_____, _____, _____ and S. E. Koch, 2007: Influence of initial conditions on the WRF-ARW model QPF response to physical parameterization changes. *Wea. Forecasting.*, **22,** 501-519.

Jewett, B. F. and R. B. Wilhelmson, 2006: The role of forcing in cell morphology and evolution within midlatitude squall lines. *Mon Wea. Rev*., **134,** 3714-3734.

Kain, J. S., and J. M. Fritsch, 1990: A one-dimensional entraining/detraining plume model and its application in convective parameterization. *J. Atmos. Sci.*, **47,** 2784-280.

_____ and _____, 1993: The role of convective "trigger function" in numerical forecasts of mesoscale convective systems. *Meteor. Atmos. Phys.,* **49,** 93-106.

_____ and _____, 1998: Multiscale convective overturning in mesoscale convective systems: Reconciling observations, simulations, and theory. *Mon Wea. Rev*., **126,** 2254-2273.

Kallos, G. and M. Segal, 1991: On the meteorological conditions during postprecipitation periods: Implications to pollutant dispersion. *J. Appl. Meteor.,* **30,** 297-311.

Kimball, S. K. and F. C. Dougherty, 2006: The sensitivity of idealized hurricane structure and development to the distribution of vertical levels in MM5. *Mon*

Wea. Rev., **134,** 1987-2008.

Knupp, K.R. and W. R. Cotton, 1987: Internal structure of a small mesoscale convective system. *Mon. Wea. Rev.,* **115**, 629-645.

Lin, Y. –L., R. D. Farley and H. D. Orville, 1983: Bulk parameterization of the snow field in a cloud model. *J. Appl. Meteor.,* **22,** 1065-1092.

_____, B. A. Colle, C. Woods and B. F. Smull, 2006: Verification of WRF for the 4-5 December 2001 IMPROVE-2 event over the central Oregon Cascades. Preprints, *7th WRF Users' Workshop,* Boulder, CO, National Center for Atmospheric Research, P2-2.

_____and _____, 2008: The 4-5 December 2001 IMPROVE-2 Event: Observed Microphysics and Comparisons with the Weather Research and Forecasting Model. *Mon.Wea.Rev.,* **137,** 1372-1392.

Lindzen, R. S. and M. Fox-Rabinovitz, 1989: Consistent Vertical and Horizontal Resolution. *Mon. Wea. Rev*., **117,** 2575-2583.

Locatelli, J. D. and P. V. Hobbs, 1974: Fall speeds and masses of solid precipitation particles. *J. Geophys. Res.,* **79,** 2185-2197.

Lynn, B. H., A. P. Khain, J. Dudhia, D. Rosenfeld, A. Pokrovsky and A. Seifert, 2005: Spectral (Bin) microphysics coupled with a mesoscale model (MM5). Part II: Simulation of a CaPE rain event with a squall line. *Mon.Wea.Rev.*, **133,** 59-71.

_____ and _____, 2007: Utilization of spectral bin microphysics and bulk parameterization schemes to simulate the cloud structure and precipitation in a mesoscale rain event. *J. Geophys. Res.*, **112,** 22205, doi:10.1029/2007JD008475.

Markowski, P. M., E. N. Rasmussen, J. M. Straka and D. C. Dowell, 1998: Observations of low-level baroclinicity generated by anvil shadows. *Mon Wea. Rev*., **126,** 2942-2958.

Marshall, J.S. and W. Mc K. Palmer, 1948: The distribution of raindrops with size. *Journal of Meteorology*., **5,** 165-166.

Mass, C.F., D. Ovens, K. Westrick, and B.A. Colle, 2002: Does increasing horizontal resolution produce better forecasts? The results of two years of real-time numerical weather prediction over the Pacific Northwest. *Bull.Amer.Meteor*. Soc., **82,** 407-430.

Matrosov, S. Y., A. V. Korolev and A. J. Heymsfield, 2002: Profiling cloud ice mass and particle characteristic size from Doppler radar measurements. *J. Atmos. Oceanic Technol.*, **19,** 1003-1018.

McCumber, M., W-K. Tao, J. Simpson, R. Penc ands-T Soong, 1991: Comparison of ice-phase microphysical parameterization schemes using numerical simulations of tropical convection. *J. Appl. Meteor.,* **30,** 985-1004.

Milbrandt, J.A., and M. K. Yau, 2005a: A multimoment bulk microphysics parameterization. Part I: Analysis of the role of the spectral shape parameter. *J. Atmos. Sci.,* **62,** 3051-3064.

Molinari, J. and M. Dudek, 1992: Parameterization of convective precipitation in mesoscale numerical models: A critical review. *Mon Wea. Rev.*, **120,** 326-344.

Morrison, H, and A. Gettelman, 2008: A new two-moment bulk stratiform cloud microphysics scheme in the Community Atmosphere Model Version 3 (CAM3). Part I: Description and numerical tests. . *J. Climate.,* **21,** 3660-3679.

_____, G. Thompson, and V. Tatarskii, 2009: Impact of cloud microphysics on the development of trailing stratiform precipitation in a simulated squall line: Comparison of one- and two-moment schemes. *Mon.Wea.Rev.,***128,** 991-1007.

Ookouchi, Y., M. Segal, R. C. Kessler and R. A. Pielke, 1984: Evaluation of soil moisture effects on the generation and modification of mesoscale circulations. *Mon Wea. Rev.*, **112,** 2281-2292.

Orr, B. W. and R. A. Kropfli, 1998: A method for estimating particle fall velocities from vertically pointing Doppler radar. *J. Atmos. Oceanic Technol.,* **16,** 29-37.

Panofsky, H. A. and J. A. Dutton, 1984: *Atmospheric Turbulence.* John Wiley & Sons, Inc., 397.

Parker, M.D. and R. H. Johnson, 2000: Organizational modes of midlatitude mesoscale convective systems, *Mon.Wea.Rev.*,**128,** 3413-3436.

_____, and _____, 2004A: Structures and dynamics of quasi-2D mesoscale convective systems, *J. Atmos. Sci.*, **61,** 545-567.

_____, _____, 2004c: Simulated convective lines with leading precipitation. Part II: Evolution and Maintenance, *J. Atmos. Sci.*, **61,** 1656-1673.

Parsons, D., cited 2002: IHOP_2002 Water Vapor Intercomparisoins Workshop Presentations. [Available online at [http://www.atd.ucar.edu/dir_off/projects/2002/IHOPwsOct03 /presentations.html].

Pecnick, M. J., and D. Keyser, 1989: The effect of spatial resolution on the simulation of upper-tropospheric frontogenesis using a sigma-coordinate primitive equation model. *Meteor. Atmos. Phys.*, **40,** 137-149.

Potter, B. E., 1991: Improvements to a commonly used cloud microphysical bulk parameterization. *J. Appl. Meteor.*, **30,** 1040-1042.

Pruppacher, H. R., and J. D. Klett, 1978: *Microphysics of Clouds and Precipitation.* D. Reidel, 714 pp..

Rasmussen, R. M. and A. J. Heymsfield, 1987: Melting and shedding of graupel and hail. Part I: Model physics. *J. Atmos. Sci.*, **44,** 2754-2763.

_____, I. Geresdi, G. Thompson, K, Manning and E. Karplus, 2002: Freezing drizzle formation in stably stratified layer clouds: The role of radiative cooling of cloud droplets, cloud condensation nuclei, and ice initiation. *J. Atmos. Sci.,* **59,** 837-860.

Raymond, W. H., and R. M. Aune, 1998: Improved precipitation forecasts using parameterized precipitation drag in a hydrostatic forecast model. *Mon.Wea.Rev.,***135,** 693-710.

Roebber, P. J. and J. Eise, 2001: The 21 June 1997 flood: Storm-scale simulations and implications for operational forecasting. *Wea. Forecasting,* **16,** 197-218.

_____, P.J., D.M. Schultz, B.A. Colle, and D.J. Stensrud, 2004: The risks and rewards of high-resolution and ensemble numerical weather prediction. *Wea. Forecasting*, **19,** 936-949.

Rogers, E., T. Black, B. Ferrier, Y. Lin, D. Parrish and G. DiMego, 2001: Changes to the NCEP Meso Eta analysis and forecast system: Increase in resolution, new cloud microphysics, modified precipitation assimilation, modified 3DVAR analysis. NWS Technical Procedures Bulletin 488, NOAA/NWS [Available online at http://www.emc.ncep.noaa.gov/mmb/mmbpll/eta12tpb/].

Rosenberg, N. J., B. L. Blad and S. B. Verma, 1983: *Microclimate,* John Wiley & Sons, Inc., 495.

Rutledge, S. A., and R. A. Houze Jr., 1987: A diagnostic modeling study of the trailing stratiform region of a midlatitude squall line. *J. Atmos. Sci.,* **44,** 2640-2656.

Schaefer, J.T., 1990: The critical success index as an indicator of warning skill. *Wea. Forecasting*, **5,** 570-575.

Segal, M., J. F. W. Purdom, J. L. Song, R. A. Pielke and Y. Mahrer, 1986: Evaluation of cloud shading effects on the generation and modification of mesoscale circulations. *Mon Wea. Rev*., **114,** 1201-1212.

Shaw, B. L., 2004: An objective inter-comparison of WRF,MM5, and NCEP ETA shortrange quantitative precipitation forecasts for the International H_2O Project (IHOP) domain. *Extended Abstract, 5th WRF/14th MM5 Users' Workshop*, Boulder, CO, National Center for Atmospheric Research, 3.6. [Available online at http://www.mmm.ucar.edu/mm5/workshop/workshop-papers_ws04.html].

Skamarock, W.C., J.B. Klemp, J. Dudhia, D.O. Gill, D.M. Barker, W. Wang, and J.G. Powers, 2005: A description of the advanced research WRF version 2. NCAR Tech. Note NCAR/TN-468+STR, 88 pp. [Available online at http://www.wrf-model.org/wrfadmin/docs/arw_v2.pdf]

Stein U. and P. Alpert, 1993: Factor separation in numerical simulations. *J. Atmos. Sci.*, **50,** 2107- Steiner, M., R. A. Houze Jr., and S. E. Yuter, 1995: Climatological characterization of three-dimensional storm structure from operational radar and rain gauge data. *J. Appl. Meteor.,* **34,** 1978-2007.

Steiner, M., R. A. Houze Jr., and S. E. Yuter, 1995: Climatological characterization of three-dimensional storm structure from operational radar and rain gauge data. *J. Appl. Meteor.,* **34,** 1978-2007.

Storm, B.A., M. D. Parker, and D. P. Jorgensen, 2007: A convective line with leading stratiform precipitation from BAMEX. *Mon.Wea.Rev.,***135,** 1769-1785.

Thompson, G., P. R. Field, W. D. Hall and R. M. Rasmussen, 2006: A new bulk microphysical parameterization for WRF (&MM5). Preprints, *7th WRF Users' Workshop,* Boulder, CO, National Center for Atmospheric Research, 1-11.

_____, _____, R. M. Rasmussen, and W. D. Hall 2008: Explicit forecasts of winter precipitation using an improved bulk microphysics scheme. Part II: Implementation of a new snow parameterization. *Mon.Wea.Rev.,* **136,** 5095-5115.

Tribbia, J. J. and D. P. Baumhefner, 1988: The reliability of improvements in deterministic short-range forecasts in the presence of initial state and modeling deficiencies. *Mon. Wea. Rev*., **116,** 2276-2288.

Verlinde, J., P. J. Flatau, and W. R. Cotton, 1990: Analytical solutions to the collection growth equation: Comparison with approximate methods and application to the cloud microphysics parameterization schemes. *J. Atmos. Sci.*, **47**:2871–2880.

Walko, R. L., W. R. Cotton, M. P. Meyers, and J. Y. Harrington, 1995: New RAMS cloud microphysics parameterization. Part I: The single-moment scheme. *Atmos. Res.*, **38**, 29–62.

Warner, T. T. and H-M Hsu, 2000: Nested-model simulation of moist convection: The impact of coarse-grid parameterized convection on fine-grid resolved convection. *Mon. Wea. Rev*., **128,** 2211-2231.

Wei, H., M. Segal, W. J. Gutowksi Jr., Z. Pan, R. W. Arritt and W. A. Gallus Jr., 2001: Sensitivity of simulated regional surface thermal fluxes during warm advection snowmelt to selection of the lowest model level height. *J. Hydrometeor*., **2,** 395-405.

Weisman, M. L., J. B. Klemp, and R. Ruttunno, 1988: Structure and evolution of numerically simulated squall lines. *J. Atmos. Sci.*, **45**, 1990-2013.

_____, W. C. Skamarock, and J. B. Klemp, 1997: The resolution dependence of explicitly modeled convective systems. *Mon.Wea.Rev.*, **136,** 527-548.

_____, C. Davis and J. Done, 2004: The promise and challenge of explicit convective forecasting with the WRF model. Preprints, *22nd Conference on Severe Local Storms*, Hyannis, MA, American Meteorological Society, 17-2.

Zhang, D.-L., and X. Wang, 2003: Dependence of hurricane intensity and structure on vertical resolution and time-step size. *Advances in Atmospheric Sciences*, **20,** 711-725.